BEYOND-GR WAVEFORM MODELS AND NUMERICAL RELATIVITY

A Dissertation

Presented to the Faculty of the Graduate School

of Cornell University

in Partial Fulfillment of the Requirements for the Degree of

Doctor of Philosophy

by

Gabriel Steffano Bonilla

August 2021

BEYOND-GR WAVEFORM MODELS AND NUMERICAL RELATIVITY

Gabriel Steffano Bonilla, Ph.D.

Cornell University 2021

Our current model for the description of spacetime, Einstein's general relativity, is now over a century old. Experimental and computational capabilities have advanced greatly since then, and now we are able to both compute as well as observe gravitational waves in the strong-field regime: gravitational waves that result from events as energetic as the merger of two black holes.

The computer calculations that are used to study general relativity have increased in sophistication over the last several years, and will be continued to be improved upon, as the field of gravitational wave experiment matures. In the first two chapters of this thesis we discuss the development and testing of a new relativity code intended to improve upon the accuracy of previous numerical calculations, a numerical relativity code that could perhaps be used in the calculation of spacetimes in theories of gravity beyond general relativity.

In the third chapter of this thesis we discuss the currently existing gravitational wave models and the efforts that have been invested toward preparing these models to be compatible with future numerical and analytical results of beyond-GR calculations. We talk about the various effects that might be observable depending on the beyond-GR theory, and how each of these effects might be incorporated in a generic gravitational wave template.

BIOGRAPHICAL SKETCH

Gabriel Steffano Bonilla was born and raised in California, where he did his undergraduate degree in physics and in mathematics at the University of California, Davis. He worked with Prof. Manuel Calderón de la Barca Sánchez on experimental particle physics and Prof. Andrew Waldron on gauge theory. In 2015, he left California to join Prof. Saul Teukolsky at Cornell University in Ithaca to work on numerical relativity.

To Maya and Marcie.

I love you.

ACKNOWLEDGEMENTS

For my time here that I've had at Cornell, I must first thank my mentor and advisor, Prof. Saul Teukolsky. I appreciate how much his presence, guidance, and encouragement has allowed me to find my own, and navigate the academic world. So much more became possible because of his mentorship. I still remember progressing through the early stages of my domain research and Saul telling me, "Keep doing what you're doing." I have held onto, and will always hold onto, the confidence those words have given me.

I also thank Dr. Larry Kidder for his presence, patience, and spirit. It was through Larry that I learned that we were more a collaboration than a company with a rigid hierarchy, that I could be vulnerable and feel safe to make mistakes, and that I could also take leadership when I had contributions to make to the group that I felt I was suited to make. And of course, our board game group every Wednesday. They helped me feel more at home.

I also thank my committee members Prof. Éanna Flanagan and Prof. Julia Thom for their guidance and questions, their balance has informed much of how I communicate science to others, and will continue to do so.

I must also thank Dr. Prayush Kumar, who provided significant guidance to me in my final years of graduate school. Prayush takes great care in his pedagogical explanations of material I needed to understand for my research. I hope to be able to pay forward the patience and education he has provided me with.

I also thank Dr. Geoffrey Lovelace, whose calming presence and encouragement has steadied me and honed my determination. I am looking forward to our collaboration.

I thank the SXS collaboration for making my graduate school experience an exciting and engaging, and most importantly, safe experience. I look forward to continue being

a part of it.

The graduate students I will miss the most. In the office, the time I spent with Will Throwe, Nils Deppe, Éamonn O'Shea, Dante Iozzo, Cristóbal Armaza, Daniel Vieira, and Ethan Chen made for some of the most memorable years of my life. It was a pleasure being able to work alongside them, and it was a pleasure to get to know them personally. I am so grateful that they felt the same way about me. I wish them all the best.

In the department, I must also thank Paul Corlies, Catie Ball, and so many of the graduate students of SSB. The memories of our lunches and board game nights and late nights out together are already idyllic. Thank you so much for everything.

In Physics, I thank Thomas Oseroff, Nilanjan Banerjee, and Patrick Hollister. We have been together since the beginning and we're almost done! Just a few more late night sessions to go. I look forward so seeing us all on the other side of the journey we started in Fall 2015.

On the east coast, I thank Stacey Ramirez and Brittany Ramirez. You gave me a home away from home and for that I will always be thankful.

On the west coast, I thank Christina Yu and Christine Nguyen. It has been six long years but you've been with me through it all. Thank you; to many more.

Finally, I thank my parents Rosa Maria Bonilla and Gabriel Eliseo Bonilla and the rest of my family. All the support they have given to me has led me to this moment.

I am so thankful to everyone who made this dream possible. I will remember it always.

CONTENTS

[1]This chapter will appear as a technical note in the public repository for the SpECTRE code[1]. Portions of it will appear in an upcoming paper describing the code.

LIST OF TABLES

LIST OF FIGURES

CHAPTER 1

INTRODUCTION

General relativity is a description of spacetime that has enjoyed much experimental success over the last hundred years. Most recently, its predictions have been confirmed by gravitional wave observatories such as LIGO. These observatories use calculations in general relativity to make detections and to measure source parameters. General relativity, in the strong-field regime probed by LIGO, is highly nonlinear, and requires sophisticated computational methods to resolve the dynamical spacetime where analytic methods begin to fail. The field of computational physics that solves Einstein's equations numerically is called numerical relativity.

When gravitational wave data is compared with the predictions of general relativity, a natural question is whether any deviations from the theory might become measurable. How can we search for such deviations and be sure they are real and not artifacts of the noise in the measurement process? And if deviations are found, we can imagine one day making numerical simulations with an alternative theory of gravity to make detections by LIGO or future gravitational wave observatories.

This thesis concerns itself with the development of two necessary components of this broader project: (i) the development of a numerical relativity code powerful enough to take advantage of upcoming exascale machines; and (ii) the development of a waveform model that will enable searches for deviations from general relativity now

and will also be able to make use of future beyond-GR numerical relativity codes.

1.1 Numerical Relativity

General relativity is a theory of gravity which was first published by Albert Einstein in 1915. The Einstein field equations relate the geometry of spacetime to the behavior of the matter within the spacetime:

$$G_{\mu\nu} = 8\pi T_{\mu\nu}, \tag{1.1}$$

where $G_{\mu\nu}$ is the Einstein tensor, constructed from the metric tensor $g_{\mu\nu}$ and its first and second derivatives, and $T_{\mu\nu}$ is the stress-energy tensor. While this covariant form of the equation may be useful in analytical calculations, it does not lend itself to numerical simulation. In a simulation, we need to set up some initial condition on the the computer. Then we use Einstein's equations to tell us how to advance the initial field values for a small time increment, Δt. We then keep repeating this process. Such a procedure requires us to choose a set of time slices $t = \text{const}$ in the spacetime. This *spacetime slicing*, or foliation, decomposes the four-dimensional spacetime into a set of three-dimensional spacelike slices, indexed by a one-dimensional time coordinate.

The Einstein field equations, when decomposed in this 3+1 fashion, yield Maxwell-like equations that determine the metric quantities on the spacelike hypersurfaces, as well as their evolution through time. Four of the equations are elliptic constraint equations, which restrict the solution on the initial hypersurface. They are analogous to the the $\nabla \cdot \mathbf{B}$ and $\nabla \cdot \mathbf{E}$ Maxwell equations. The remaining six equations are hyperbolic evolution equations, analogous to the the $\partial\mathbf{E}/\partial t$ and $\partial\mathbf{B}/\partial t$ equations. In this thesis we will concern ourselves with the evolution equations.

The six hyperbolic equations involve second-order derivatives of the metric, but can be cast into first-order form via the introduction of auxiliary variables that are the first derivatives of the metric. The equations then take the general conservation form

$$\partial_t u + \partial_i F^i = S, \tag{1.2}$$

where u are the conserved variables, F^i are the fluxes of these variables, and S are the source terms. Since F^i and S are complicated nonlinear functions of the variables, the equations are challenging to solve.

A major advance in numerical relativity for black hole simulations was the realization that spectral-type methods are extremely efficient in the case of smooth solutions when compared to finite-difference methods. While finite-difference methods approximate the spatial derivatives that appear in the evolution equations, in a spectral method, it is the solution that is approximated by an expansion in a set of $N + 1$ basis functions:

$$u(x) \approx \sum_{i=0}^{N} u_i \phi_i(x), \tag{1.3}$$

where $\phi_i(x)$ are the basis functions, and u_i are their corresponding coefficients in the expansion.

Thousands of binary black hole waveforms have been computed and catalogued[1] since Frans Pretorius performed the first successful simulation of a black hole binary inspiral and merger in 2005[2]. Such calculations made possible the first detection of black hole mergers by LIGO[7]. However, when the next generation of ground-based gravitational wave detectors such as the Einstein telescope come online, calculations of binary black hole waveforms will need to be about ten times more accurate[3]. Such a

task requires the development of a faster, as well as more accurate, numerical relativity code.

1.2 SpECTRE

The goal of the SpECTRE project is to develop a simulation code that can take advantage of the upcoming generation of supercomputers[4]. Current numerical relativity codes do not run efficiently on more than about a hundred or a few thousand processors, depending on the algorithms used. Exascale machines will make 10^5 – 10^6 processors available to a typical user. SpECTRE will take advantage of this large processor count by using novel techniques to discretize the equations and to distribute the computations across all the processors.

In Chapter 2 of the thesis, I describe my contributions to SpECTRE. I have been responsible for the design of suitable computational domains for the simulation of astrophysical phenomena, including the mergers of black holes and neutron stars. In SpECTRE, the computational domain is divided into adjacent hexahedral subdomains that can be distributed across the processors to enable parallel processing. The partitioning of the domain into hexahedral elements creates inter-element boundaries across which data must be communicated. It turns out that even a simple partitioning can produce a nontrivial topology of the domain and the nontrivial orientation of element boundaries with respect to one another. This information must be explicitly supplied to the algorithm and determined for each domain configuration. I discuss the methods used to deduce the topological connectivity, even in domains with hundreds of elements distributed over dozens of distinct coordinate maps, such as those used for binary black hole simulations. Chapter 2 also discusses work on generic methods for

grid point redistribution within the computational domain in order to better resolve physical phenomena at shorter length scales.

The flexibility of these domain creation methods means that they can be used for problems other than binary mergers. For example, we can construct a domain suitable to simulate a spacetime having an Einstein static universe topology or a wormhole topology with minimal changes to the code. Another application is to construct a domain suitable for modelling the thermal noise in the LIGO mirrors. This application is being pursued by researchers at the Albert Einstein Institute in Potsdam.

1.3 Parameter Estimation

Parameter estimation is the means by which the properties of observed phenomena, such as black holes, are determined and quantified from the measured data. The most important parameters for binary black hole mergers are: the component masses, their spins, the distance from the system to Earth, the orientation of the system on the sky, and the merger time. Each of these are parameters that can be estimated and constrained from the gravitational waveform (GW) data collected by observatories such as LIGO.

1.3.1 Bayesian Inference

Bayesian inference is the method of using Bayes' theorem to construct estimates on the possible values of an observable. In the context of binary mergers, the observables are the parameters of the binary system. Bayesian inference allows us to include reasonable constraints on the parameters based on our previous knowledge—in fact,

it requires us to do so. For example, in the case of neutron stars we might want to include mass constraints based on previous pulsar and X-ray binary observations. In Bayesian inference, this allowed region of parameter space is the space upon which the *prior* is defined. The prior corresponds to the probability distribution of an observed parameter taking on a particular value, based on our previous knowledge. This prior is then updated using observed data, such as the GW data from LIGO, to construct the *posterior*, the new probability distribution of an observed parameter taking on a particular value, once the observed data has been taken into account.

Bayes' theorem is really just a rewriting of the formula for conditional probability:

$$p(\theta|\mathbf{X}, M) = \frac{p(\theta|M)p(\mathbf{X}|\theta, M)}{p(\mathbf{X}|M)}, \tag{1.4}$$

where θ is the set of parameters whose values are being estimated. Here $\mathbf{X}$ is the observed data, $p(\theta|\mathbf{X}, M)$ is the posterior probability distribution of θ given the data $\mathbf{X}$ and model M, $p(\theta|M)$ is the prior probability distribution of θ given M, $p(\mathbf{X}|M)$ is the probability distribution of the data $\mathbf{X}$ given M, and $p(\mathbf{X}|\theta, M)$ is the probability distribution of the data $\mathbf{X}$, given M and a particular value of the parameter θ. Viewed as a function of the parameter θ, $p(\mathbf{X}|\theta, M)$ is referred to as the *likelihood*. Each of these probability distributions is conditional on the choice of model, M, which is often left out of the formulas for brevity. Bayes' theorem tells us how priors and likelihoods are to be put together in order to construct the posterior, the estimate of the parameter given the observed data.

1.3.2 Matched Filtering

Matched filtering involves comparing observed GW waveforms against candidate template waveforms from a model to determine whether the candidate waveforms are a good match for the data. Candidate waveforms, each with various parameters, are constructed and compared against the observed GW waveform to compute a *match statistic*.

The match statistic is typically computed in the frequency domain:

$$\text{match}(h, s) = 4\Re \int_0^\infty df \frac{\tilde{h}^*(f)\tilde{s}(f)}{S_n(f)}, \tag{1.5}$$

where $\tilde{h}(f)$ is the Fourier-domain waveform template, $\tilde{s}$ the Fourier transform of the observed data, and $S_n(f)$ the noise curve corresponding to the detector.

Note that the *signal-to-noise ratio*(SNR) ρ is defined using the match statistic as well:

$$\rho := \frac{\text{match}(h, s)}{\sqrt{\text{match}(h, h)}}, \tag{1.6}$$

ρ is merely the normalized match statistic. For reference, GW150914 was detected with an single-detector SNR of 13 to 20 [5].

It is the match statistic that enters the likelihood calculation that was discussed in the previous section. If one assumes that each detector produces stationary, uncorrelated Gaussian noise, the likelihood is then given by[6]:

$$p(\mathbf{X}|\theta, M) \propto \exp\left[-\frac{1}{2}\sum_{i=1}^{N} \text{match}(n_i, n_i)\right], \tag{1.7}$$

where N is the number of detectors, and n_i is the residual $s_i - h_i$, the strain data s_i minus the gravitational waveform h_i corresponding to the i-th detector. The likelihood

is maximized when the residual is closest to Gaussian noise; if the waveform h_i does not match the strain data s_i, the residual will contain non-noise elements, yielding a smaller likelihood.

1.3.3 Markov Chain Monte Carlo

Markov Chain Monte Carlo (MCMC) is one of the methods by which the posterior probability distribution is obtained from Bayes' theorem. As the posterior can only be computed analytically in a few idealized cases, the posterior is computed numerically via sampling the parameter space on which the distribution is defined, which is made possible by MCMC. The distribution is sampled in *chains*, where each chain is a Markov chain, a series of sampled points in parameter space where each subsequent point in the chain is chosen in a probabilistic manner based only on the previous point. In practice, the subsequent points are constructed from a *proposal probability distibution* $Q(\theta, \theta')$, from which the next sample is proposed, and an *acceptance probability* $A(\theta, \theta')$, which determines whether to accept or reject the proposed point. The acceptance probability is informed by the likelihood $p(\mathbf{X}|\theta, M)$; the distribution of the resulting chain approximates the posterior distribution $p(\theta|\mathbf{X}, M)$ that was desired.

1.3.4 Waveform Models

The waveform models from which candidate waveforms are compared against the strain data are varied in their versatility and practicality. Some are accurate but slow, whereas others sacrifice accuracy for speed. Some may be more accurate than others in certain regions of parameter space.

Simple waveforms can be computed from linearized gravity approximations, which can be used to model the early inspiral. These waveforms can be computed analytically, meaning the parameter space can be explored quickly. On the other hand, the merger portion of the waveform must be omitted as the linearized gravity approximation only holds in the weak-field regime, where the velocities of the black holes are small.

In order to obtain waveforms that are computed directly from the full Einstein's equations, numerical relativity must be used. While these calculations are computationally expensive, the parameter space one can probe is only limited to that which can be stably evolved by current numerical relativity codes.

1.4 Modelling Post-Inspiral Effects in Beyond-GR Waveforms

General relativity describes how two compact objects orbiting each other merge as the result of energy and angular momentum loss via the emission of GWs. As the once-circular orbits shrink, the orbiting frequencies of the compact objects increase rapidly. GR predicts that the rate of energy emission at the point of merger approaches the Planck power scale.[1] It is not currently known whether or not astrophysical phenomena conform to the predictions of GR at this scale. Other fields, predicted by beyond-GR theories, may "turn on" at some point as the rate of energy emission approaches the Planck scale. If additional energy is lost via these new fields, the orbits will close faster, and the merger will occur at an earlier time compared to that predicted by GR.

The Laser Interferometer Gravitational Wave Observatory (LIGO), as seen in

[1]Planck quantities are built by dimensional analysis from c, G, and $\hbar$, and are thought to set the scale of quantum gravity. The Planck power is $c^5/G \sim 10^{60}$ erg sec^{-1}, and happens to be independent of $\hbar$.

Figure 1.1: One of the LIGO detectors. The one pictured is in Livingston, LA; the other detector is in Hanford, WA. [Image: LIGO]

Fig. 1.1, detected the first gravitational wave signal on September 14, 2015[7]. The event, denoted GW150914, consisted of the merger of two ~ 30 solar mass black holes and marked the beginning of the era of gravitational wave astronomy. GW150914 was found to be consistent with general relativity[5].

Dynamical Chern-Simons theory (dCS), in contrast to general relativity, is an example of a beyond-GR theory that predicts the presence of a new scalar field, while other theories predict the presence of vector or even tensor fields. With the variety of beyond-GR theories that exist, it is necessary to systematically test all of them so that the ones that most agree with the current GW data can be identified. Conversely, one would like to rule out theories that disagree. While this is ordinarily done using parameter estimation methods on the GW data using matched filtering against template wave-

forms, this requires the existence of template waveforms for the particular beyond-GR theory being tested. Producing these waveforms requires full numerical simulation of the theory and is only in its early stages. In the meantime, analytical models for deforming the GR waveform into beyond-GR waveforms are being created.

Yunes and Pretorius developed a model that deforms the GR waveform in the inspiral regime. The extension is carried out by adding a new parameter β that determines the leading post-Newtonian order at which a difference from GR shows up. In Chapter 3 of the thesis, I develop an extension of this model into the merger regime. This extension introduces a second parameter ϵ, whose main effect is to change the merger time, mimicking the effect of a theory with additional fields that can dissipate energy. I have used this model, along with the parameter estimation software PyCBC, to perform injection tests demonstrating the recoverability of these parameters from LIGO-like data.

1.5 Future Work: Numerical Relativity beyond General Relativity

Both analytical and numerical models are needed to understand the observations made by LIGO and Virgo. Models are also required for determining the parameters of the sources, such as the mass and spin of the binary companions and the distance to the binary. While the early inspiral regime is well modeled by using the post-Newtonian approximation, where relativistic corrections are added to the Newtonian dynamics of a binary system, this approximation breaks down as gravitational waves carry away energy and decrease the separation between the black holes. In order to compute the trajectory of the last ten to twenty orbits, as well as the merger, numerical methods such as those used in SpECTRE are needed.

With the injection tests completed, and the plausibility of the extended model demonstrated, I plan to use the extended model with the current LIGO data to place constraints on the new parameters introduced in the model. Not only will this research serve as an additional test of GR with the LIGO data, but it will also serve to constrain the behavior of possible beyond-GR theories beyond the inspiral regime. In addition, the infrastructure is in place to test multiple beyond-GR theories that each predict deviations from GR at different leading PN orders. This will be a component of future work as appropriate priors for β and ϵ must be determined for each theory. Parameters corresponding to merger and ringdown effects can also be added to the model, and current numerical work being done by others will be used to guide what these parameters should be. Further along, the spins of these new fields imply different effects on the different modes of the resultant GW. I will look to incorporate the effects of the presence of these fields beyond the effect on the h_{22} mode. Finally, I will continue my work on SpECTRE to extend its capabilities beyond general relativity calculations.

CHAPTER 2

DOMAIN CONSTRUCTION IN SPECTRE[1]

The construction of the computational and physical domains, as well as the mappings that relate the two, are crucial ingredients in any numerical relativity calculation. We discuss the domains and maps that are used in the SpECTRE code, as well as the techniques that were used to construct them, along with the advantages that are gained in using them. We also discuss how these domains may be used in simulations of exotic or otherwise topologically nontrivial spacetimes. We conclude with a discussion of an early binary compact object domain used in SpECTRE.

2.1 Introduction

SpECTRE makes use of the Discontinuous Galerkin (DG) method in its numerical solution of partial differential equations (PDEs). In the DG method, the physical domain is partitioned into smaller elements. In each element, the solution is represented as an expansion in some set of basis functions. If the boundaries of the domain are not very complicated, we can choose the elements to be hexahedral and fit then to the boundaries, possibly with the aid of coordinate maps. In many engineering applications, however, domain boundaries are complicated and require tetrahedral elements to get a good fit. We will not discuss that case here.

The advantage of hexaderal elements is that the basis functions can be chosen to be a tensor product of 1-dimensional basis functions, one along each coordinate direction. This greatly simplifies the computations. Quantities associated with the interior of each element, along with information on the boundaries of the element from neighbor-

[1]This chapter will appear as a technical note in the public repository for the SpECTRE code[1]. Portions of it will appear in an upcoming paper describing the code.

ing elements, then enter and are combined in the DG method to compute the numerical solution.

Hexahedral elements allow us to use Cartesian rectilinear coordinates, the *logical coordinates*, the computational domain in which all DG computations are ultimately performed. While the coordinates in the computational domain are Cartesian, they need not be so in the physical domain if the appropriate *coordinate map* between the domains is provided.

Depending on the geometry of the physical domain, the geometry of the elements that result after partitioning may be nontrivial. For example, in the case of a single black hole domain, the physical domain is spherically symmetric with an excised region inside the black hole; the coordinates used in each element of this domain must map to the Cartesian-like coordinate system in the logical cube, the logical coordinates. In this particular case, the map that brings points in the logical cube to the elements of the single black hole domain in SpECTRE is called the Wedge map.

In this chapter we discuss the various coordinate maps that are used by SpECTRE. We also discuss the domains that they are used by, and the algorithms that are used to ensure that the coordinate systems that are used by each element do not interfere with the calculation of the boundary quantities in the DG method. We close the chapter with a discussion of how these techniques can be used to construct computational domains for physical domains of nontrivial topology.

2.2 Coordinates

2.2.1 Logical Coordinates

The logical coordinates are the coordinates of the *computational domain*, the space on which the basis functions of the DG method are defined. This space makes up the *logical hypercube*, the D-dimensional interval $[-1,1]^D$. The coordinates that parameterize the logical hypercube are given Greek letters. In three dimensions, the coordinates are ξ, η, and ζ. The choice of this interval is made to correspond with the choice of basis functions which also live on the interval $[-1,1]$.

The logical coordinates do not determine the gridpoints of the DG calculation. The locations of the gridpoints are given by the choice of quadrature points in the DG method used. The gridpoints are very rarely equally spaced. For example, using the Legendre-Gauss-Lobatto points, the gridpoints are more closely spaced near the logical element boundaries.

In the case where the physical domain is itself rectilinear and/or has symmetries compatible with a Cartesian coordinate system, the partitioning of the domain into hexahedral elements can be relatively trivial. In the simplest case the identity map is sufficient. In more complicated domains, such as those resembling the spherical domain in Fig. 2.1, multiple maps will be needed, each mapping a logical cube to the corresponding region of the physical domain.

2.2.2 Equiangular Coordinates

Equiangular coordinates are very nearly logical coordinates, in that they also live in the domain of $[-1, 1]$, as logical coordinates do. That is, the domain equiangular coordinates live in is not the physical domain, but some intermediate frame that follows the computatational domain. Equiangular coordinates are used when one wishes to use domains with spherical surfaces, as opposed to flat surfaces, where an affine map would suffice. Points that are equally spaced in equiangular coordinates are also equally spaced in angle, measured by the sphere on whose surface the points lie.

The equiangular map is as follows:

$$\Xi = \tan(\pi\xi/4), \tag{2.1}$$

and has Jacobian:

$$\frac{\mathrm{d}\Xi}{\mathrm{d}\xi} = \frac{\pi}{4}(1 + \Xi^2). \tag{2.2}$$

From the Jacobian it is clear that the equiangular map brings the points near the endpoints of the $[-1, 1]$ domain towards the origin.

Comparing Fig. 2.1 and Fig. 2.2, we can see how the gridpoints in the equidistant coordinates example are more concentrated near the boundaries of the patch. The equiangular map brings these points towards the origin, leading to points that are more uniformly spaced.

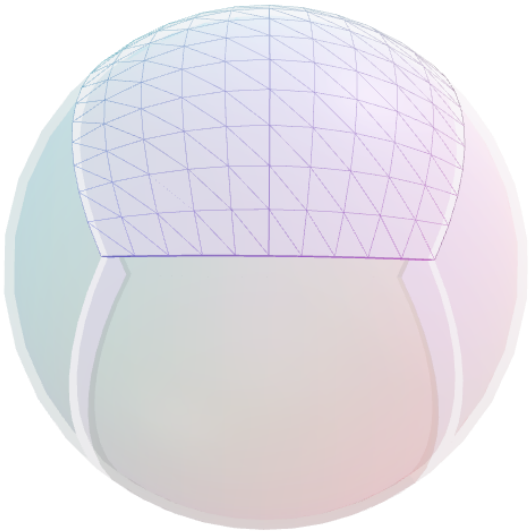

Figure 2.1: A spherical surface patch that where the vertical and horizontal gridlines are equally spaced in equiangular coordinates.

2.2.3 Projective Coordinates

The mapping for any convex quadrilateral defined by the locations of four vertices $\vec{x}_1, \vec{x}_2, \vec{x}_3, \vec{x}_4$ can be obtained by bilinearly interpolating between each one:

$$\vec{x}(\xi,\eta) = \frac{(1-\xi)(1-\eta)}{4}\vec{x}_1 + \frac{(1-\xi)(1+\eta)}{4}\vec{x}_2 + \frac{(1+\xi)(1-\eta)}{4}\vec{x}_3 + \frac{(1+\xi)(1+\eta)}{4}\vec{x}_4. \quad (2.3)$$

In the case of a trapezoid where two of the sides are parallel, it is appropriate to linearly interpolate along the parallel sides. However, linearly interpolating between the two bases results in a less than ideal gridpoint distribution.

As seen in Fig. 2.3 from Veltman's Warp-Off[8], linear interpolation between the two bases results in a uniformly spaced grid between the bases of the frustum. This

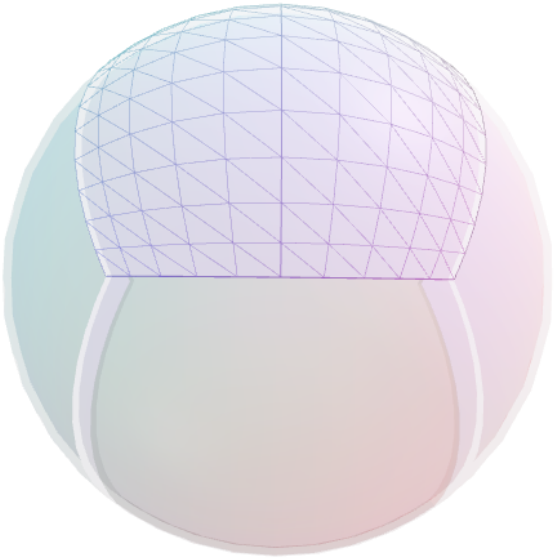

Figure 2.2: A spherical surface patch that where the vertical and horizontal gridlines are equally spaced in equidistant coordinates.

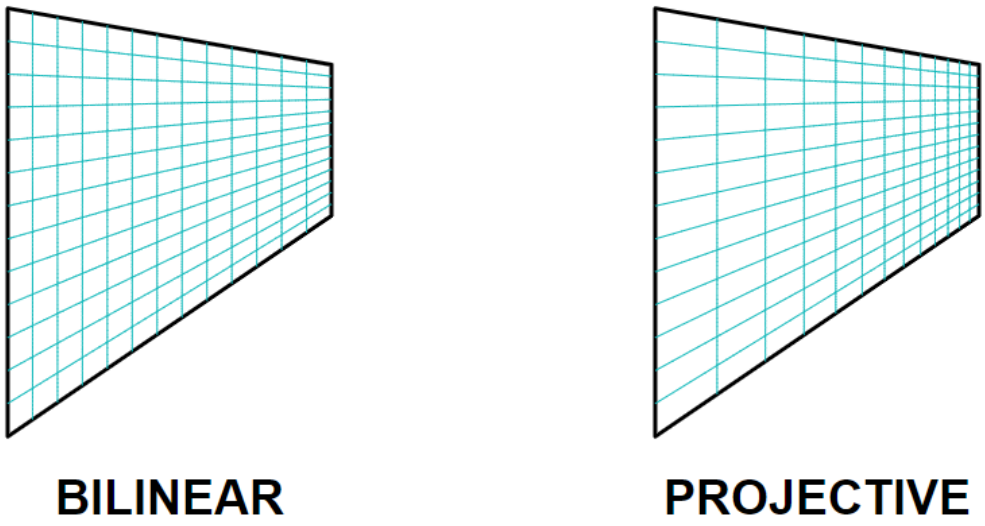

Figure 2.3: The resulting gridpoint locations when they are placed according to either bilinear interpolation between the bounding curves, or according to a projective map which concentrates the gridpoints at one end.

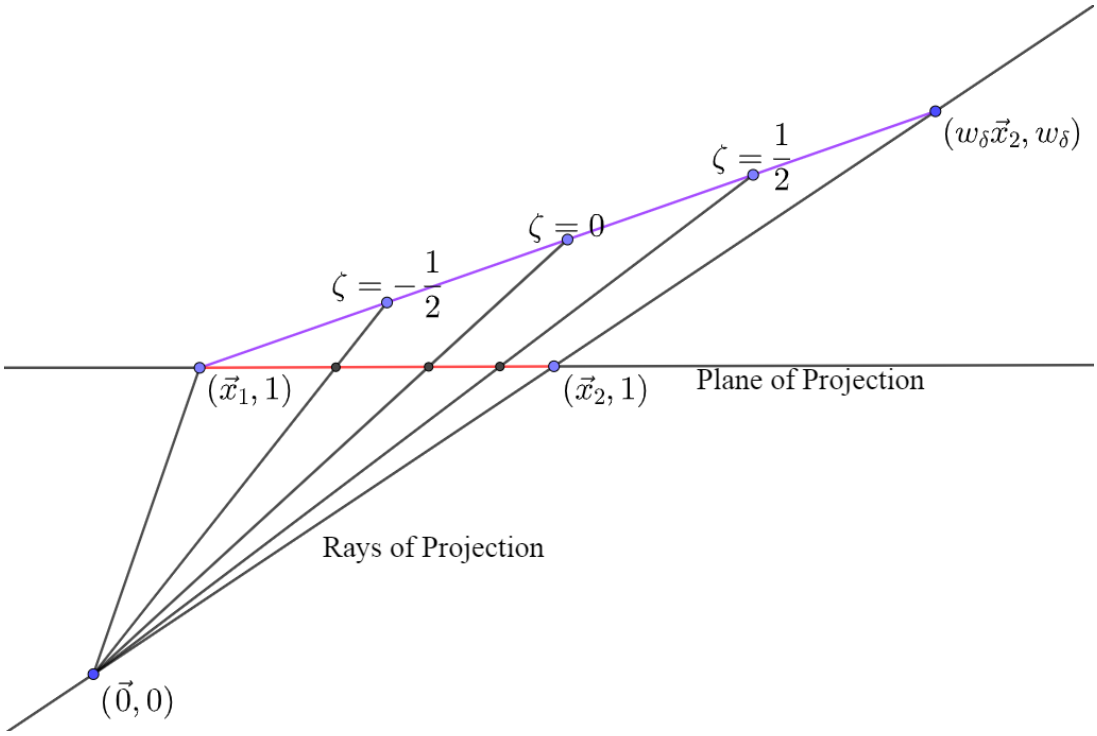

Figure 2.4: The above diagram demonstrates how to obtain a nonlinearly parameterized object (seen in red) from a linearly parameterized one (seen in purple).

causes elements near the smaller base to be longer in the direction normal to the base, and elements near the larger base to be shorter in that direction. We desire elements that have roughly equal sizes along each of their dimensions.

We can redistribute the gridpoints along a chosen direction using a projective map, moving more gridpoints toward the smaller base. We can also see in Fig. 2.3 that too much of a projective map can be applied, leaving elements distorted at the opposite end. From this we can see that it is important to control the degree of projection.

We adapt a technique from projective geometry to obtain the desired grid spacing[9]. The heart of the method is that objects arranged in a line at equal distances from one another will appear to converge as they approach the horizon.

The procedure consists in *lifting* the linearly parameterized object into a higher spa-

tial dimension beyond the canonical Cartesian dimensions of x, y, and z, referred to as w, such that its projection back onto the plane remains unchanged. As seen in Fig. 2.4, the linearly parameterized object exists has zero extent in the w dimension, while the nonlinearly parameterized object (the lifted object) does. The size of the lifted object in the w dimension is controlled by the parameter w_δ, which controls the degree of projection of one end of the object (purple) into the higher spatial dimension w. In projective geometry, these points that exist in the higher dimension are labeled with homogeneous coordinates $\{\tilde{x}, \tilde{y}, \tilde{z}, w\}$, to distinguish them from the Cartesian coordinates that label points that exist on the $w = 1$ hyperplane, $\{x, y, z\}$. The resulting grid (seen in red) is obtained by projecting back into the $w = 1$ hyperplane. The Cartesian coordinates are obtained by dividing each homogeneous coordinate of the linearly parameterized object by its respective w coordinate value.

The parametric equation for the purple object seen above in homogeneous coordinates is:

$$\begin{bmatrix} \tilde{x} \\ \tilde{y} \\ \tilde{z} \\ w \end{bmatrix} = \frac{1-\zeta}{2} \begin{bmatrix} x_1 \\ y_1 \\ z_1 \\ 1 \end{bmatrix} + \frac{1+\zeta}{2} \begin{bmatrix} x_2 w_\delta \\ y_2 w_\delta \\ z_2 w_\delta \\ w_\delta \end{bmatrix}. \tag{2.4}$$

The equation for the red object in Cartesian coordinates is obtained by dividing by w:

$$\vec{x}(\zeta) = \frac{1}{w(\zeta)} \begin{bmatrix} \tilde{x}(\zeta) \\ \tilde{y}(\zeta) \\ \tilde{z}(\zeta) \end{bmatrix}. \tag{2.5}$$

We can recast this equation into a form similar to that of linear interpolation, where the interpolation is done in the auxilliary variable Z:

$$\mathrm{Z}(\zeta) = \frac{(w_\delta - 1) + \zeta(w_\delta + 1)}{(w_\delta + 1) + \zeta(w_\delta - 1)}. \tag{2.6}$$

With this choice of Z, the mapping to projective coordinates then becomes:

$$\vec{x}(\zeta) = \frac{1 - \mathrm{Z}(\zeta)}{2}\vec{x_1} + \frac{1 + \mathrm{Z}(\zeta)}{2}\vec{x_2}, \tag{2.7}$$

2.2.4 Choice of Coordinates

In a typical SpECTRE computation, the fields that are being computed (metric quantities, thermodynamic quantities, etc.) have features at many scales that must be resolved. In these kinds of computations a uniform distribution of gridpoints leaves some regions under-resolved, and other regions with excess computational resources being expended on already-resolved features. For these types of problems, we allow different regions of the domain to take on different refinement levels, corresponding to the level of resolution that is needed to accurately compute the fields in question.

The mapping of the logical coordinates from the computational domain to the physical domain, along with the locations of the quadrature points in these coordinates, determine the location of the gridpoints in the physical domain. In finite element analysis this is referred to as r-refinement. r-refinement is used to redistribute gridpoints in the physical domain towards regions where higher resolution is needed. Other methods of increasing resolution, including h-refinement, where the elements are subdivided into multiple elements, and p-refinement, where the number of quadrature points is increased, are more commonly deployed in SpECTRE, but r-refinement is convenient in situations where the nature of the refinement desired can be expressed analytically.

Examples of where r-refinement is appropriate are in the Wedge map and in the Frustum map. Under the equiangular choice of coordinates, equal coordinate distances

correspond to equal angular distances, leading to a more uniform grid spacing than was possible with the equidistant choice of coordinates alone. In the Frustum map, the projective coordinates are used to correct for the distortion incurred by using a bilinear mapping with two bases of disparate lengths. The projection map allows the gridpoints to be redistributed more uniformly despite this effect.

2.3 Coordinate Maps

2.3.1 Wedge Map

The Wedge map is the primary map used in the two-dimensional Disk and three-dimensional Sphere and Shell domains.[10] The main purpose of the Wedge map is to serve as a transition between a Cartesian-like space, such as the logical coordinates, and a coordinate system that more readily respects the symmetries of the sphere and has its boundaries conform to it.

The Wedge map makes use of the equiangular coordinates in its mapping as they readily conform to the spherical surface shape [11]. Before discussing the fully generalized Wedge3D, let us recall the map in its simplest form, obtained by interpolating between two parameterized surfaces. The first of these is the upper $+z$ surface of a cube of side length $2L$ centered at the origin:

$$\vec{\sigma}_{\text{cubical}}(\xi,\eta) = L \begin{bmatrix} \xi \\ \eta \\ 1 \end{bmatrix}. \tag{2.8}$$

The second of these is the above surface projected onto a sphere of radius R, also cen-

tered at the origin:

$$\vec{\sigma}_{\text{spherical}}(\xi,\eta) = \frac{R}{\sqrt{1+\xi^2+\eta^2}} \begin{bmatrix} \xi \\ \eta \\ 1 \end{bmatrix}. \tag{2.9}$$

In general, a map parameterizing the volume between two surfaces can be obtained by interpolating in a third logical coordinate ζ:

$$\vec{x}(\xi,\eta,\zeta) = \frac{1+\zeta}{2}\vec{\sigma}_{cubical}(\xi,\eta) + \frac{1-\zeta}{2}\vec{\sigma}_{spherical}(\xi,\eta). \tag{2.10}$$

To obtain a vanilla Wedge3D one interpolates between the surface of a cube of side length $2L$ and a sphere of radius R:

$$\vec{x}(\xi,\eta,\zeta) = \left\{ \frac{1+\zeta}{2}L + \frac{1-\zeta}{2}\frac{R}{\sqrt{1+\xi^2+\eta^2}} \right\} \begin{bmatrix} \xi \\ \eta \\ 1 \end{bmatrix}. \tag{2.11}$$

2.3.2 Bulged Cube Map

The volume map from the cube to a bulged cube is obtained by interpolating between six surface maps, twelve bounding curves, and eight corners[12]. The surface map for the upper $+z$ axis is obtained by interpolating between a cubical surface and a spherical surface. The two surfaces are chosen such that the sphere circumscribes the cube. We make a choice here as to whether we wish to use the logical coordinates parameterizing these surfaces as they are, in which case we have the equidistant choice of coordinates, or whether to apply a tangent map to them which leads us to the equiangular choice of coordinates. In terms of the logical coordinates, the equiangular coordinates are:

Figure 2.5: A cut-away of the Shell domain, made up of six Wedges, with one of the Wedges shown in wireframe. The inner face of each Wedge is spherical; the excised region removes the black hole singularity from the domain of the computation.

$$\text{equiangular xi} : \Xi(\xi) = \tan(\xi\pi/4), \tag{2.12}$$

$$\text{equiangular eta} : \mathrm{H}(\eta) = \tan(\eta\pi/4). \tag{2.13}$$

The derivatives are

$$\Xi'(\xi) = \frac{\pi}{4}(1 + \Xi^2), \tag{2.14}$$

$$\mathrm{H}'(\eta) = \frac{\pi}{4}(1 + \mathrm{H}^2). \tag{2.15}$$

The equidistant Ξ and H coordinates are simply the logical coordinates ξ and η.

We also define the variable ρ, given by:

$$\rho = \sqrt{1 + \Xi^2 + \mathrm{H}^2}. \tag{2.16}$$

The Spherical Face Map

The surface map for the spherical face of radius R lying in the $+z$ direction in either choice of coordinates is then given by:

$$\vec{\sigma}_{\text{spherical}}(\xi, \eta) = \begin{bmatrix} x(\xi, \eta) \\ y(\xi, \eta) \\ z(\xi, \eta) \end{bmatrix} = \frac{R}{\rho} \begin{bmatrix} \Xi \\ \mathrm{H} \\ 1 \end{bmatrix}. \tag{2.17}$$

The Cubical Face Map

The surface map for the cubical face of side length $2L$ lying in the $+z$ direction is given by:

$$\vec{\sigma}_{\text{cubical}}(\xi, \eta) = \begin{bmatrix} x(\xi, \eta) \\ y(\xi, \eta) \\ L \end{bmatrix} = L \begin{bmatrix} \Xi \\ \mathrm{H} \\ 1 \end{bmatrix}. \tag{2.18}$$

The Bulged Face Map

To construct the bulged map we interpolate between a cubical face map of side length $2L$ and a spherical face map of radius R, with the interpolation parameter being s, the 'sphericity'. The surface map for the bulged face lying in the $+z$ direction is then given

by:

$$\vec{\sigma}_{+\zeta}(\xi,\eta) = \left\{(1-s)L + \frac{sR}{\rho}\right\} \begin{bmatrix} \Xi \\ \mathrm{H} \\ 1 \end{bmatrix}. \tag{2.19}$$

This equation defines the upper-z map $\vec{\sigma}_{+\zeta}$, and we similarly define the other five surface maps $\vec{\sigma}_{+\eta}$, $\vec{\sigma}_{+\xi}$, and so on by appropriate rotations. We constrain L by demanding that the spherical face circumscribe the cube. With this condition, we have $L = R/\sqrt{3}$.

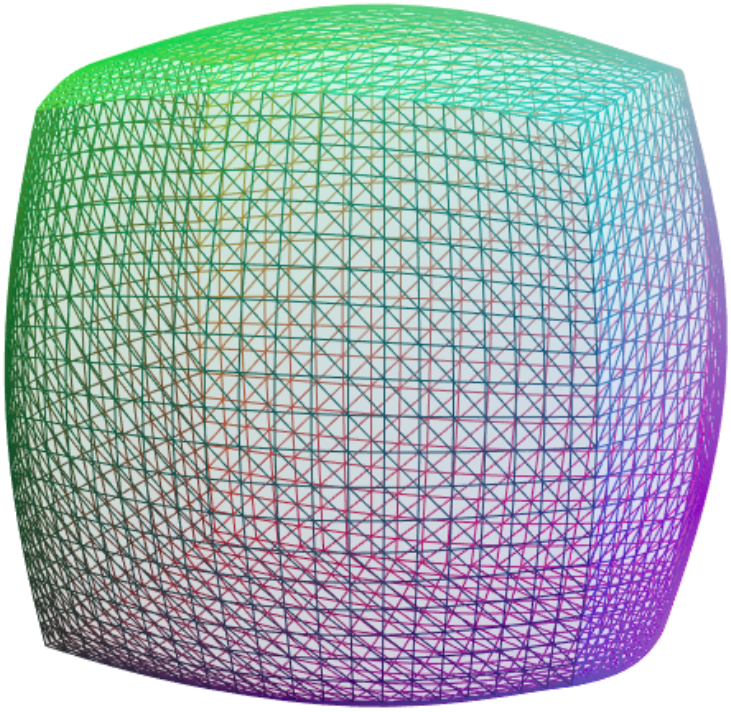

Figure 2.6: An element after the Bulged Cube map has been applied. The Bulged Cube is constructed by interpolating between six Wedge surfaces, and is used for neutron star domains.

The General Formula for 3D Isoparametric Maps

The general formula is given by Eq. 1 in section 2.1 of a paper by Hesthaven [13].

Hesthaven's formula is general in the degree of the shape functions used, so for our purposes we take the special case where the shape functions are linear in the interpolation variable, and define new variables accordingly. However, our interpolation variables do not necessarily have to be the logical coordinates themselves, though they often are. To make this distinction clear, we will define the new interpolation variables $\{\tilde{\xi}, \tilde{\eta}, \tilde{\zeta}\}$, which may either be the logical coordinates themselves or an invertible transformation of them. For the purposes of the bulged cube map, this transformation will be the same transformation that takes the logical coordinates into the equiangular coordinates. We will later see how this choice can lead to simplifications in the final map. We define the following variables for $\alpha, \beta, \gamma \in \{\tilde{\xi}, \tilde{\eta}, \tilde{\zeta}\}$:

$$f_{\alpha}^{\pm} = \frac{1}{2}(1 \pm \alpha), \tag{2.20}$$

$$f_{\alpha\,\beta}^{\pm\pm} = \frac{1}{4}(1 \pm \alpha)(1 \pm \beta), \tag{2.21}$$

$$f_{\alpha\,\beta\,\gamma}^{\pm\pm\pm} = \frac{1}{8}(1 \pm \alpha)(1 \pm \beta)(1 \pm \gamma). \tag{2.22}$$

The formula involves six surfaces, which we will denote by $\vec{\sigma}$, twelve curves, denoted by $\vec{\Gamma}$, and eight vertices, denoted by $\vec{\pi}$, with the subscripts denoting which face(s) these

objects belong to. The full volume map is given by:

$$\begin{aligned}\vec{x}(\xi,\eta,\zeta) =& f^{+}_{\tilde{\zeta}}\vec{\sigma}_{+\zeta}(\xi,\eta) + f^{-}_{\tilde{\zeta}}\vec{\sigma}_{-\zeta}(\xi,\eta) \\ &+ f^{+}_{\tilde{\eta}}\vec{\sigma}_{+\eta}(\xi,\zeta) + f^{-}_{\tilde{\eta}}\vec{\sigma}_{-\eta}(\xi,\zeta) + f^{+}_{\tilde{\xi}}\vec{\sigma}_{+\xi}(\eta,\zeta) + f^{-}_{\tilde{\xi}}\vec{\sigma}_{-\xi}(\eta,\zeta) \\ &- f^{++}_{\tilde{\xi}\,\tilde{\eta}}\vec{\Gamma}_{+\xi+\eta}(\zeta) - f^{-+}_{\tilde{\xi}\,\tilde{\eta}}\vec{\Gamma}_{-\xi+\eta}(\zeta) - f^{+-}_{\tilde{\xi}\,\tilde{\eta}}\vec{\Gamma}_{+\xi-\eta}(\zeta) - f^{--}_{\tilde{\xi}\,\tilde{\eta}}\vec{\Gamma}_{-\xi-\eta}(\zeta) \\ &- f^{++}_{\tilde{\xi}\,\tilde{\zeta}}\vec{\Gamma}_{+\xi+\zeta}(\eta) - f^{-+}_{\tilde{\xi}\,\tilde{\zeta}}\vec{\Gamma}_{-\xi+\zeta}(\eta) - f^{+-}_{\tilde{\xi}\,\tilde{\zeta}}\vec{\Gamma}_{+\xi-\zeta}(\eta) - f^{--}_{\tilde{\xi}\,\tilde{\zeta}}\vec{\Gamma}_{-\xi-\zeta}(\eta) \\ &- f^{++}_{\tilde{\eta}\,\tilde{\zeta}}\vec{\Gamma}_{+\eta+\zeta}(\xi) - f^{-+}_{\tilde{\eta}\,\tilde{\zeta}}\vec{\Gamma}_{-\eta+\zeta}(\xi) - f^{+-}_{\tilde{\eta}\,\tilde{\zeta}}\vec{\Gamma}_{+\eta-\zeta}(\xi) - f^{--}_{\tilde{\eta}\tilde{\zeta}}\vec{\Gamma}_{-\eta-\zeta}(\xi) \\ &+ f^{+++}_{\tilde{\xi}\,\tilde{\eta}\,\tilde{\zeta}}\vec{\pi}_{+\xi+\eta+\zeta} + f^{-++}_{\tilde{\xi}\,\tilde{\eta}\,\tilde{\zeta}}\vec{\pi}_{-\xi+\eta+\zeta} + f^{+-+}_{\tilde{\xi}\,\tilde{\eta}\,\tilde{\zeta}}\vec{\pi}_{+\xi-\eta+\zeta} + f^{--+}_{\tilde{\xi}\,\tilde{\eta}\,\tilde{\zeta}}\vec{\pi}_{-\xi-\eta+\zeta} \\ &+ f^{++-}_{\tilde{\xi}\,\tilde{\eta}\,\tilde{\zeta}}\vec{\pi}_{+\xi+\eta-\zeta} + f^{-+-}_{\tilde{\xi}\,\tilde{\eta}\,\tilde{\zeta}}\vec{\pi}_{-\xi+\eta-\zeta} + f^{+--}_{\tilde{\xi}\,\tilde{\eta}\,\tilde{\zeta}}\vec{\pi}_{+\xi-\eta-\zeta} + f^{---}_{\tilde{\xi}\,\tilde{\eta}\,\tilde{\zeta}}\vec{\pi}_{-\xi-\eta-\zeta}.\end{aligned} \tag{2.23}$$

The Special Case for Octahedral Symmetry

The general formula is for the case in which there are six independently specified bounding surfaces. In octahedral symmetry, the surfaces are obtained by rotations and reflections of the upper-ζ face.

We define the matrices corresponding to these transformations to be:

$$S_{xy} = \begin{bmatrix} 0 & 1 & 0 \\ 1 & 0 & 0 \\ 0 & 0 & 1 \end{bmatrix}, S_{xz} = \begin{bmatrix} 0 & 0 & 1 \\ 0 & 1 & 0 \\ 1 & 0 & 0 \end{bmatrix}, S_{yz} = \begin{bmatrix} 1 & 0 & 0 \\ 0 & 0 & 1 \\ 0 & 1 & 0 \end{bmatrix}, \tag{2.24}$$

$$C_{zxy} = \begin{bmatrix} 0 & 0 & 1 \\ 1 & 0 & 0 \\ 0 & 1 & 0 \end{bmatrix}, C_{yzx} = \begin{bmatrix} 0 & 1 & 0 \\ 0 & 0 & 1 \\ 1 & 0 & 0 \end{bmatrix}, \tag{2.25}$$

$$N_x = \begin{bmatrix} -1 & 0 & 0 \\ 0 & 1 & 0 \\ 0 & 0 & 1 \end{bmatrix}, N_y = \begin{bmatrix} 1 & 0 & 0 \\ 0 & -1 & 0 \\ 0 & 0 & 1 \end{bmatrix}, N_z = \begin{bmatrix} 1 & 0 & 0 \\ 0 & 1 & 0 \\ 0 & 0 & -1 \end{bmatrix}. \tag{2.26}$$

The surface maps can now all be written in terms of $\vec{\sigma}_{+\zeta}$ and these matrices:

$$\begin{aligned} \vec{\sigma}_{-\zeta}(\xi,\eta) =& N_z \vec{\sigma}_{+\zeta}(\xi,\eta) \\ \vec{\sigma}_{+\eta}(\xi,\zeta) =& S_{yz} \vec{\sigma}_{+\zeta}(\xi,\zeta) \\ \vec{\sigma}_{-\eta}(\xi,\zeta) =& N_y S_{yz} \vec{\sigma}_{+\zeta}(\xi,\zeta) \\ \vec{\sigma}_{+\xi}(\eta,\zeta) =& C_{zxy} \vec{\sigma}_{+\zeta}(\eta,\zeta) \\ \vec{\sigma}_{-\xi}(\eta,\zeta) =& N_x C_{zyx} \vec{\sigma}_{+\zeta}(\eta,\zeta). \end{aligned} \tag{2.27}$$

The four bounding curves $\vec{\Gamma}$ on the $+\zeta$ face are given by:

$$\vec{\Gamma}_{+\xi,+\zeta}(\eta) = \vec{\sigma}_{+\zeta}(+1,\eta) \tag{2.28}$$

$$\vec{\Gamma}_{-\xi,+\zeta}(\eta) = \vec{\sigma}_{+\zeta}(-1,\eta) = N_x \vec{\sigma}_{+\zeta}(+1,\eta) \tag{2.29}$$

$$\vec{\Gamma}_{+\eta,+\zeta}(\xi) = \vec{\sigma}_{+\zeta}(\xi,+1) = S_{xy} \vec{\sigma}_{+\zeta}(+1,\xi) \tag{2.30}$$

$$\vec{\Gamma}_{-\eta,+\zeta}(\xi) = \vec{\sigma}_{+\zeta}(\xi,-1) = N_y S_{xy} \vec{\sigma}_{+\zeta}(+1,\xi) \tag{2.31}$$

The bounding curves on the other surfaces can be obtained by transformations on the $+\zeta$ face:

$$\vec{\Gamma}_{+\xi,-\zeta}(\eta) = N_z\vec{\sigma}_{+\zeta}(+1,\eta) \tag{2.32}$$

$$\vec{\Gamma}_{-\xi,-\zeta}(\eta) = N_z\vec{\sigma}_{+\zeta}(-1,\eta) = N_zN_x\vec{\sigma}_{+\zeta}(+1,\eta) \tag{2.33}$$

$$\vec{\Gamma}_{+\eta,-\zeta}(\xi) = N_z\vec{\sigma}_{+\zeta}(\xi,+1) = N_zS_{xy}\vec{\sigma}_{+\zeta}(+1,\xi) \tag{2.34}$$

$$\vec{\Gamma}_{-\eta,-\zeta}(\xi) = N_z\vec{\sigma}_{+\zeta}(\xi,-1) = N_zN_yS_{xy}\vec{\sigma}_{+\zeta}(+1,\xi) \tag{2.35}$$

$$\vec{\Gamma}_{+\xi,+\eta}(\zeta) = C_{zxy}\vec{\sigma}_{+\zeta}(+1,\zeta) \tag{2.36}$$

$$\vec{\Gamma}_{-\xi,+\eta}(\zeta) = N_xC_{zxy}\vec{\sigma}_{+\zeta}(+1,\zeta) \tag{2.37}$$

$$\vec{\Gamma}_{+\xi,-\eta}(\zeta) = C_{zxy}\vec{\sigma}_{+\zeta}(-1,\zeta) = C_{zxy}N_x\vec{\sigma}_{+\zeta}(+1,\zeta) \tag{2.38}$$

$$\vec{\Gamma}_{-\xi,-\eta}(\zeta) = N_xC_{zxy}\vec{\sigma}_{+\zeta}(-1,\zeta) = N_xC_{zxy}N_x\vec{\sigma}_{+\zeta}(+1,\zeta) \tag{2.39}$$

Now we can write the volume map in terms of $\vec{\sigma}_{+\zeta}$ only:

$$\begin{aligned}
\vec{x}(\xi,\eta,\zeta) = {} & (f^+_{\tilde{\zeta}} + f^-_{\tilde{\zeta}}N_z)\vec{\sigma}_{+\zeta}(\xi,\eta) \\
& + (f^+_{\tilde{\eta}} + f^-_{\tilde{\eta}}N_y)S_{yz}\vec{\sigma}_{+\zeta}(\xi,\zeta) \\
& + (f^+_{\tilde{\xi}} + f^-_{\tilde{\xi}}N_x)C_{zxy}\vec{\sigma}_{+\zeta}(\eta,\zeta) \\
& - (f^+_{\tilde{\xi}} + f^-_{\tilde{\xi}}N_x)(f^+_{\tilde{\eta}} + f^-_{\tilde{\eta}}N_y)C_{zxy}\vec{\sigma}_{+\zeta}(+1,\zeta) \\
& - (f^+_{\tilde{\zeta}} + f^-_{\tilde{\zeta}}N_z)\left\{(f^+_{\tilde{\xi}} + f^-_{\tilde{\xi}}N_x)\vec{\sigma}_{+\zeta}(+1,\eta) + (f^+_{\tilde{\eta}} + f^-_{\tilde{\eta}}N_y)S_{xy}\vec{\sigma}_{+\zeta}(+1,\xi)\right\} \\
& + \frac{r}{\sqrt{3}}\vec{\tilde{\xi}}
\end{aligned}$$

Note that we can now absorb all of the fs into the matrix prefactors in the above equation and obtain a final set of matrices. We define the following "blending matrices":

$$B_{\tilde{\xi}} = \begin{bmatrix} 0 & 0 & \tilde{\xi} \\ 1 & 0 & 0 \\ 0 & 1 & 0 \end{bmatrix}, B_{\tilde{\eta}} = \begin{bmatrix} 1 & 0 & 0 \\ 0 & 0 & \tilde{\eta} \\ 0 & 1 & 0 \end{bmatrix}, B_{\tilde{\zeta}} = \begin{bmatrix} 1 & 0 & 0 \\ 0 & 1 & 0 \\ 0 & 0 & \tilde{\zeta} \end{bmatrix} \tag{2.40}$$

$$B_{\tilde{\xi}\tilde{\eta}} = \begin{bmatrix} 0 & 0 & \tilde{\xi} \\ \tilde{\eta} & 0 & 0 \\ 0 & 1 & 0 \end{bmatrix}, B_{\tilde{\xi}\tilde{\zeta}} = \begin{bmatrix} \tilde{\xi} & 0 & 0 \\ 0 & 1 & 0 \\ 0 & 0 & \tilde{\zeta} \end{bmatrix}, B_{\tilde{\eta}\tilde{\zeta}} = \begin{bmatrix} 0 & 1 & 0 \\ \tilde{\eta} & 0 & 0 \\ 0 & 0 & \tilde{\zeta} \end{bmatrix} \tag{2.41}$$

$$B_{\tilde{\xi}\tilde{\eta}\tilde{\zeta}} = \begin{bmatrix} \tilde{\xi} & 0 & 0 \\ 0 & \tilde{\eta} & 0 \\ 0 & 0 & \tilde{\zeta} \end{bmatrix} \tag{2.42}$$

Now we can write the volume map in these terms:

$$\begin{aligned} \vec{x}(\xi,\eta,\zeta) = & B_{\tilde{\zeta}}\vec{\sigma}_{+\zeta}(\xi,\eta) \\ & + B_{\tilde{\eta}}\vec{\sigma}_{+\zeta}(\xi,\zeta) + B_{\tilde{\xi}}\vec{\sigma}_{+\zeta}(\eta,\zeta) \\ & - B_{\tilde{\xi}\tilde{\eta}}\vec{\sigma}_{+\zeta}(+1,\zeta) - B_{\tilde{\xi}\tilde{\zeta}}\vec{\sigma}_{+\zeta}(+1,\eta) + B_{\tilde{\eta}\tilde{\zeta}}\vec{\sigma}_{+\zeta}(+1,\xi) \\ & + B_{\tilde{\xi}\tilde{\eta}\tilde{\zeta}}\vec{\sigma}_{+\zeta}(+1,+1) \end{aligned}$$

The Bulged Cube Map

We now use the result above to provide the mapping for the bulged cube. First we will define the variables ρ_A and ρ_{AB}, for $A, B \in \{\Xi, \mathrm{H}, \mathrm{Z}\}$, where Z is $\tan(\zeta\pi/4)$ in the equiangular case and ζ in the equidistant case:

$$\rho_A = \sqrt{2 + A^2}\ \rho_{AB} = \sqrt{1 + A^2 + B^2} \tag{2.43}$$

The final mapping is then:

$$\begin{aligned}\vec{x}(\xi,\eta,\zeta) = \frac{(1-s)R}{\sqrt{3}}\begin{bmatrix}\Xi\\ \mathrm{H}\\ \mathrm{Z}\end{bmatrix} + \frac{sR}{\sqrt{3}}\begin{bmatrix}\tilde{\xi}\\ \tilde{\eta}\\ \tilde{\zeta}\end{bmatrix} \\ + sR\begin{bmatrix}\tilde{\xi} & \Xi & \Xi\\ \mathrm{H} & \tilde{\eta} & \mathrm{H}\\ \mathrm{Z} & \mathrm{Z} & \tilde{\zeta}\end{bmatrix}\begin{bmatrix}1/\rho_{\mathrm{HZ}}\\ 1/\rho_{\Xi\mathrm{Z}}\\ 1/\rho_{\Xi\mathrm{H}}\end{bmatrix} \\ - sR\begin{bmatrix}\Xi & \tilde{\xi} & \tilde{\xi}\\ \tilde{\eta} & \mathrm{H} & \tilde{\eta}\\ \tilde{\zeta} & \tilde{\zeta} & \mathrm{Z}\end{bmatrix}\begin{bmatrix}1/\rho_{\Xi}\\ 1/\rho_{\mathrm{H}}\\ 1/\rho_{\mathrm{Z}}\end{bmatrix}.\end{aligned} \tag{2.44}$$

Recall that the lower case Greek letters with tildes are the variables used for the linear interpolation between the six bounding surfaces, and that the upper case Greek letters are the coordinates along these surfaces, both of which can be specified to be either equidistant or equiangular. In the case where the interpolation variable is chosen to match that of the coordinates along the surface, we have $\tilde{\xi} = \Xi$, etc. In this case, the formula reduces further. The reduced formula below is the one used for this CoordinateMap. It is given by:

$$\vec{x}(\xi,\eta,\zeta) = \left\{\frac{R}{\sqrt{3}} + sR\left(1/\rho_{\mathrm{HZ}} + 1/\rho_{\Xi\mathrm{Z}} + 1/\rho_{\Xi\mathrm{H}} - 1/\rho_{\Xi} - 1/\rho_{\mathrm{H}} - 1/\rho_{\mathrm{Z}}\right)\right\}\begin{bmatrix}\Xi\\ \mathrm{H}\\ \mathrm{Z}\end{bmatrix}. \tag{2.45}$$

The inverse mapping is analytic in the angular directions. However, a root find must be performed for the inverse mapping in the radial direction. This one-dimensional formula is obtained by taking the magnitude of both sides of the mapping, changing variables from ξ, η, ζ to x, y, z, and introducing $\rho^2 := \sqrt{\xi^2 + \eta^2 + \zeta^2}$.

2.3.3 The Special Mobius Map

A general Mobius transformation is a function on the complex plane, and takes the form

$$f(z) = \frac{az + b}{cz + d}, \tag{2.46}$$

where $z, a, b, c, d \in \mathbf{C}$, and $ad - bc \neq 0$. The special case used in this map is the function

$$f(z) = \frac{z - \mu}{1 - z\mu}, \tag{2.47}$$

where μ is real. This map has the properties that the unit disk in the complex plane is mapped to itself, that the x-axis is mapped to itself, and that $f(\mu) = 0$[14]. We will use it to map the unit ball to itself.

This map depends on a single parameter μ, which is the x-coordinate of the preimage of the origin under the map. This map has the fixed points $x = 1$ and $x = -1$. The map is singular for $\mu = 1$ but we have found that the map is accurate up to 12 decimal places for values of μ up to 0.96.

We define the auxiliary variables

$$r := \sqrt{x^2 + y^2 + z^2} \tag{2.48}$$

and

$$\lambda := \frac{1}{1 - 2x\mu + \mu^2 r^2}. \tag{2.49}$$

The map corresponding to this transformation in cartesian coordinates is then given by:

$$\vec{x}'(x, y, z) = \lambda \begin{bmatrix} x(1 + \mu^2) - \mu(1 + r^2) \\ y(1 - \mu^2) \\ z(1 - \mu^2) \end{bmatrix}. \tag{2.50}$$

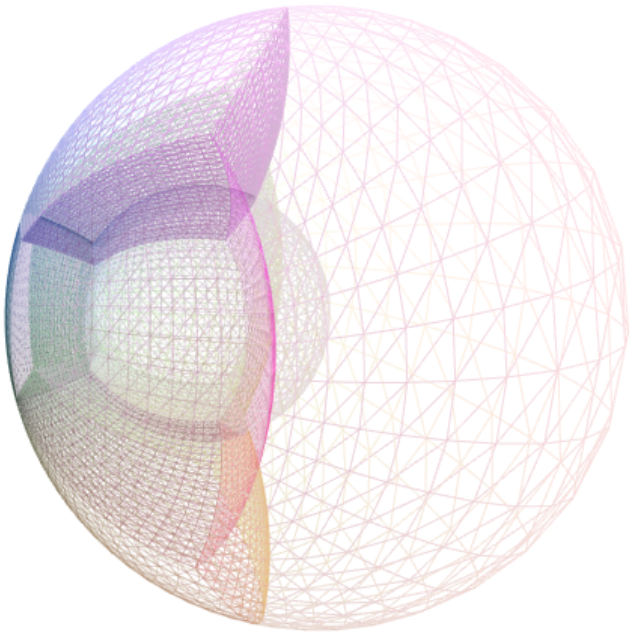

Figure 2.7: A Shell domain where an additional Special Mobius map has been applied. This map preserves the spherical shape of the domain while redistributing gridpoints away from one pole and towards the opposite pole.

The inverse map is the same as the forward map with μ replaced by $-\mu$.

This map is intended to be used only inside the unit sphere. A point inside the unit sphere maps to another point inside the unit sphere. The map can have undesirable behavior at certain points outside the unit sphere: The map is singular at $(x, y, z) = (1/\mu, 0, 0)$ (which is outside the unit sphere since $|\mu| < 1$). Moreover, a point on the x-axis arbitrarily close to the singularity maps to an arbitrarily large value on the $\pm x$-axis, where the sign depends on which side of the singularity the point is on.

The three-dimensional version of this map is obtained by rotating the disk in the plane about the x-axis.

This map is useful for performing transformations along the x-axis that preserve

the unit disk. A concrete example of this is in the BBH domain, where two BBHs with a center-of-mass at $x = \mu$ can be shifted such that the new center of mass is now located at $x = 0$. Additionally, the spherical shape of the outer wave-zone is preserved and, as a Mobius map, the spherical coordinate shapes of the black holes are also preserved.

2.3.4 The Frustum Map

A Frustum map is a map from the logical cube to the volume determined by interpolating between two parallel rectangles each perpendicular to the z-axis[15]. A Frustum map $\vec{x}(\xi, \eta, \zeta)$ is determined by specifying two heights $z_1 =$ `lower_bound` and $z_2 =$ `upper_bound` for the positions of the rectangular bases of the frustum along the $z-$axis, while the sizes of the rectangles are determined by the eight values passed to `face_vertices`:

$$\begin{aligned}
&\text{lower x upper base} : x^{+\zeta}_{-\xi,-\eta} = x(-1,-1,1)\\
&\text{lower x lower base} : x^{-\zeta}_{-\xi,-\eta} = x(-1,-1,-1)\\
&\text{upper x upper base} : x^{+\zeta}_{+\xi,+\eta} = x(1,1,1)\\
&\text{upper x lower base} : x^{-\zeta}_{+\xi,+\eta} = x(1,1,-1)\\
&\text{lower y upper base} : y^{+\zeta}_{-\xi,-\eta} = y(-1,-1,1)\\
&\text{lower y lower base} : y^{-\zeta}_{-\xi,-\eta} = y(-1,-1,-1)\\
&\text{upper y upper base} : y^{+\zeta}_{+\xi,+\eta} = y(1,1,1)\\
&\text{upper y lower base} : y^{-\zeta}_{+\xi,+\eta} = y(1,1,-1).
\end{aligned}$$

As an example, consider a frustum along the z-axis, with the lower base starting at $(x, y) = (-2.0, 3.0)$ and extending to $(2.0, 5.0)$, and with the upper base extend-

ing from $(0.0, 1.0)$ to $(1.0, 3.0)$. The corresponding values for `face_vertices` are `{{{{-2.0,3.0}}, {{2.0,5.0}}, {{0.0,1.0}}, {{1.0,3.0}}}}`.

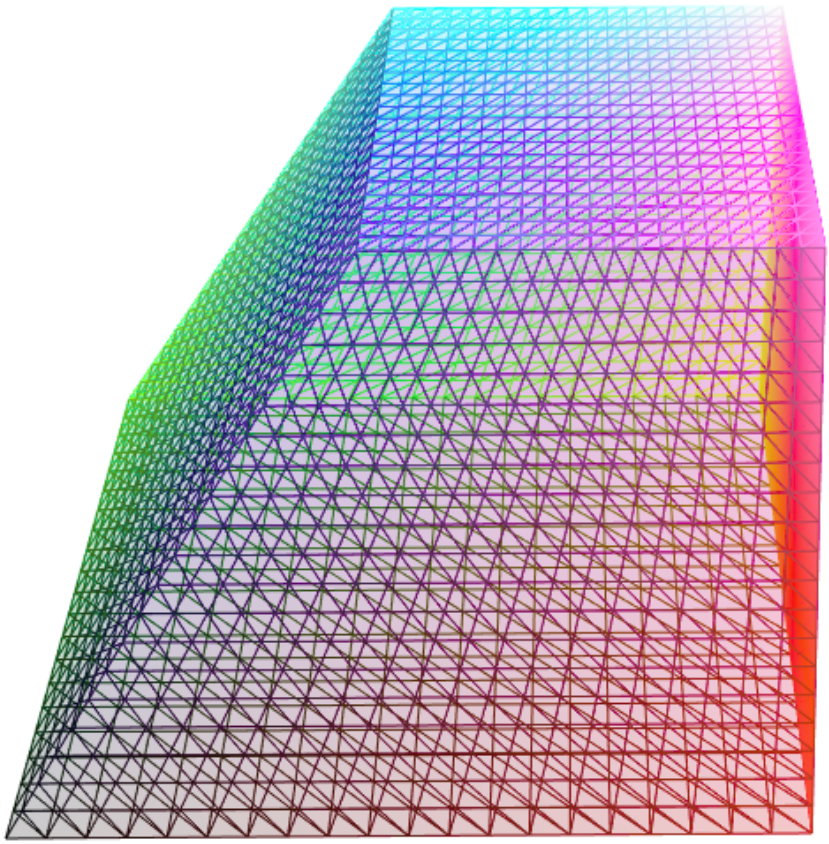

Figure 2.8: A frustum with rectangular bases.

In the case where the two rectangles are geometrically similar, the volume formed is a geometric frustum. However, this coordinate map generalizes to rectangles that need not be similar. The user may reorient the frustum by passing an OrientationMap to the constructor. If `with_equiangular_map` is true, then this coordinate map applies a tangent function mapping to the logical ξ and η coordinates. We then refer to the generalized logical coordinates as Ξ and H. If `projective_scale_factor` is set to a quantity other than unity, then this coordinate map applies a rational function mapping to the logical ζ coordinate. This gen-

eralized logical coordinate is referred to as Z. If `auto_projective_scale_factor` is `true`, the user-specified `projective_scale_factor` is ignored and an appropriate value for `projective_scale_factor` is computed based on the values passed to `face_vertices`. See the page on redistributing gridpoints to see more detailed information on equiangular variables and projective scaling.

Coordinate Map and Jacobian

In terms of the `face_vertices` variables, we define the following auxiliary variables:

$$
\begin{aligned}
\Sigma^x &= \frac{1}{4}(x^{+\zeta}_{-\xi,-\eta} + x^{+\zeta}_{+\xi,+\eta} + x^{-\zeta}_{-\xi,-\eta} + x^{-\zeta}_{+\xi,+\eta}) \\
\Delta^x_\zeta &= \frac{1}{4}(x^{+\zeta}_{-\xi,-\eta} + x^{+\zeta}_{+\xi,+\eta} - x^{-\zeta}_{-\xi,-\eta} - x^{-\zeta}_{+\xi,+\eta}) \\
\Delta^x_\xi &= \frac{1}{4}(x^{+\zeta}_{+\xi,+\eta} - x^{+\zeta}_{-\xi,-\eta} + x^{-\zeta}_{+\xi,+\eta} - x^{-\zeta}_{-\xi,-\eta}) \\
\Delta^x_{\xi\zeta} &= \frac{1}{4}(x^{+\zeta}_{+\xi,+\eta} - x^{+\zeta}_{-\xi,-\eta} - x^{-\zeta}_{+\xi,+\eta} + x^{-\zeta}_{-\xi,-\eta}) \\
\Sigma^y &= \frac{1}{4}(y^{+\zeta}_{-\xi,-\eta} + y^{+\zeta}_{+\xi,+\eta} + y^{-\zeta}_{-\xi,-\eta} + y^{-\zeta}_{+\xi,+\eta}) \\
\Delta^y_\zeta &= \frac{1}{4}(y^{+\zeta}_{-\xi,-\eta} + y^{+\zeta}_{+\xi,+\eta} - y^{-\zeta}_{-\xi,-\eta} - y^{-\zeta}_{+\xi,+\eta}) \\
\Delta^y_\eta &= \frac{1}{4}(y^{+\zeta}_{+\xi,+\eta} - y^{+\zeta}_{-\xi,-\eta} + y^{-\zeta}_{+\xi,+\eta} - y^{-\zeta}_{-\xi,-\eta}) \\
\Delta^y_{\eta\zeta} &= \frac{1}{4}(y^{+\zeta}_{+\xi,+\eta} - y^{+\zeta}_{-\xi,-\eta} - y^{-\zeta}_{+\xi,+\eta} + y^{-\zeta}_{-\xi,-\eta}) \\
\Sigma^z &= \frac{z_1 + z_2}{2} \\
\Delta^z &= \frac{z_2 - z_1}{2}.
\end{aligned}
\tag{2.51}
$$

The full map is then given by

$$
\vec{x}(\xi,\eta,\zeta) = \begin{bmatrix} \Sigma^x + \Delta^x_\xi \Xi + (\Delta^x_\zeta + \Delta^x_{\xi\zeta}\Xi)\mathrm{Z} \\ \Sigma^y + \Delta^y_\eta \mathrm{H} + (\Delta^y_\zeta + \Delta^y_{\eta\zeta}\mathrm{H})\mathrm{Z} \\ \Sigma^z + \Delta^z \mathrm{Z} \end{bmatrix},
$$

with Jacobian

$$J = \begin{bmatrix} (\Delta_{\xi}^{x} + \Delta_{\xi\zeta}^{x}\mathrm{Z})\Xi' & 0 & (\Delta_{\zeta}^{x} + \Delta_{\xi\zeta}^{x}\Xi)\mathrm{Z}' \\ 0 & (\Delta_{\eta}^{y} + \Delta_{\eta\zeta}^{y}\mathrm{Z})\mathrm{H}' & (\Delta_{\zeta}^{y} + \Delta_{\eta\zeta}^{y}\mathrm{H})\mathrm{Z}' \\ 0 & 0 & \Delta^{z}\mathrm{Z}' \end{bmatrix}.$$

Suggested values for the projective scale factor

This section assumes familiarity with projective scaling as discussed on the page on redistributing gridpoints.

When constructing a Frustum map, it is not immediately obvious what value of w_δ to use in the projective map; here we present a choice of w_δ that will produce minimal grid distortion. We consider two cases: the first is the special case in which the two rectangular Frustum bases are related by a simple scale factor; the second is the general case.

As seen in Cervone's Cubes and Hypercubes Rotating [16], there is a special case in which the inverse projection of a trapezoid is not another trapezoid, but a rectangle where the bases are congruent. Most often one will want to use the special value of w_δ where this occurs. This value of w_δ corresponds to the projective transformation mapping a rectangular prism in an ambient 4D space with congruent faces at $w = 1$ and $w = w_\delta$ to the frustum in the plane $w = 1$:

$$w_\delta = \frac{L_1}{L_2}, \tag{2.52}$$

where L_1/L_2 is the ratio between any pair of corresponding side lengths of the z_1- and z_2-bases of the frustum.

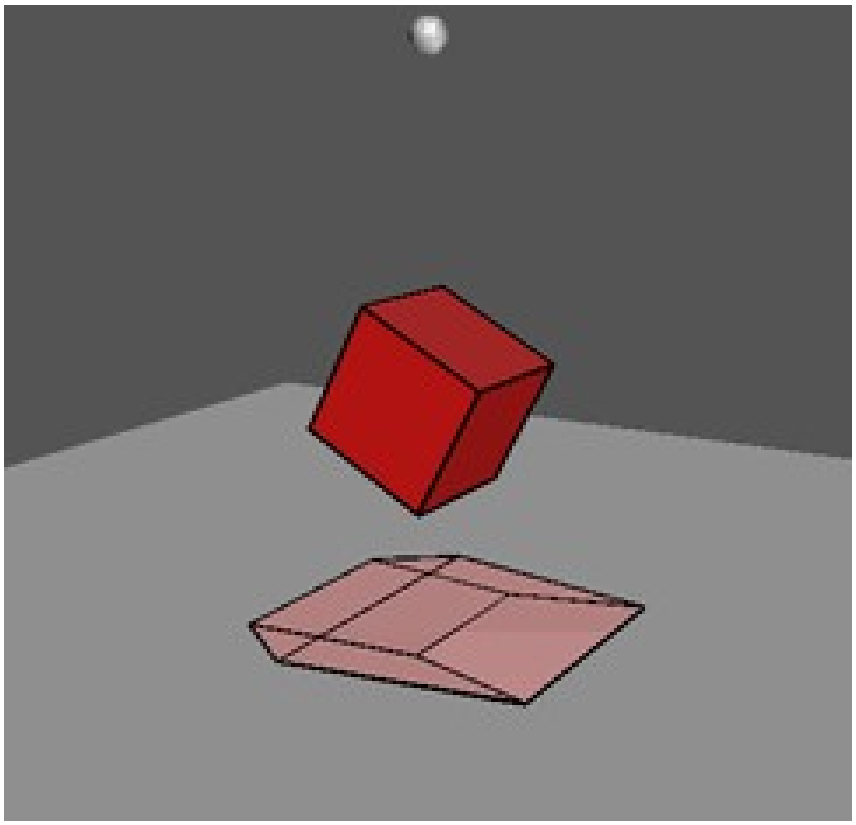

Figure 2.9: A frustum with rectangular bases.

For the general case one will want to use the value:

$$w_\delta = \frac{\sqrt{(x^{-\zeta}_{+\xi,+\eta} - x^{-\zeta}_{-\xi,+\eta})(y^{-\zeta}_{+\xi,+\eta} - y^{-\zeta}_{+\xi,-\eta})}}{\sqrt{(x^{+\zeta}_{+\xi,+\eta} - x^{+\zeta}_{-\xi,+\eta})(y^{+\zeta}_{+\xi,+\eta} - y^{+\zeta}_{+\xi,-\eta})}}. \tag{2.53}$$

This is the value for w_δ used by this CoordinateMap when `auto_projective_scale_factor` is `true`.

2.3.5 Equatorial Compression Map

This is a mapping from the sphere to itself that depends on a single parameter, the `aspect_ratio` α, which is the ratio of the horizontal length to the vertical height for a given point. This parameter name was chosen because points with $\tan\theta = 1$ get

mapped to points with $\tan\theta' = \alpha$[17]. In general, gridpoints located at an angle θ from the pole are mapped to a new angle θ' satisfying $\tan\theta' = \alpha\tan\theta$.

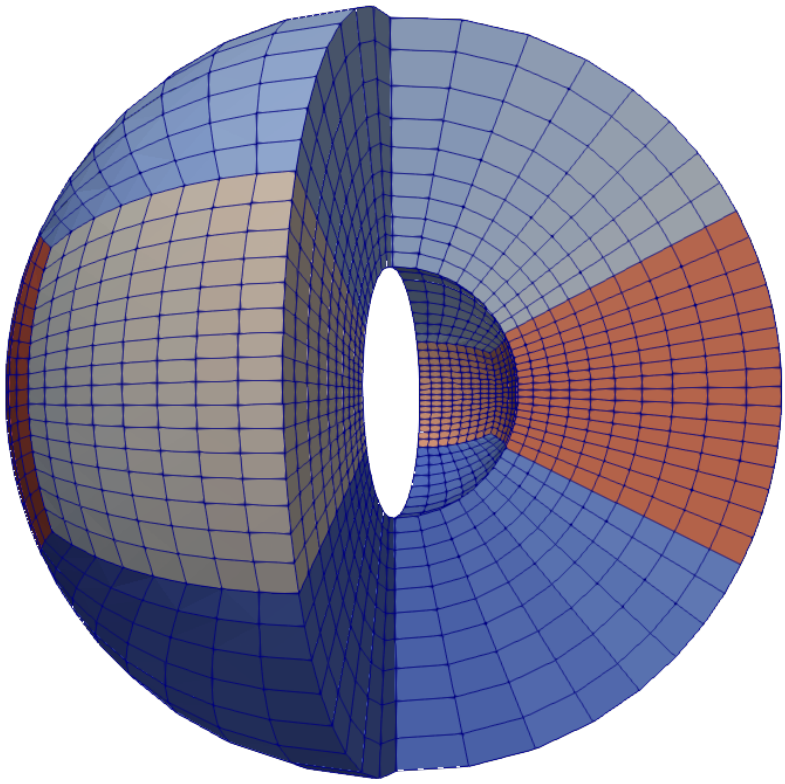

Figure 2.10: A Shell domain where the Equatorial Compression map has been applied. This map redistributes gridpoints from the north and south pols and moves them towards the equator. This is useful in accretion disk simulations where more resolution is desired at the equator.

For an `aspect_ratio` greater than one, the gridpoints are mapped towards the equator, leading to an equatorially compressed grid. For an `aspect_ratio` less than one, the gridpoints are mapped towards the poles. Note that the aspect ratio must be positive.

We define the auxiliary variables $r := \sqrt{x^2 + y^2 + z^2}$ and $\rho := \sqrt{x^2 + y^2 + \alpha^{-2}z^2}$. Then the map corresponding to this transformation in cartesian coordinates is given

by:

$$\vec{x}'(x,y,z) = \frac{r}{\rho}\begin{bmatrix} x \\ y \\ \alpha^{-1}z \end{bmatrix}. \tag{2.54}$$

2.3.6 Focally Lifted Maps

Consider the problem of creating invertible parameterized coordinate maps. These maps are to be used in the specification of a computational domain on which a PDE is solved.

Consider a parameterized surface $\vec{\sigma}$ whose points lie on the level set of some scalar function $\phi_\sigma = 0$. We define *focal lifting* as the projection of this surface with respect to some *focus* $\vec{x}_0$ and *lifting scale factor* Λ. The resulting map is then said to be a *focally lifted* map. These maps can be cast into the following form:

$$\vec{x} = \vec{x}_0 + \Lambda(\vec{\sigma} - \vec{x}_0). \tag{2.55}$$

Suppose that $\vec{\sigma}$ is parameterized by the *logical coordinates* ξ and η. Given that the surface map is invertible, the focally lifted map can be inverted by obtaining the value of $\Lambda(x,y,z)$ that satisfies the level set equation

$$\phi_\sigma(\frac{x-x_0}{\Lambda} + x_0, \frac{y-y_0}{\Lambda} + y_0, \frac{z-z_0}{\Lambda} + z_0) = 0. \tag{2.56}$$

ξ and η are then given by the surface inverse map to $\vec{\sigma}(\xi,\eta)$. Geometrically, the map can be inverted by following the ray from $\vec{x}_0$ to $\vec{x}$ in the desired volume and finding where this ray also intersects the surface $\vec{\sigma}$. While this motivates a procedure for numerically inverting the map, here we will only consider the case in which the inversion can be done analytically.

Focally Lifting the Cube

As an instructive example, we show how to obtain an analytically invertible map for any "ray body" (Minkowski's *Strahlkörper*). Any Strahlkörper may be constructed by focally lifting the six surface maps of the cube.

Suppose we have specified a Strahlkörper with surface $R(\theta, \phi)$ centered at the focus $\vec{x}_0$, where the angles θ and ϕ are defined with respect to this focus. The upper $+z$ map of the logical cube has the following form:

$$\vec{\sigma}(\xi, \eta) = \begin{bmatrix} \xi \\ \eta \\ 1 \end{bmatrix}. \tag{2.57}$$

We can lift this surface onto the desired Strahlkörper by multiplying by the factor $\Lambda(\xi, \eta) = R(\theta(\xi, \eta), \phi(\xi, \eta))/\sqrt{1 + \xi^2 + \eta^2}$. The focally lifted map then takes the following form:

$$\vec{x}(\xi, \eta) = \vec{x}_0 + \frac{R(\theta(\xi, \eta), \phi(\xi, \eta))}{\sqrt{1 + \xi^2 + \eta^2}} \begin{bmatrix} \xi \\ \eta \\ 1 \end{bmatrix}, \tag{2.58}$$

where $\theta(\xi, \eta) = \cos^{-1}(1/\sqrt{1 + \xi^2 + \eta^2})$ and $\phi(\xi, \eta) = \tan^{-1}(\eta/\xi)$. The other five surface maps are constructed similarly.

What remains is to find an analytic inverse. For surfaces $\vec{\sigma}(\xi, \eta)$ with constant normal vector $\hat{n}$, $\Lambda(x, y, z)$ is given by:

$$\Lambda(x, y, z) = \frac{(\vec{x} - \vec{x}_0) \cdot \hat{n}}{(\vec{\sigma} - \vec{x}_0) \cdot \hat{n}}. \tag{2.59}$$

$\vec{\sigma}$ is then given by:

$$\vec{\sigma} = \vec{x}_0 + \frac{(\vec{\sigma} - \vec{x}_0) \cdot \hat{n}}{(\vec{x} - \vec{x}_0) \cdot \hat{n}} (\vec{x} - \vec{x}_0), \tag{2.60}$$

from which the logical coordinates ξ and η follow immediately.

With two Strahlkörper surfaces $R_+(\theta, \phi)$ and $R_-(\theta, \phi)$, one can create a family of such surfaces $R(\theta, \phi, \zeta)$ parameterized by the logical coordinate ζ, where the ζ coordinate lines emanate radially outward from the focus $\vec{x}_0$. As long as $R_+(\theta, \phi)$ is strictly larger than $R_-(\theta, \phi)$, the volume map $\vec{x}(\xi, \eta, \zeta)$ can be inverted. In this case where upper $+z$ surface of the cube is lifted, the lifting factor is $\Lambda(\xi, \eta, \zeta) = R(\theta(\xi, \eta), \phi(\xi, \eta), \zeta)/\sqrt{1 + \xi^2 + \eta^2}$.

Jacobian

We provide the Jacobian in the case of a focally lifted volume, where the lifting factor varies with respect to all three logical coordinates. The Jacobian equations are:

$$\frac{\partial \vec{x}}{\partial \xi} = \frac{\partial \Lambda}{\partial \xi}(\vec{\sigma} - \vec{x}_0) + \Lambda \frac{\partial \vec{\sigma}}{\partial \xi} \tag{2.61}$$

$$\frac{\partial \vec{x}}{\partial \eta} = \frac{\partial \Lambda}{\partial \eta}(\vec{\sigma} - \vec{x}_0) + \Lambda \frac{\partial \vec{\sigma}}{\partial \eta} \tag{2.62}$$

$$\frac{\partial \vec{x}}{\partial \zeta} = \frac{\partial \Lambda}{\partial \zeta}(\vec{\sigma} - \vec{x}_0). \tag{2.63}$$

The determinant is then:

$$\det J = \Lambda^2 \det J_\sigma \frac{\partial \Lambda}{\partial \zeta}(\vec{\sigma} - \vec{x}_0) \cdot \hat{n}, \tag{2.64}$$

where $\det J_\sigma$ is the determinant of the Jacobian of the surface $\vec{\sigma}(\xi, \eta)$.

If we define the auxiliary variables:

$$\vec{\theta}_\xi := \frac{\partial \vec{\sigma}}{\partial \eta} \times (\vec{\sigma} - \vec{x}_0) \tag{2.65}$$

$$\vec{\theta}_\eta := (\vec{\sigma} - \vec{x}_0) \times \frac{\partial \vec{\sigma}}{\partial \xi}, \tag{2.66}$$

we can write the inverse Jacobian equations as:

$$\det J \frac{\partial \xi}{\partial \vec{x}} = \Lambda \frac{\partial \Lambda}{\partial \zeta} \vec{\theta}_\xi \tag{2.67}$$

$$\det J \frac{\partial \eta}{\partial \vec{x}} = \Lambda \frac{\partial \Lambda}{\partial \zeta} \vec{\theta}_\eta \tag{2.68}$$

$$\det J \frac{\partial \zeta}{\partial \vec{x}} = \Lambda^2 \det J_\sigma \hat{n} - \Lambda \frac{\partial \Lambda}{\partial \xi} \vec{\theta}_\xi - \Lambda \frac{\partial \Lambda}{\partial \eta} \vec{\theta}_\eta. \tag{2.69}$$

Metric

Let us define the variables:

$$\phi_\xi := \partial_\xi \vec{\sigma} \cdot (\vec{\sigma} - \vec{x}_0) \tag{2.70}$$

$$\phi_\eta := \partial_\eta \vec{\sigma} \cdot (\vec{\sigma} - \vec{x}_0) \tag{2.71}$$

$$h_{ij} := \partial_i \vec{\sigma} \cdot \partial_j \vec{\sigma}. \tag{2.72}$$

The metric g_{ij} for the volume then is given by:

$$g_{ij} = |\vec{\sigma} - \vec{x}_0|^2 (\partial_i \Lambda)(\partial_j \Lambda) + \Lambda^2 h_{ij} + \Lambda(\phi_i \partial_j \Lambda + \phi_j \partial_i \Lambda). \tag{2.73}$$

2.4 Orientation Methods

Each element in a SpECTRE domain is a hexahedral element mapped from the logical cube, whose coordinates are Cartesian in nature. In a domain with multiple elements, the logical directions are not necessarily aligned on the interfaces between two elements, as shown in Fig. 2.11. As certain operations (e.g. fluxes, limiting) communicate information across the boundaries of adjacent elements, there must be additional calculations that take into account the relative orientations of elements that neighbor each other. The collection of methods that are used to compute this connectivity information are referred to as Orientation methods in SpECTRE[18].

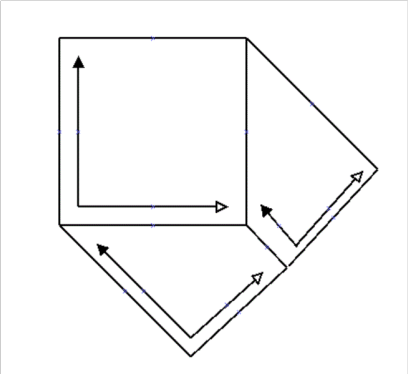

Figure 2.11: A domain in which it is not possible for the logical axes in each element to align with all of its neighbors' axes.

2.4.1 Local Corner Numbering

The orientation of the dim logical directions within each element determines an ordering of the 2^{dim} vertices of that element. This is called the local corner numbering scheme (Local CNS) with respect to that element. We give the ordering of the local corners for the case of a three-dimensional element in Fig. 2.12. All logical cubes in three dimensions share this numbering of their corners with respect to their logical coordinate axes.

2.4.2 Global Corner Numbering

To encode the relative orientations between elements in a domain, SpECTRE uses a global corner numbering scheme (global CNS), which is constructed by assigning a unique number to each of the vertices in a domain. Vertices that are shared between elements are assigned the same number; they are considered to be the same vertex. Fig. 2.13 gives an example of a global corner numbering.

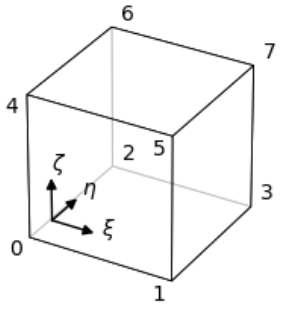

Figure 2.12: The standard local corner numbering of the logical cube in the case of three dimensions.

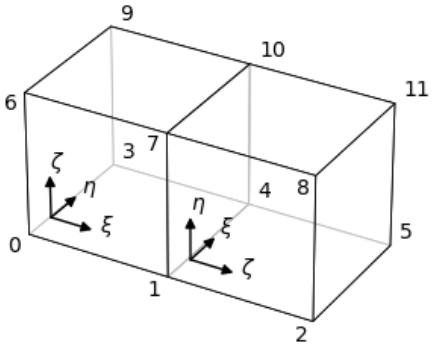

Figure 2.13: Each vertex of the two-block domain has been assigned a number. Although each block has eight corners, four are shared among them, so there are only twelve unique corners in this domain. Any numbering may be used in the global corner numbering, so long as the each distinct corner is given a single distinct corner number.

The local CNS is then used to encode the resulting relative orientations in a global corner numbering scheme (global CNS). The global CNS is an unordered list of ordered lists of numbered corners. Each entry of the outermost list corresponds to an element in the domain, and each of these entries is a list of the corners of that element. The ordering of the corners in each list is inherited from the local CNS; the orientation of the logical axes within each element determines the ordering of the global corner numbers in the list.

2.4.3 Deducing Orientations

In this subsection we will outline the algorithm used to deduce the relative orientations of the domain elements from the global CNS. Referring again to Fig. 2.13, here is one possible numbering that can be used:

```
Block1:  {0, 1, 3, 4, 6, 7, 9, 10}
Block2:  {1, 4, 7, 10, 2, 5, 8, 11}.
```

Each element has eight corners, and so each list has eight entries. While there are 16 total vertices among two cubes, in this domain they share a face. Four vertices are shared between them and only 12 numbers are needed to assign a unique global corner number to each vertex in the domain. The ordering of each list is determined by the local CNS. The first entries in each list correspond to the corners that are in the lowest $\{-\xi, -\eta, -\zeta\}$ octant of the cube, followed by those in the $\{+\xi, -\eta, -\zeta\}$ octant, and so on.

The global corner numbers that are shared between these two cubes are:

{1, 4, 7, 10} .

What then follows is determining the local corner number that corresponds to each of these shared global corner numbers with respect to each element's logical axes orientation. They are:

```
Block1 result:  {1, 3, 5, 7}
Block2 result:  {0, 1, 2, 3}
```

An intermediate step that is taken is to convert each corner number into its binary representation. Local corner numbers range from 0 to $2^{dim} - 1$. In the case of three dimensions they range from 0 to 111. Leading zeros are added such that each number has the same number of digits in the binary representation:

```
Corner 0:  000
Corner 1:  001
Corner 2:  010
Corner 3:  011
Corner 4:  100
Corner 5:  101
Corner 6:  110
Corner 7:  111
```

From here we can use the binary representation to read off the location of the corner: 0 and 1 indicate lower and upper in the corresponding axis (ζ, η, ξ). Note that the

ordering has been reversed so that the rightmost column corresponds to the ξ position and the leftmost column to the ζ position. Returning to the example at hand, we have:

```
Block1 result:  {001,011,101,111}
Block2 result:  {000,001,010,011}
```

As these corners are the corners of the shared face, all corners must lie on the same side of one axis, the axis that is perpendicular to the shared face. The direction in which the shared face lies can then be easily read off:

```
Block1:  Upper xi (All Block1 corners have a 1 in the third position)
Block2:  Lower zeta (All Block2 corners have a 0 in the first position)
```

In this manner the logical axes that correspond to the shared face are deduced between all pairs of neighboring elements in a domain, saving the user the work of having to manually specify the relative orientations between each element. This is most convenient in our larger domains in which we have dozens of elements, such as the binary compact object domain. In addition to encoding the relative orientations between shared blocks, we can also manually assign additional faces to be shared, which enables us to construct and use domains with more complicated topologies in our calculations.

2.4.4 Periodic Boundary Conditions

The corner numbering scheme that is used to determine the relative orientations between adjacent elements in a domain can also be used to manually identify the boundaries of non-adjacent elements. It is in this way that periodic boundary conditions are established in a domain. The vertices of the faces that are to be identified have different corner numbers in the global CNS. These corners, which encode the orientation of the logical axes, are then provided to an algorithm that determines the proper neighbor relationship the two faces should have.

2.4.5 Nontrivial Topologies

While SpECTRE is a code that is written with the primary purpose of doing binary black hole simulations in an asymptotically flat space time in mind, the algorithms outlined above allow the user to be more flexible in their choice of topology. As a simple example, the corner algorithm that is used to identify different faces of different elements with one another is sensitive to the orientation of the face: the ordering of the corners encodes the face's orientation. This allows the user to identify faces such that physical quantities that enter one of the faces leave the other face with a different orientation. In Fig. 2.14 we see how a particular identification of two of the faces of a two-dimensional rectangular domain results in a domain that has a Mobius strip topology. More exotic topologies can be constructed by identifying different sides of the rectangle with different orientations. For example, Fig. 2.15 shows that along with the standard choice of periodic boundary conditions, which results in a cylinder or torus topology, other identifications allow us to perform simulations on Klein bottle-like or projective plane-like surfaces.

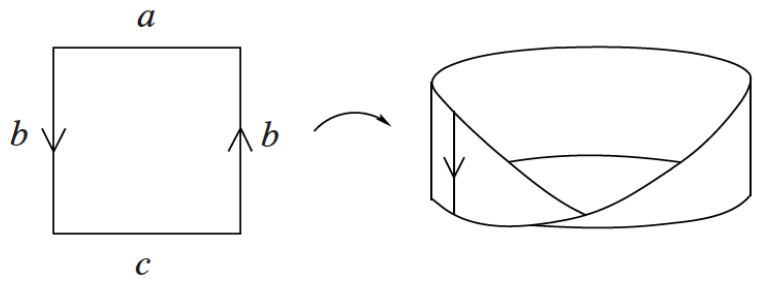

Figure 2.14: A square with two of the sides identified with opposite orientations has the topology of a Mobius strip; vector quantities that leave the domain from one face enter the domain from opposite face with the opposite orientation.

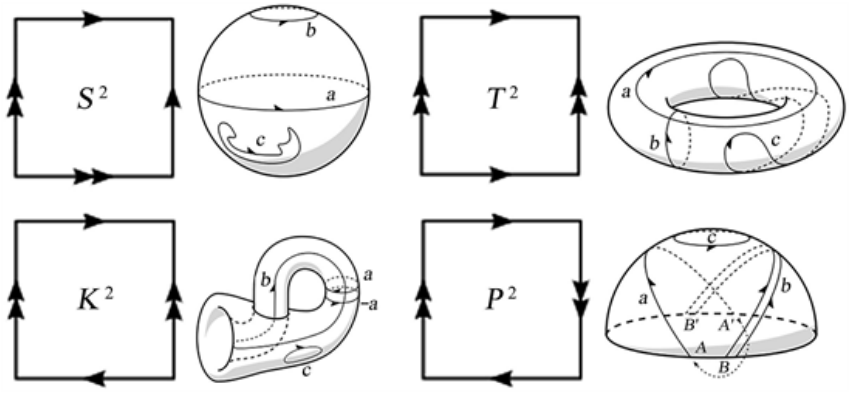

Figure 2.15: Different choices for which faces to identify, and with which orientation, result in multiple different topologies: the sphere S^2, the torus T^2, the Klein bottle K^2, and the projective plane P^2. The closed curves a, b, and c serve to illustrate the topology of the domain. Points A and A', and B and B', are identified.

The techniques that allow us to construct domains with these topologies for our two-dimensional simulations easily generalize to higher spatial dimensions [19]. In practice, we use multiple elements to construct a domain with a non-trivial topology and geometry, as the target geometry is still partitioned into hexahedra by these elements. In the case of a domain which has an $S^2 \times I$ topology, as seen in Fig. 2.16, we use the fact that the surface of an S^2 is partitioned into six equivalent regions when the edges of a cube that is concentric with the sphere are projected onto the spherical surface. This cube is then unfolded into a net, which determines the boundaries that

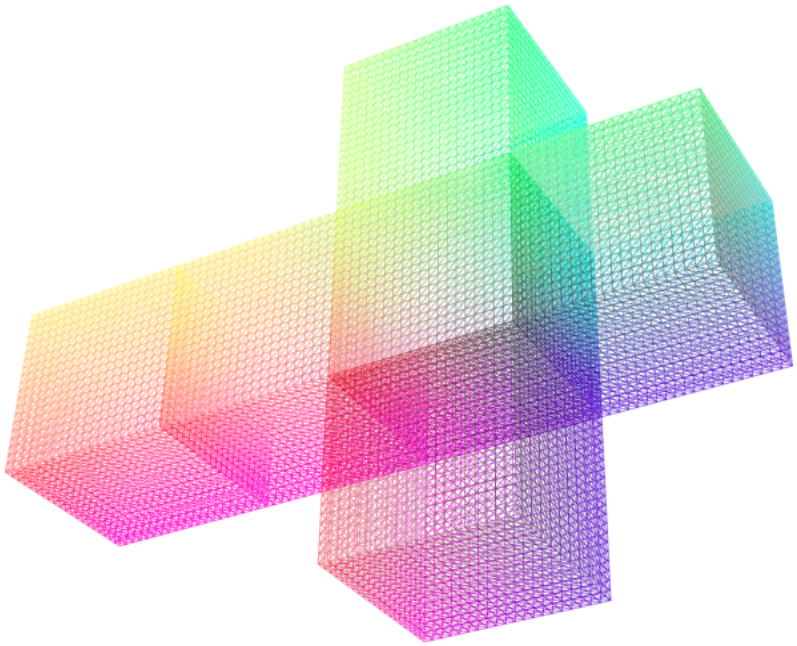

Figure 2.16: A net for the cube (which has an S^2 topology) that has been extruded to produce a domain that has a $S^2 \times I$ topology, once the corresponding faces of the cubes in the net have been identified.

are to be identified with one another. This net is then extruded into a third dimension. The faces to be identified stay the same, but the resulting domain now partions the $S^2 \times I$ domain into six equivalent regions.

With these methods it is possible to investigate spacetimes such as the Einstein closed universe [20].

2.4.6 Domains

The physical domain, the region of space in which the fields of the simulation are evolved, is decomposed into multiple hexahedral elements, each of which is equipped with a coordinate map that maps the element to the logical cube. The relative orienta-

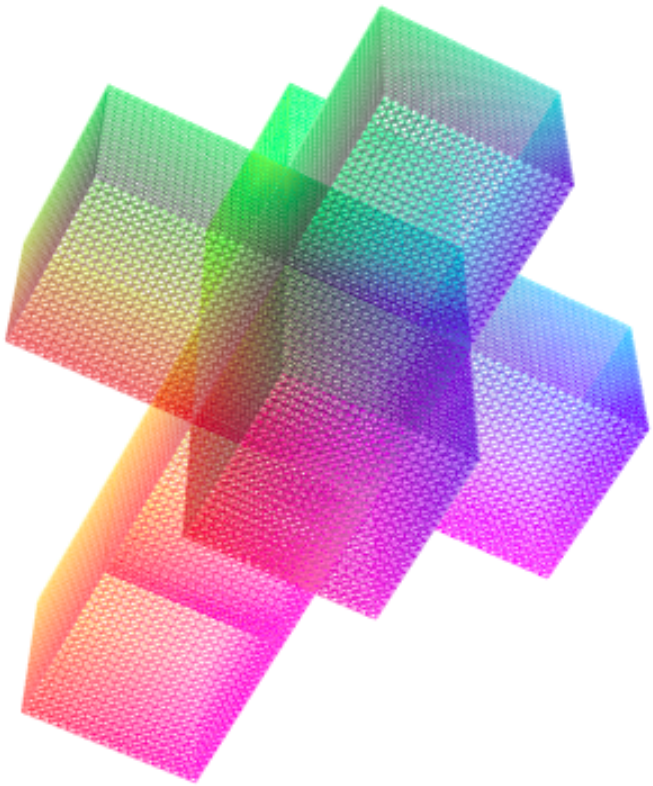

Figure 2.17: A net for the tesseract, which has an S^3 topology, once the corresponding faces of the cubes in the net have been identified.

tions of the logical axes relative to one another in these elements are computed, which allows for the proper communication of fluxes across element boundaries. SpECTRE uses these coordinate maps and corner algorithms to construct its domains. In this section we discuss three often-used domains, the Shell domain, used for single black hole and accretion disk simulations, the Sphere domain, used for neutron star simulations, as well as the Binary Compact Object Domain, used for binary black hole simulations.

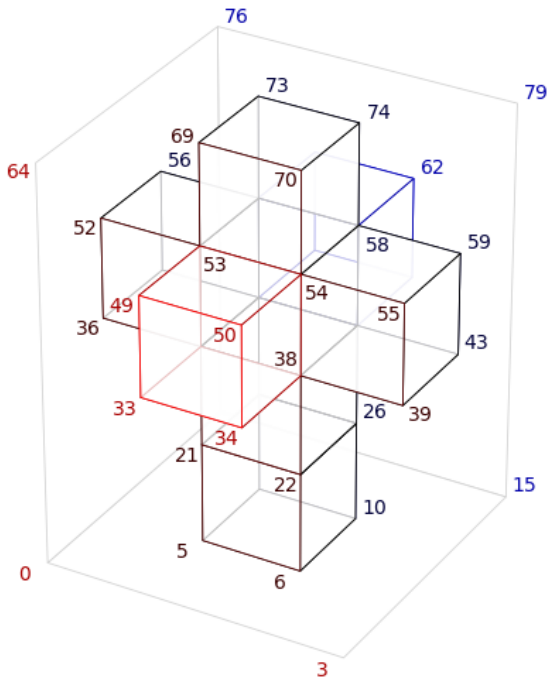

Figure 2.18: Different choices for which faces to identify, and with which orientation, result in multiple different topologies: the sphere S^2, the torus T^2, the Klein bottle K^2, and the projective plane P^2. The closed curves a, b, and c serve to illustrate the topology of the domain. Points A and A', and B and B', are identified.

Sphere and Shell Domains

The Shell domain (as seen in Fig. 2.19) is the primary domain used for single black hole simulations. Its defining feature is the excised region in the center, which is needed to remove the singularity from the spacetime that is being evolved. The spacetime that lies outside the singularity, but within the apparent horizon of the black hole, does not need to be evolved since all fields in this region will have their content fall into the black hole. The associated fluxes of these fields are only ingoing, and so there is no need to provide a boundary condition for the excised region.

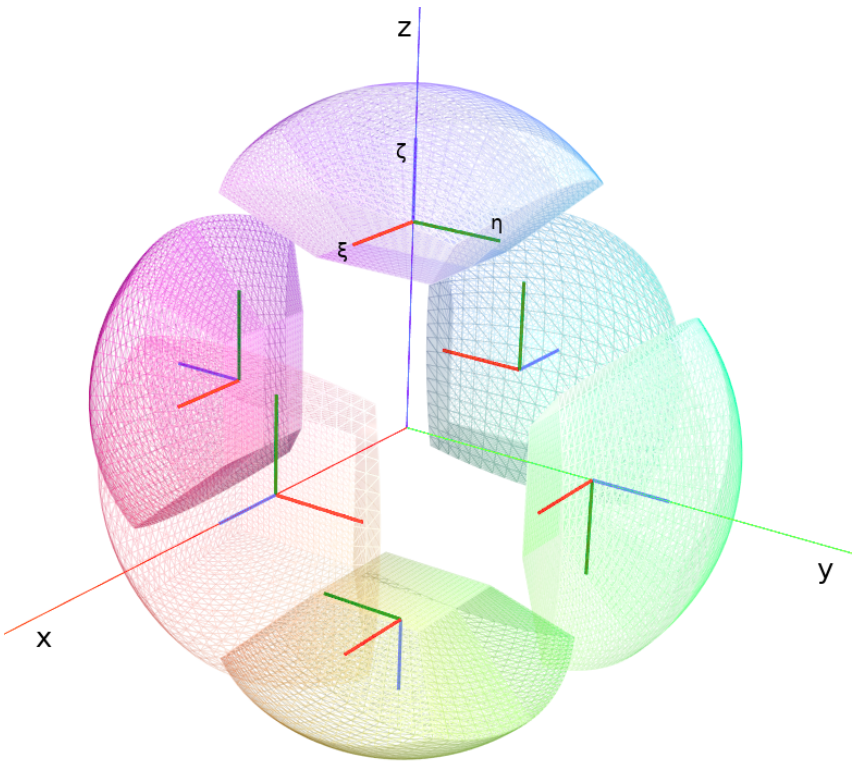

Figure 2.19: An exploded view of the Sphere domain, where the orientation of the logical axes within each element can be seen. The axes ξ, η, and ζ are colored in red, green, and blue.

Binary Compact Object Domain

The Binary Compact Object domain (as seen in Fig. 2.20) is the domain used when the interaction between two compact objects is being studied in SpECTRE[21]. Because of the hexahedral constraint on the element shapes, this domain is different from the one originally used in SpEC[22]. The domain consists of five layers of elements, referred to as *blocks* in SpECTRE:

- 0: (optionally) The block at the center of each compact object, if not excised. If present (as for a neutron star), this block is a cube. If excised, the hole left by its

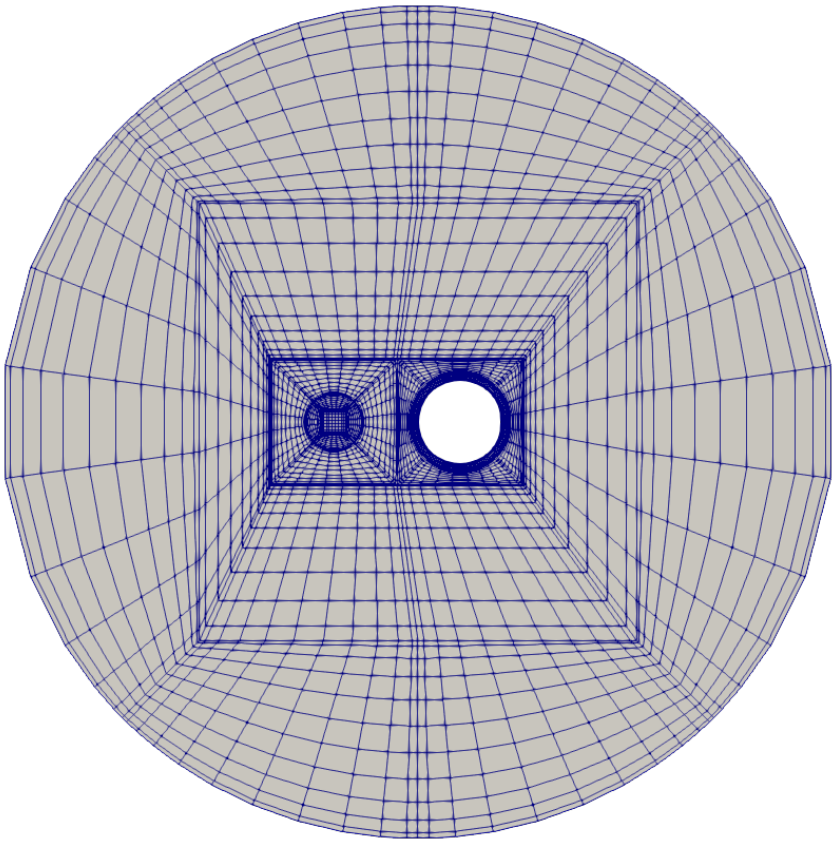

Figure 2.20: A slice of the Binary Compact Object domain, set up for a neutron star and black hole binary.

absence is spherical.

- 1: The blocks that resolve each individual compact object. This layer has a spherical outer boundary. If the corresponding layer-0 block exists, then the layer is a cube-to-sphere transition. If the layer-0 block is excised, then the layer is a spherical shell.
- 2: The blocks that surround each object with a cube. Around each compact object, this layer transitions from a sphere to a cube.
- 3: The blocks that surround each cube with a half-cube. At this layer, the two compact objects are enclosed in a single cube-shaped grid.
- 4: The 10 blocks that form the first outer shell. This layer transitions back to

spherical. The gridpoints are distributed linearly with respect to radius.

- 5: The 10 blocks that form a second outer shell. This layer is spherical, so a logarithmic map can optionally be used in this layer. This allows the domain to extend to large radial distances from the compact objects. This layer can be h-refined radially, creating a layer of multiple concentric spherical shells.

2.5 Conclusion

SpECTRE is primarily a code that employs the discontinuous Galerkin method to solve for the evolution of fields described by PDEs. The DG method is applied using a domain that has been partitioned into hexahedral elements, each equipped with coordinate maps and information on the relative orientation of neighboring elements, including periodic boundary information. The methods for establishing the mapping and connectivity for many possible domains used in SpECTRE have been described.

CHAPTER 3

MODELING THE MERGER IN BEYOND-GR WAVEFORMS

The parameterized post-Einsteinian framework incorporates beyond-GR effects into inspiral waveform models. We extend the existing model into the merger-ringdown regime. The modification introduced here adds a single degree of freedom that corresponds to a change in the binary coalescence time. Other merger properties remain as predicted by GR. We discuss parameter estimation with this model, and how it can be used to extract information from beyond-GR waveforms.

3.1 Introduction

For over two hundred years Newton's theory of gravity stood without equal as an accurate description of gravity. For the last hundred years, general relativity has superseded Newtonian gravity in predictive power. However, there is good reason to believe that general relativity (GR) is not the ultimate theory of gravity. In particular, many theorists believe that in the low-energy limit of some future quantum theory of gravity, there will be modifications that may be detectable on classical length scales [23, 24, 5].

GR reduces to Newtonian gravity in the appropriate limit, but it is not merely a correction term that is added on top of Newtonian predictions. Full GR is only obtained by demanding one's model of gravity adhere to new principles not present in Newtonian gravity, often referred to as the pillars of GR[23]. As a result, GR predicts additional phenomena that are entirely absent in the Newtonian theory, such as black holes and gravitational waves(GWs). Likewise, we expect that the theory of gravity to

replace GR will be founded on new principles and similarly reveal new phenomena not present in GR. It is possible that evidence of beyond-GR phenomena will make their first observable appearance as small deviations from GR in these GWs[24].

The detection of GW events such as GW150914 [5] has provided direct evidence that these new phenomena predicted by GR are present in our universe and that GR is an accurate description of gravity, even in the strong-field regime. These detections are made possible by searching for signals in the data of GW detectors such as LIGO using our knowledge of what we already expect these waveforms to look like in GR. The accurate construction of these model waveforms, used as matched-filter templates, is being improved upon as the sensitivity of the GW detectors improves.

For the process of matched-filtering to work however, the signals in GW data must be sufficiently similar to the constructed templates. By limiting oneself to only using GR to generate templates then, it can become impossible to recover a waveform that deviates from GR. Of course, it is in principle possible that a binary coalescence with certain parameters in a beyond-GR theory may be closely mimicked by a coalescence in GR with slightly different parameters [25].

The choice of using GR in the construction of waveform templates thus limits our ability to detect deviations from GR. Assuming GR in binaries where GR may be violated may cause us to ascribe incorrect properties to these binaries, and this will lead us to draw incorrect conclusions about the astrophysical population these binaries come from.[23]

There exist alternative theories of gravity beyond GR such as dynamical Chern-Simons gravity and Einstein dilaton Gauss Bonnet where there has been partial progress in producing GW waveforms[26]. Even if it were possible to produce wave-

forms from these beyond-GR theories with the full technology that we have for GR waveforms, it would still be computationally prohibitive to test GW data against each beyond-GR theory individually. It might also be the case that some yet-unknown beyond-GR theory fits the data even better than any of the ones being used in the parameter estimation.

Yunes and Pretorius have introduced a framework they refer to as the *parameterized post-Einsteinian*(ppE) formalism[27] for modifying waveforms such that neither GR nor any other particular beyond-GR theory is assumed, so long as the beyond-GR theory is smoothly connected to GR. Although it is not yet possible to perform full numerical simulations of mergers in all beyond-GR theories, it is possible in many to calculate the leading post-Newtonian(PN) order corrections to the waveform.[28] This correction is then incorporated via a modification of the corresponding waveform in GR. This allows for the searching of evidence for beyond-GR theories using GW data in a model-independent manner.

A limitation of Yunes and Pretorius' model that is addressed in this paper is that their model is derived under the quasicircular approximation. An alternative to the Yunes and Pretorius model that is explored in this paper is one where corrections in the inspiral regime are extended into the intermediate and merger-ringdown regimes, where an additional parameter shifts the merger time. The Yunes and Pretorius model only parametrizes deviations that occur in the inspiral regime, which are obtained by assuming a quasicircular inspiral. While this leads to leading PN-order corrections to the GR waveform in the inspiral regime, the approximation breaks down before the merger is reached. This is relevant to current efforts in GW detection in the LIGO band, since a significant portion of the signal-to-noise-ratio(SNR) is in the post-inspiral waveform. Yunes and Pretorius' model does not extend into this regime and so cannot

capture deviations from GR that occur there. In this paper, we present a new extension to the ppE framework that allows for corrections to the GR waveform past the inspiral regime. The new extension decouples the merger portion of the waveform from the initial spiral assuming a minimal number of new parameters. The new extension is able to model changes to the gravitational wave where the change in the merger time is independent of the changes that occur in the inspiral regime.

This paper is organized as follows. In Sec. II, we discuss the existing gravitational waveform models used, in particular the IMRPhenomD approximant[29], which is the model that is extended in this paper. In Sec. III, we discuss the waveform models in the context of modelling beyond-GR behavior, and the various ways in which inspiral models can be extended up to merger. In Sec. IV, we discuss how the model is used and its usefulness for parameter estimation is explored. In Sec. V, we summarize the results and lay out possible directions in which this work can be extended.

3.2 GR Approximants

Deducing the properties of a detected GW from a compact binary coalescence requires the production of a candidate waveform, called a template, against which the strain data can be compared. In practice, parameter estimation requires the generation of millions of templates of differing parameters[30]. It is prohibitively expensive to run full numerical relativity(NR) calculations for each choice of candidate parameters. Depending on the degree of accuracy required, there are various alternatives. GR-based phenomenological waveform models are a computationally cheaper method used to more rapidly produce many candidate waveforms. The trade-off is that these GR approximants are calibrated such that they are only consistent with NR simulations in a

limited region of parameter space. Moreover, NR itself encounters limits to its accuracy that are comparable to LIGO's accuracy needs[26]. To that extent, such waveforms can only be said to be GR waveforms up to a certain degree of accuracy; they are only GR approximants.

Analytically, there also exists the post-Newtonian (PN) method, which gives an accurate approximation to the inspiral GW for large separations and slow velocities. As the loudest component of a GW is the h_{22} mode, it is currently sufficient to only use an approximant for the h_{22} mode; the other modes contribute a non-neligible but small amount of power[31]. While there are other approximants available and in the process of being developed that include higher-order modes, in this paper we will restrict ourselves to the h_{22} mode.

3.2.1 TaylorF2

For completeness, we reproduce here the TaylorF2 approximant to the $\tilde{h}_{22}$ mode of the GW. This approximant is written in the frequency domain as $\tilde{h}_{\rm GR}(f)$, where the tilde denotes that the quantity has been Fourier transformed into the frequency domain. The TaylorF2 approximant is obtained from a PN treatment that assumes large separations and nonrelativistic speeds. It is analytic with no free model parameters, meaning it exists independent of calibration to any NR waveforms. In the TaylorF2 approximant [32], the leading order amplitude and phase of $\tilde{h}_{\rm TF2}(f)$ are given by the following:

$$\tilde{h}_{\rm TF2}(f) = \sqrt{\frac{2\eta}{3\pi^{1/3}}} f^{-7/6} e^{i\phi_{\rm TF2}}, \tag{3.1}$$

$$\begin{aligned}\phi_{\rm TF2} &= 2\pi f t_c - \phi_c - \pi/4 \\ &\quad + \frac{3}{128\eta}(\pi M f)^{-5/3} \sum_{i=0}^{7} \phi_i (\pi M f)^{i/3}.\end{aligned} \tag{3.2}$$

The above equations give the frequency-domain waveform for a binary with component masses m_1 and m_2, with total mass $M = m_1 + m_2$ and symmetric mass ratio $\eta = m_1 m_2 / M^2$, that coalesces at a time t_c with a coalescence phase of ϕ_c. Here ϕ_i are the coefficients corresponding to the PN expansion, where each coefficient depends on intrinsic binary parameters. We refer the reader to Eq.(318) in [32] for the spin-independent ϕ_i. The TaylorF2 portion of IMRPhenomD is supplemented with additional spin-dependent corrections, which are given in [29].

3.2.2 IMRPhenomD

The waveform approximant to which we apply the ppE correction is the IMRPhenomD approximant described in [29]. This is a frequency-domain approximant to the $\tilde{h}_{22}(f)$ GW mode. The approximant is split into three frequency regimes, denoted the inspiral, intermediate, and merger-ringdown regimes. The inspiral regime extends from the low-frequency limit of the waveform up to $Mf = 0.018$, while the intermediate region extends from this point up to $f = 0.5 f_{\rm RD}$, where $f_{\rm RD}$ is the ringdown frequency of the final Kerr black hole resulting from the coalescence.

In frequency-domain approximants, it is common to factor the strain $\tilde{h}_{\rm GR}(f)$ into separate amplitude and phase components:

$$\tilde{h}(f) = \mathcal{A}(f) e^{i\phi(f)}. \tag{3.3}$$

In the IMRPhenomD approximant, both $\mathcal{A}(f)$ and $\phi(f)$ are given as piecewise functions, with each piece corresponding to a different frequency regime.

In the inspiral regime, the IMRPhenomD waveform is the same as that of the TaylorF2 approximant, including the terms corresponding to higher-order PN corrections

in both the phase and amplitude. The full TaylorF2 phase used by IMRPhenomD is given by (3.2).

In the intermediate regime, the IMRPhenomD phase is given by

$$\eta\phi_{\rm Int} = \beta_0 + \beta_1 f + \beta_2 \log(f) - \frac{\beta_3}{3} f^{-3}, \tag{3.4}$$

where β_0 and β_1 serve to ensure continuity and differentiability, and β_2 serves as a fitting coefficient used to reproduce NR waveforms to a desired tolerance.

In the merger-ringdown regime, the IMRPhenomD phase is given by

$$\eta\phi_{\rm MR} = \alpha_0 + \alpha_1 f - \alpha_2 f^{-1} + \frac{4}{3}\alpha_3 f^{3/4} + \alpha_4 \tan^{-1}\left(\frac{f - \alpha_5 f_{\rm RD}}{f_{\rm damp}}\right), \tag{3.5}$$

where α_0, and α_1 ensure continuity and differentiability of the phase across the two regimes. The remaining parameters α_2, α_3, α_4, α_5, $f_{\rm RD}$, and $f_{\rm damp}$ are determined via fits to NR simulations of GR mergers.

3.3 PPE Approximants

Introduced by Yunes and Pretorius, the parameterized post-Einsteinian (ppE) formalism provides a way to modify frequency-domain GR waveforms according to the leading PN order deviation predicted by a beyond-GR theory[27]. The ppE framework consists of four parameters, α, β, a, and b. The modification to the GR waveform is given by:

$$\tilde{h}_{\rm ppE}(f) = \tilde{h}_{\rm GR}(f)(1 + \alpha u^a) e^{i\beta u^b}. \tag{3.6}$$

The parameters α and β quantify the amplitude and phase deviation from $\tilde{h}_{\rm GR}$, while the parameters a and b are selected by the beyond-GR theory that is being con-

sidered. The quantity $u(f) = (\pi \mathcal{M} f)^{1/3}$ is proportional to the Keplerian velocity of the orbit, where $\mathcal{M} = (m_1 m_2)^{3/5}/(m_1 + m_2)^{1/5}$ is the chirp mass of the binary.

The additional terms that appear in $\tilde{h}_{\rm ppE}(f)$ corresponding to a and b can be seen as corrections of a PN order relative to those that appear in $\tilde{h}_{\rm GR}(f)$. The relative PN orders of the correction terms that appear for a choice of a and b are $a/2$ and $(b+5)/2$, respectively. If we look at Eq. (3.6), we can see that the exponent a appears in the term with coefficient α, which controls the deviation in the amplitude, while the exponent b appears in the term with coefficient β, which controls the deviation in the phase. As the matched filtering process is much more sensitive to changes in the phase than in the amplitude, in this paper we will ignore the effects of the amplitude term, setting α to zero.

In Table 3.1, we list a few examples of beyond-GR theories with their corresponding values of a and b.

3.3.1 Inspiral Correction

The ppE parameters α and β correspond to the leading-order PN corrections to GR predicted by the beyond-GR theory under consideration. The ppE corrections to higher order are unknown, so the ppE-corrected waveform can be expected to deviate from

Table 3.1: The values of a and b corresponding to each beyond-GR theory, along with the PN order of the phase correction.

	a	b	PN
dCS	4	-1	2
Einstein-Æther	0	-5	0
EdGB	-2	-7	-1

the true beyond-GR waveform at higher frequencies. Recently, numerical simulations have been successful in evolving binaries in some beyond-GR theories through merger.[26] These numerical waveforms can be used to extend the ppE model to higher frequencies. The β-ppE correction is applied in the inspiral regime, which extends up to $Mf = 0.018$ in the IMRPhenomD model.

3.3.2 Post-inspiral-β Corrections

Besides changes to the phasing that might occur in the inspiral because of beyond-GR effects, an additional modification that might occur is a change in the merger time caused by a change in the inspiral rate. This raises the question of how we might extend the simple ppE model beyond the inspiral regime while still preserving the physical plausibility of the model. We examine a progression of increasingly sophisticated models to see how this merger-time modification naturally arises out of extending the inspiral correction in a manner that preserves continuity and differentiability. The difference between each of these models is determined by the choice of the ppE phase correction, denoted as $\Delta\phi_{\rm ppE}$. The amplitude $\tilde{h}_{\rm GR}(f)$ is left unchanged in each case. The generic form of the ppE correction where the phase is modified is then given by:

$$\tilde{h}_{\rm ppE}(f) = \tilde{h}_{\rm GR}(f) e^{i\Delta\phi_{\rm ppE}(f)}. \tag{3.7}$$

We now consider various methods for handling the ppE phase correction beyond the inspiral regime.

Zero Correction

For completeness, we include the case here where we do not include a post-inspiral correction at all, and instead truncate the ppE waveform at a particular frequency $f_{\rm IM}$.

$$\tilde{h}^{\rm Trunc}_{\rm ppE}(f) = \begin{cases} \tilde{h}_{\rm GR}(f) e^{i\beta u^b}, & f < f_{\rm IM}, \\ 0, & f_{\rm IM} \leq f. \end{cases} \tag{3.8}$$

C^0 Correction

Although the IMRPhenomD model is constructed to be C^1 in its phase, we include the C^0 correction here to be able to make comparisons against a naive post-inspiral correction that is not physically motivated.

$$\Delta\phi^{\rm C0}_{\rm ppE}(f) = \begin{cases} \beta u^b, & f < f_{\rm IM}, \\ \beta u^b_{\rm IM}, & f_{\rm IM} \leq f. \end{cases} \tag{3.9}$$

As seen in Fig. 3.1, such a correction may not necessarily result in an obviously pathological waveform.

C^1 Correction

The C^1 correction is the first post-inspiral correction that is physically motivated.

$$\Delta\phi^{\rm C1}_{\rm ppE}(f) = \begin{cases} \beta u^b, & f < f_{\rm IM}, \\ \beta u^b_{\rm IM} + \beta \frac{b}{3}((u/u_{\rm IM})^3 - 1), & f_{\rm IM} \leq f. \end{cases} \tag{3.10}$$

As seen in Fig. 3.2, the additional post-inspiral term induces a shift in the merger time and phase that leaves the two waveforms identical in the merger after this shift, which

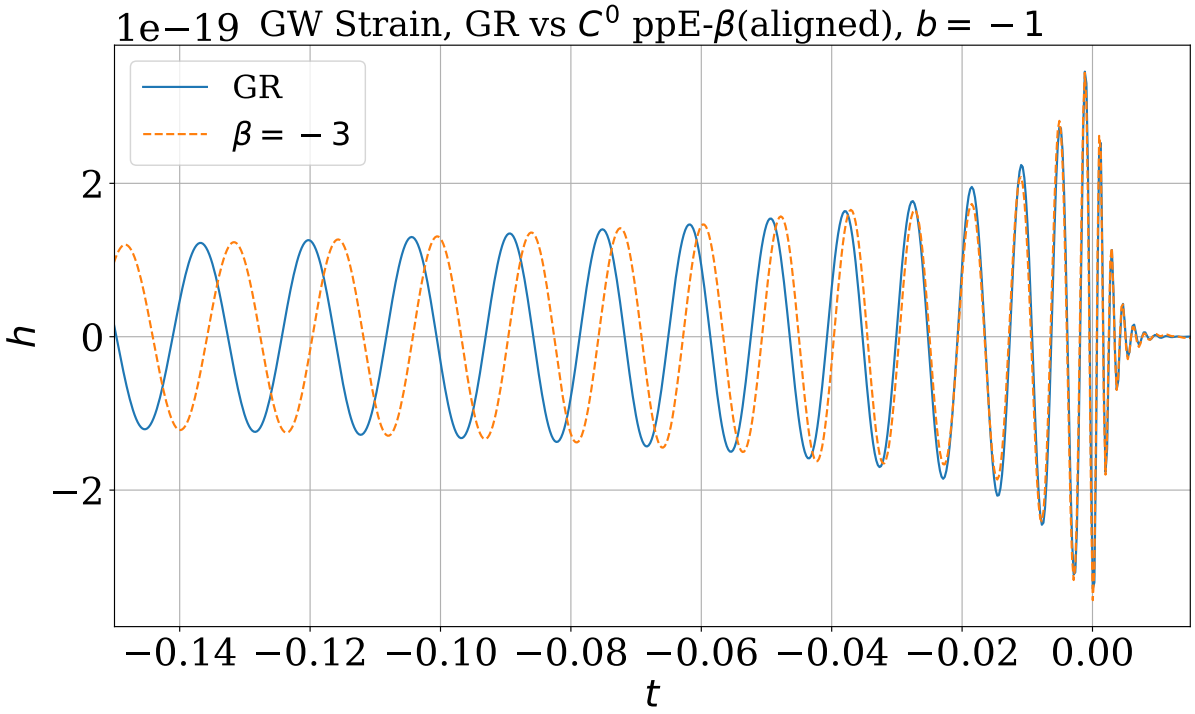

Figure 3.1: A GR waveform with its ppE-C^0 counterpart. Despite being less physically motivated than other ppE schemes, the correction still results in a waveform that is not obviously unphysical. The mergers have been aligned in time and in phase.

is linear in frequency, has been subtracted off. As the ppE-β correction is only applied in the inspiral regime, this scheme is a good candidate for extending the correction into the merger/ringdown regime with minimal assumptions.

C^∞ Correction

We also include the C^∞ correction for the sake of completeness:

$$\tilde{h}^{C\infty}_{\rm ppE}(f) = \tilde{h}_{\rm GR}(f) e^{i\beta u^b}. \tag{3.11}$$

For some values of b and β the extension of the inspiral correction into the merger regime leads to significant distortion of the waveform. We compute an upper bound

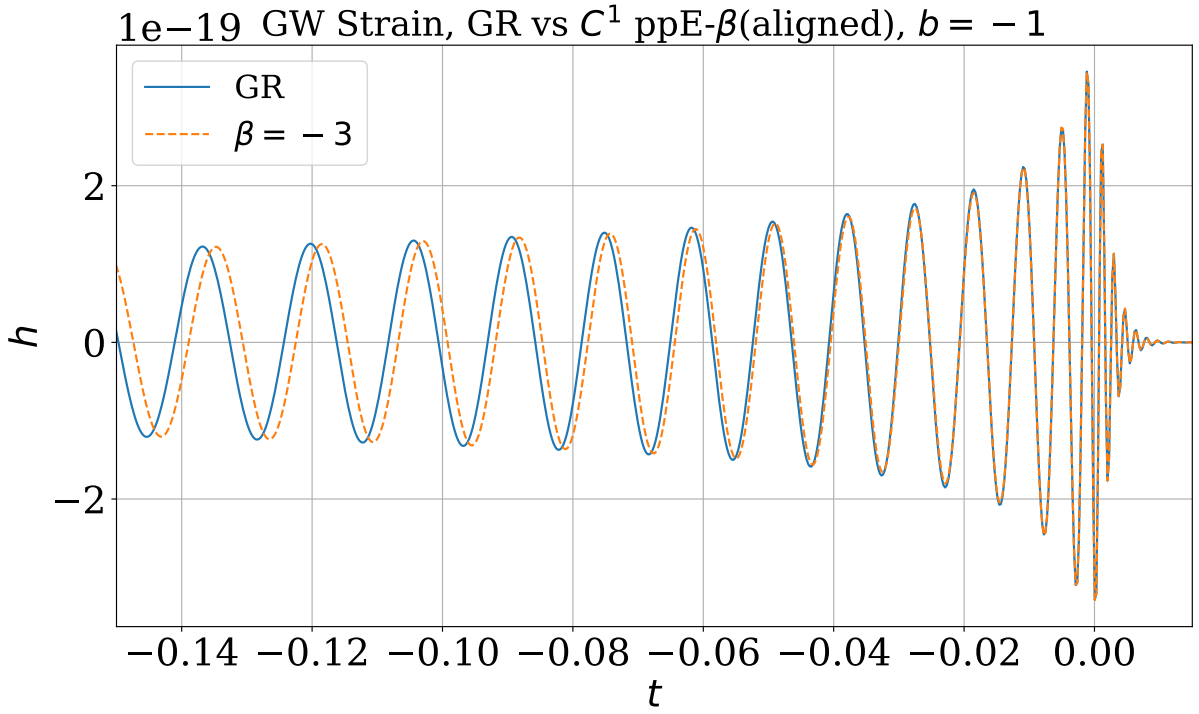

Figure 3.2: A GW in GR plotted against its ppE-β counterpart in the time domain. The ppE waveform has been shifted in phase and time such that both waveforms have the same t_c and ϕ_c. Aligning the waveforms in time renders the frequency domain waveforms identical after $Mf_{\rm IM} = 0.018$, which is reached 0.07s before merger. In the time domain, dephasing becomes apparent a few cycles before merger, but there is minimal amplitude disagreement between the two GWs.

on the value of β that is compatible with this type of correction. This motivates the need for a novel extension of the ppE correction into the intermediate and merger regimes.

3.3.3 Post-inspiral-$\beta\epsilon$ Correction

The β-ppE correction is extended into the intermediate and merger-ringdown regimes by demanding continuity and differentiability of the phase across frequency regimes. This is equivalent to changing the parameters β_0, β_1, α_0, and α_1 in the IMRPhenomD approximant (See equations (3.4) and (3.5)). Consequently, the intermediate and merger-ringdown portion of the β-ppE corrected waveform is unchanged with re-

spect to that of the original GR wavefrom from which it was constructed, albeit with a phase and time shift.

Merger Time Correction

These shifts are given by:

$$\phi_\beta = \left(1 - \frac{b}{3}\right) \beta u_{\rm IM}^b \tag{3.12}$$

$$t_\beta = \frac{-b}{3} \frac{\beta u_{\rm IM}^b}{2\pi f_{\rm IM}}. \tag{3.13}$$

This corresponds to the displacement of the peak GW amplitude in time and can be arranged such that at $t = t_c$, the GW reaches its peak amplitude in both the GR case as well as the ppE corrected case. The β-ppE correction used is the C^1 correction $\Delta\phi^{C1}_{\rm ppE}$ (see Eq. 3.10).

In Fig. 3.3, we show the effects of promoting the β in Eq. 3.10 which multiplies the u^3 term into an additional free parameter ϵ that controls the merger time.

IMRPhenomD Compatibility

The IMRPhenomD model uses a GR phase approximant that is C1 in frequency, so both the $\Delta\phi^{\rm C0}_{\rm ppE}$ and $\Delta\phi^{\rm C1}_{\rm ppE}$ post-inspiral phase corrections can be absorbed into a re-definition of the IMRPhenomD coefficients. This leaves the phase evolution $\Delta\phi'_{\rm ppE}(f)$ entirely expressible in terms of the IMRPhenomD parameters. This means that an IMRPhenomD waveform corresponding to a GR signal can be found such that the two frequency waveforms match exactly in the inspiral. In the C0 case, this corresponds to a change in the coalescence phase of the original GR waveform. In the C1 case, this corresponds to a change in both the coalescence phase and coalescence time of the original

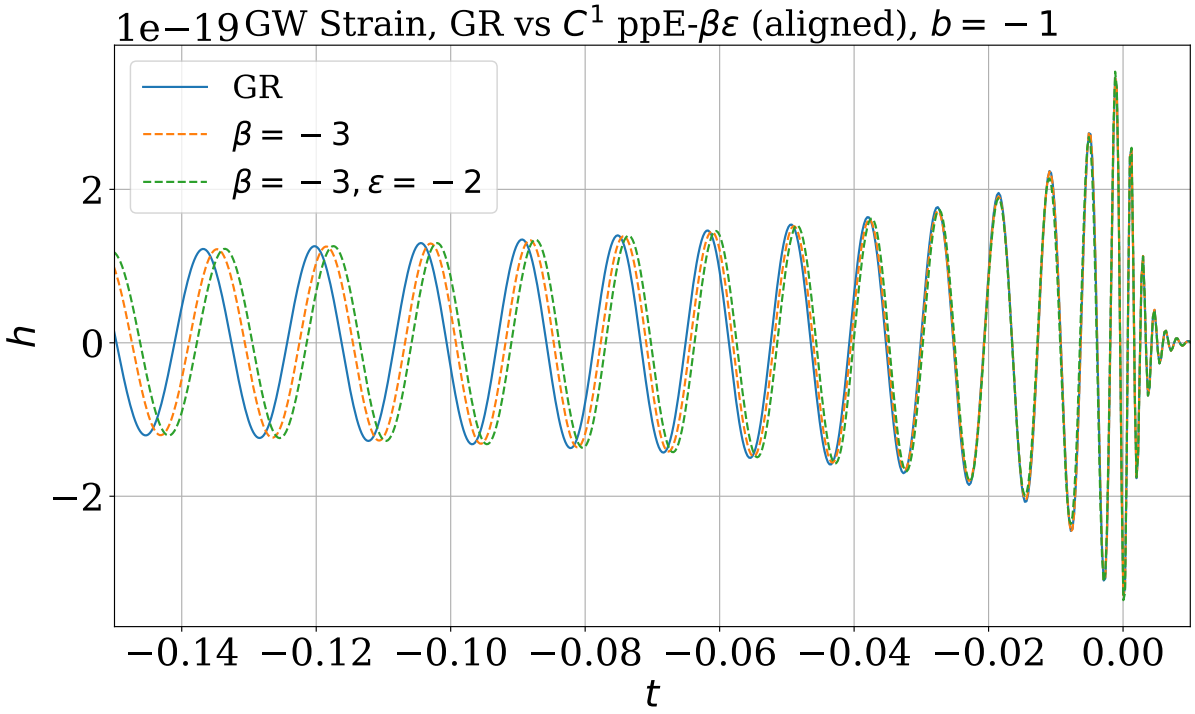

Figure 3.3: A GW in GR plotted against its ppE-β and ppE-ϵ counterpart in the time domain. The ppE waveforms have been shifted in phase and time such that all waveforms have the same t_c and ϕ_c. In the frequency domain, all waveforms are identical after $f = 0.5 f_{\rm RD}$. In the time domain, dephasing becomes apparent a few cycles before merger, and the dephasing is more significant for the the ppE-ϵ waveform. There is minimal amplitude disagreement between all GWs.

GR waveform. In Fig. 3.4 we show how this C^1 agreement between the IMRPhenomD model and the ppE correction scheme is reflected in the fact that the derivatives of the Fourier phases are identical in the merger/ringdown regime, barring a constant offset corresponding to the time shift incurred by the ppE modification.

Time-Shifting Property

Note that the time shift in the coalescence time incurred by extending the ppE-β correction into the merger regime in a C1 fashion is not a prediction of the original beyond-GR theory in the ppE-β framework. The ppE-β correction is calculated using an as-

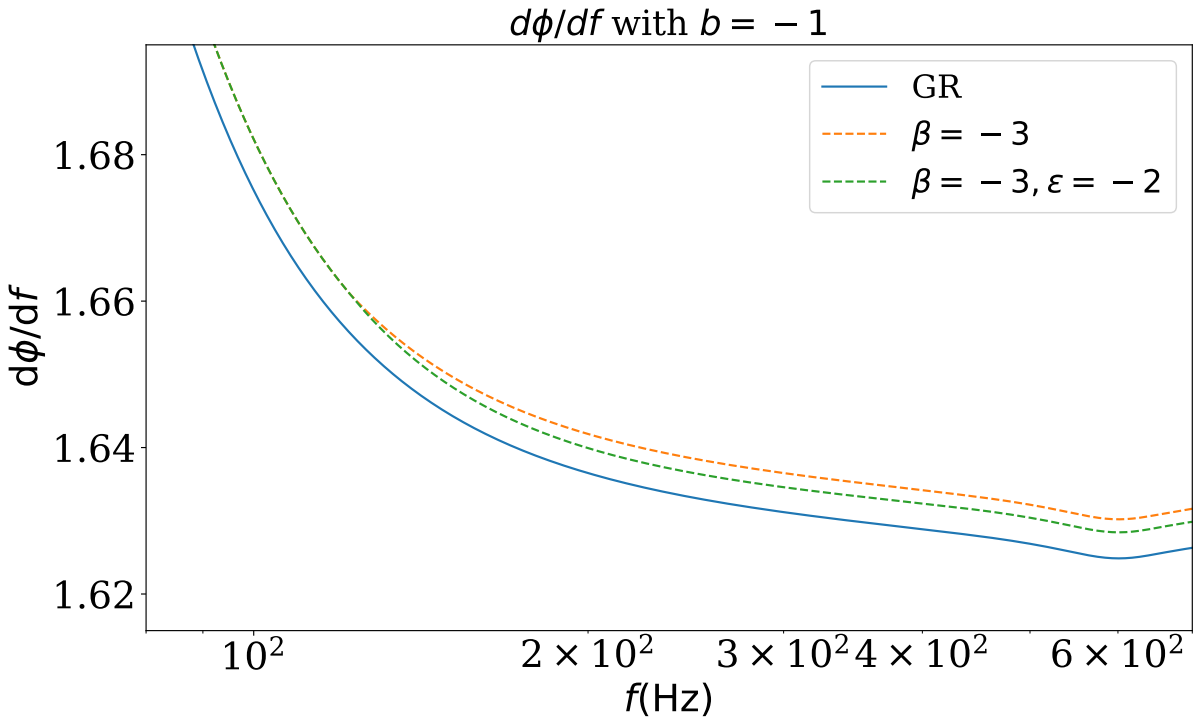

Figure 3.4: The derivative of the Fourier phase for both a GR waveform (blue), its ppE-β counterpart (orange), and its ppE-ϵ counterpart (green). The ppE-corrected waveforms are identical in the inspiral regime. The ppE-ϵ parameter controls the further deformation of the waveform beyond $Mf = 0.018$.

sumption of a quasicircular inspiral. One should not expect that the dynamics of a merger in which this assumption breaks down can be approximated in this way. This motivates us to extend the ppE-β correction by generalizing the time shift such that it is controlled by a new parameter ϵ (cf. Eq.(3.13)):

$$t_\epsilon = \frac{-b}{3} \frac{\epsilon u_{\rm IM}^b}{2\pi f_{\rm IM}}. \tag{3.14}$$

This new parameter ϵ then parameterizes the change in the merger time with respect to a GR merger with the same intrinsic parameters. Note that the time shift t_β in the ppE-β framework is determined by the C1 requirement imposed on the waveform across the frequency regimes. In the ppE-ϵ framework, the C1 requirement is still imposed; the requirment is satisfied by modifying the waveform in the intermediate

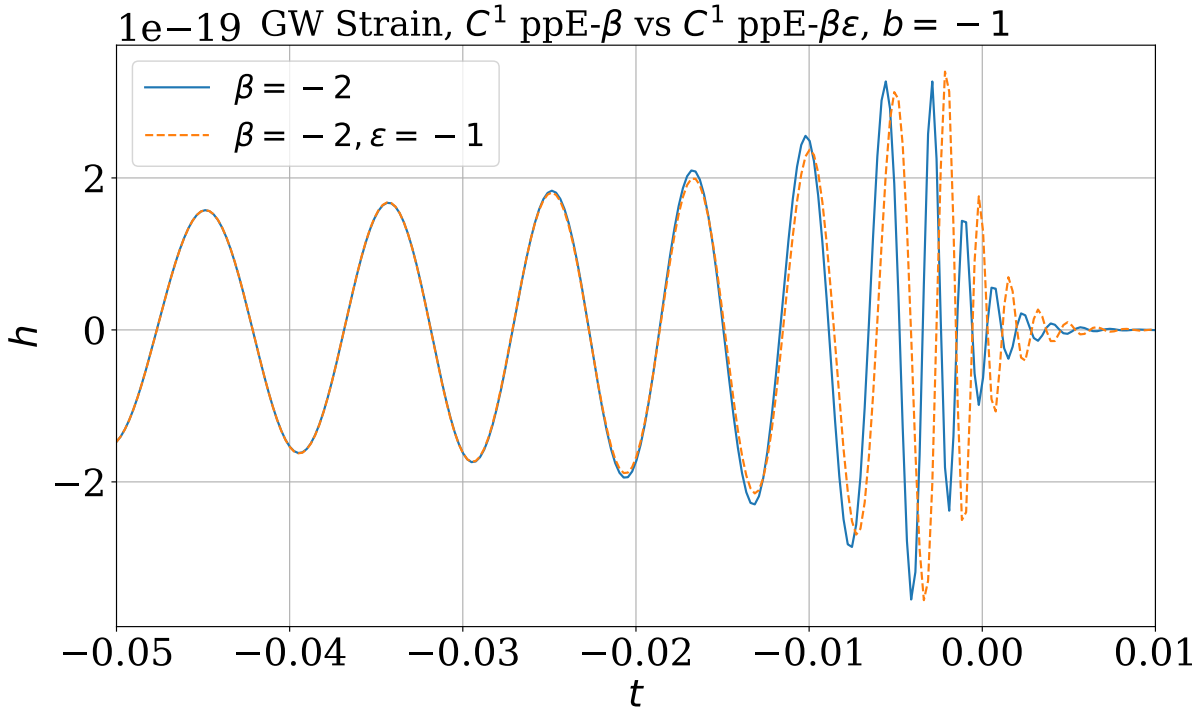

Figure 3.5: A ppE-β corrected waveform plotted against its ppE-$\beta\epsilon$ corrected counterpart in the time domain. The ppE waveforms have **not** been shifted in phase and time such that all waveforms have the same t_c and ϕ_c. The localized shifting of the merger portion of the ppE-$\beta\epsilon$ corrected waveform relative to the ppE-β corrected waveform can be clearly seen.

regime through changes in the parameters β_0, β_1, β_2, and β_3, which are now functions of ϵ. The phase change in the inspiral-merger regime is then given by:

$$\Delta\phi^{\epsilon}_{\rm ppE}(f) = \begin{cases} \beta u^b, & f < f_{\rm IM}, \\ \Delta\phi_{\rm Int}(f,\beta,\epsilon), & f_{\rm IM} \leq f < \frac{1}{2} f_{\rm RD}, \\ \beta u^b_{\rm IM} + \frac{b}{3}\epsilon u^b_{\rm IM}((u/u_{\rm IM})^3 - 1), & \frac{1}{2} f_{\rm RD} \leq f. \end{cases} \tag{3.15}$$

The form of $\Delta\phi_{\rm Int}(f,\beta,\epsilon)$ is determined by the coefficients β_0, β_1, β_2, and β_3 that

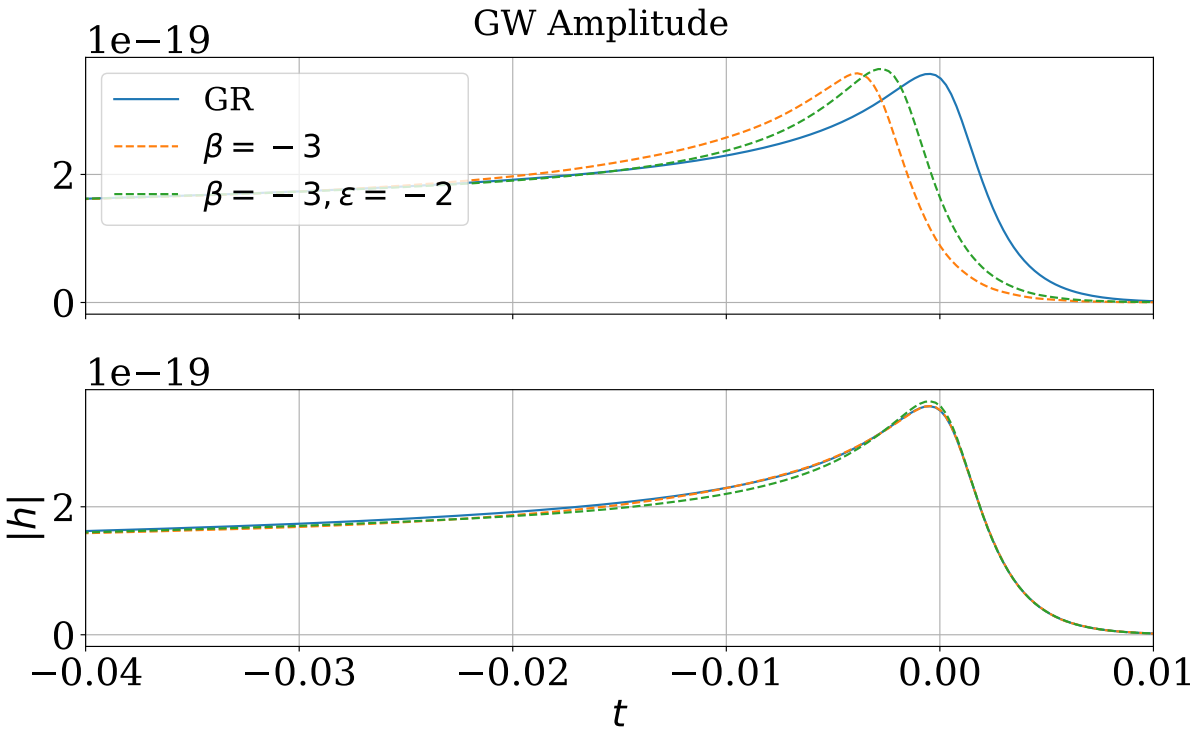

Figure 3.6: The GW strain amplitudes after applying various ppE corrections, with the mergers aligned in time in the bottom panel. While the ppE-ϵ is a pure phase correction in the frequency domain, this is not the case after transforming to the time domain. While the ppE-β corrected GW suffers from less distortion, neither produce a GW amplitude that is non-monotonic before t_c.

solve the following matrix equation:

$$\begin{bmatrix} \Delta\phi^{\epsilon}_{\rm ppE}(f_{\rm IM}) \\ \Delta\phi^{\epsilon\prime}_{\rm ppE}(f_{\rm IM}) \\ \Delta\phi^{\epsilon}_{\rm ppE}(f_{\rm RD}/2) \\ \Delta\phi^{\epsilon\prime}_{\rm ppE}(f_{\rm RD}/2) \end{bmatrix} = \begin{bmatrix} 1 & f_{\rm IM} & \log((f_{\rm IM}) & -\frac{1}{3}f_{\rm IM}^{-3} \\ 0 & 1 & 1/f_{\rm IM} & \frac{1}{9}f_{\rm IM}^{-4} \\ 1 & f_{\rm RD}/2 & \log(f_{\rm RD}/2) & -\frac{1}{3}(f_{\rm RD}/2)^{-3} \\ 0 & 1 & 2/f_{\rm RD} & \frac{1}{9}(f_{\rm RD}/2)^{-4} \end{bmatrix} \begin{bmatrix} \beta_0 \\ \beta_1 \\ \beta_2 \\ \beta_3 \end{bmatrix}. \tag{3.16}$$

While Eq. (3.15) gives the modification of the waveform, this is not the modification that is applied when performing parameter estimation. The presence of the factor that is linear in frequency in the ringdown regime causes the coalescence time to incur a shift after Fourier transforming to the time domain; this linear factor is subtracted off in order for the coalescence time t_c to remain unchanged for different choices of β and ϵ. Note that when a correction of non-zero β is applied to the inspiral regime in the $\beta\epsilon$ correction scheme, a corresponding correction of $\epsilon = \beta$ must also be applied to the rest of the waveform such that the resultant waveform is equivalent to a ppE-β corrected waveform satisfying the C1 continuity condition. For example, in Fig. 3.5, a choice of $\epsilon = \beta = -2$ would lead to the dotted orange curve lying on top of of the blue curve. A choice of $\epsilon \neq \beta$ leads to the merger portion of the waveform being displaced. As this leaves the rest of the waveform intact, it demonstrates how ϵ is a nearly independent parameter from β, which only affects the inspiral portion of the waveform, and thus can be measured separately. In Fig. 3.6 the GW strain amplitudes are plotted demonstrating that the monotonicity of the amplitude is preserved after the ϵ modification of the merger-ringdown portion of the waveform, indicating that the time-shifting property of the ϵ modification is a physical plausible one.

3.4 Parameter Estimation

In order to determine the characteristics of the two compact objects that generate a detected GW, one finds the model parameters for a template waveform that best corresponds to the data. For GR approximants there may be up to fifteen such parameters, which includes extrinsic parameters determining the sky location of the binary as well as intrinsic parameters corresponding to binaries that are physically distinct in their source frame. The ppE-$\beta\epsilon$ corrected waveforms have two additional parameters,

corresponding to beyond GR modifications in the inspiral and intermediate regimes. Constraints on these parameters can also be obtained using matched-filter parameter estimation, which allows us to begin examining the degree to which the current GW data deviates from GR, if at all.

3.4.1 Match

It may be the case that the GWs that observatories are detecting are beyond-GR in nature. That these observatories are still able to identify GW events in the data using GR templates tells us that the theory of gravity describing these GWs must not be too dissimilar from GR at these scales. To quantify the amount of mismatch between a GR waveform and a ppE-corrected waveform with non-zero β, we use the *match*, defined as follows:

$$\mathrm{match}(h, h_{\mathrm{ppE}}) = \max_{t_c,\phi_c} \Re \frac{\int df \hat{h}^*(f)\hat{h}_{\mathrm{ppE}}(f)e^{-2\pi i f t_c + i\phi_c}}{\sqrt{\int df \hat{h}^*(f)\hat{h}(f)}\sqrt{\int df \hat{h}^*_{\mathrm{ppE}}(f)\hat{h}_{\mathrm{ppE}}(f)}}. \quad (3.17)$$

where $\hat{h}(f)$ is the noise-weighted Fourier-domain waveform $\tilde{h}(f)/S_n(f)$, and $S_n(f)$ is the corresponding noise curve.

Using the ppE framework, we can produce waveforms that are distinguishable from GR. We then compare the similarity between the ppE modified waveform and the unmodified GR waveform using the match statistic between the two waveforms. This gives us a quantitative handle on how large a ppE correction we can make to the GR waveform.

3.4.2 Injection Recovery

To quantify the degree to which the beyond-GR parameters can be recovered from GW data, we carry out parameter estimation (PE) on simulated data consisting of waveforms embedded in noise. In general, this is done by choosing a waveform model to generate the data to be injected in the PE pipeline. We then choose a second waveform model (which can be the same as the first) to generate the templates with which the matched-filtering is performed.

To establish a baseline for how well parameters can currently be determined from GW data, we show the results of a parameter estimation run using IMRPhenomD templates on IMRPhenomD injections. This stands in for the case where we assume GR is a sufficiently accurate model of gravity for the purposes of our current GW data. Next, we want to explore what happens if we use GR-approximants for templates when the underlying signal is beyond-GR in nature. We represent this possibility by showing the results of a PE run using IMRPhenomD templates on ppE-corrected IMRPhenomD injections. The posteriors can then be compared against the GR-to-GR case where the templates match the underlying theory. We expect a slight broadening of the posteriors as the GR model becomes a poorer approximation to the beyond-GR injections. We then show the case of a PE run where a ppE-corrected template is used against a ppE-corrected injection. In this case we expect to recover the underlying parameters of the binary to a similar accuracy as in the GR-to-GR case. Finally we show the case of PE with a ppE template against a GR injection, to represent the case where the new ppE model is used before GW detectors have the sensitivity to capture beyond-GR effects in GW data.

To simulate the effects of accumulating a large amount of GW signals that are beyond-GR in origin, we conduct the PE runs in the zero-noise limit. While an in-

dividual event may have a small SNR, having multiple detectors in place allows us to combine the detector data to allow the signals to add constructively, increasing the overall SNR. The zero-noise limit occurs in the limit of having infinitely many detectors for a single event[33]. Although one may also consider combining signals from multiple events, this must be done carefully as beyond-GR effects may manifest differently in binaries that have different parameters from each other.

Choice of MCMC Parameters

The parameter estimation is done via a Markov Chain Monte Carlo (MCMC) algorithm within PyCBC Inference[6], in which trial waveforms are sampled from a parameter space and then compared against the simulated data. Using the likelihood, subsequent waveforms are sampled in a probabilistic fashion, resulting in a chain of samples. If done correctly, the resulting distribution of samples approximates the posterior distribution. One detail of MCMC is that the sampling process resembles a random walk, and the samples that make up the initial steps of the random walk may not be representative of the posterior distribution, because of being initialized in, or stepping into, a region that should be exponentially less populated. These samples are identified and eliminated in a procedure known as *burn-in*. There are multiple procedures for estimating when the chain has burned in; we use the `nacl` and `max_posterior` methods defined in PyCBC.

In our parameter estimation runs we use an extension of MCMC that makes use of what is known as *parallel tempering*. Parallel tempering initializes multiple chains that explore the parameter space according to the "temperature," which modifies the effect the likelihood has on the next iteration of the chain. This allows the chains to more efficiently explore the parameter space than could be done using only a single

temperature.

The particular MCMC settings that have been used are given in table 3.2.

Choice of Prior Parameters

In this section we discuss the effect the choice of prior has on the recovery of the parameters of a GR injection. At present, no measurable non-zero β-deviation from GR has been detected in GW data [34]. However, we can do better than to start with an arbitrarily wide uniform prior on β. From our match approximant, we can identify values of β for which the match would drop as low as 95%; we do not need to consider values of β that would cause a higher mismatch as such deviations from GR would have been identified already [35]. For a fixed mismatch, we can also examine what effect the mass has on the value of β needed to produce such a mismatch. At higher total masses, the lower frequency portions of the waveform, which are identically GR in the ppE-β framework, dominate the SNR and a higher value for β is needed for mismatches arising from the modified inspiral to be significant. This effect become more pronounced as one changes the value of the ppE parameter b in the exponent of the phase change term. In this paper we are examining posteriors in β and ϵ for only a single value of b, so even though the masses are not held fixed, a fixed prior over β and ϵ is sufficient for our purposes.

Table 3.2: The MCMC parameters used to perform the parameter estimation examined in this paper.

N_{walkers}	N_{temps}	$N^{\text{Eff.}}_{\text{samples}}$	$N^{\text{Max}}_{\text{perChain}}$	Burn-in Test
3000	4	3000	3000	`nacl | max_posterior`

The particular prior choices that have been used are given in table 3.3.

Choice of Injection Parameters

In Table 3.4, we list the different injections over which we have done parameter estimation runs. These values are the same as those used in the parameter estimation example in the PyCBC documentation. The masses probed are those most most likely to be found by detectors with noise curves similar to LIGO[36]. In this paper we only consider equal-mass injections, but the parameter estimation does not assume this.

GR Injection, GR Approximant

In order to have a baseline for how well we can expect the beyond-GR parameters to be recovered, we must first examine the degree to which the ordinary GR parameters can be recovered using the unmodified IMRPhenomD approximant. In Fig. 3.7 we show the posterior recovered for two chosen parameters, the coalescence time t_c and the chirp mass $\mathcal{M}$. In Fig. 3.8, we show the posterior distribution recovered for the chirp mass for each GR injection. Using the widths of the initial posteriors as a baseline, we repeat the parameter estimation on the GR injection using the ppE-β approximant. If using the β-modified ppE approximant causes the spreads to widen too broadly, then

Table 3.3: The parameters of the priors used to perform the parameter estimation examined in this paper.

param.	t_c	M_1	M_2	ϕ_c	β	ϵ
Dist.	Unif.	Unif.	Unif.	Unif. Angle	Unif.	Unif.
Min	1126259462.32	10	10	n/a	-20	-20
Max	1126259462.52	80	80	n/a	20	20

parameter estimation may not be too useful anymore.

GR Injection, ppE Approximant

We now examine the results of parameter estimation runs where the injection is a GR waveform, but the template used to recover parameters is of a ppE nature. In this case, the parameter estimation will attempt to recover values of β and ϵ in addition to the standard GR parameters. Since the underlying signal is GR in nature, we expect the recovered values of β and ϵ to be consistent with zero. As we only vary the injections over the mass of the system, there are only five injections created. In Fig. 3.9, we show the posteriors recovered for four chosen parameters, the coalescence time t_c and the chirp mass $\mathcal{M}$ as before, and now the ppE parameters β and ϵ. We note that the peaks of the posteriors for t_c and $\mathcal{M}$ are offset slightly from the posteriors recovered in Fig. 3.7. This offset reflects the change in the parameters recovered by the introduction of the additional parameters β and ϵ. Despite this offset, the injected value still lies within the 90% contour lines. In Fig. 3.10 we show the corresponding plot to Fig. 3.8, which demonstrates how the posteriors for the chirp mass change after the introduction of β and ϵ to the approximant. The injected value is still contained within each posterior

after its first reference in text

Table 3.4: The parameters used to generate the injections examined in this paper. Each of these entries corresponds to a set of 25 injections with β and ϵ in the range of $[-5, 5] \times [-5, 5]$.

param.	ra	dec	ι	ϕ_c	ψ	$d_L(\mathrm{Mpc})$	Mass 1	Mass 2
set 1	2.2	-1.25	2.5	1.5	1.75	100	30	30
set 2	2.2	-1.25	2.5	1.5	1.75	100	35	35
set 3	2.2	-1.25	2.5	1.5	1.75	100	40	40
set 4	2.2	-1.25	2.5	1.5	1.75	100	45	45
set 5	2.2	-1.25	2.5	1.5	1.75	100	50	50

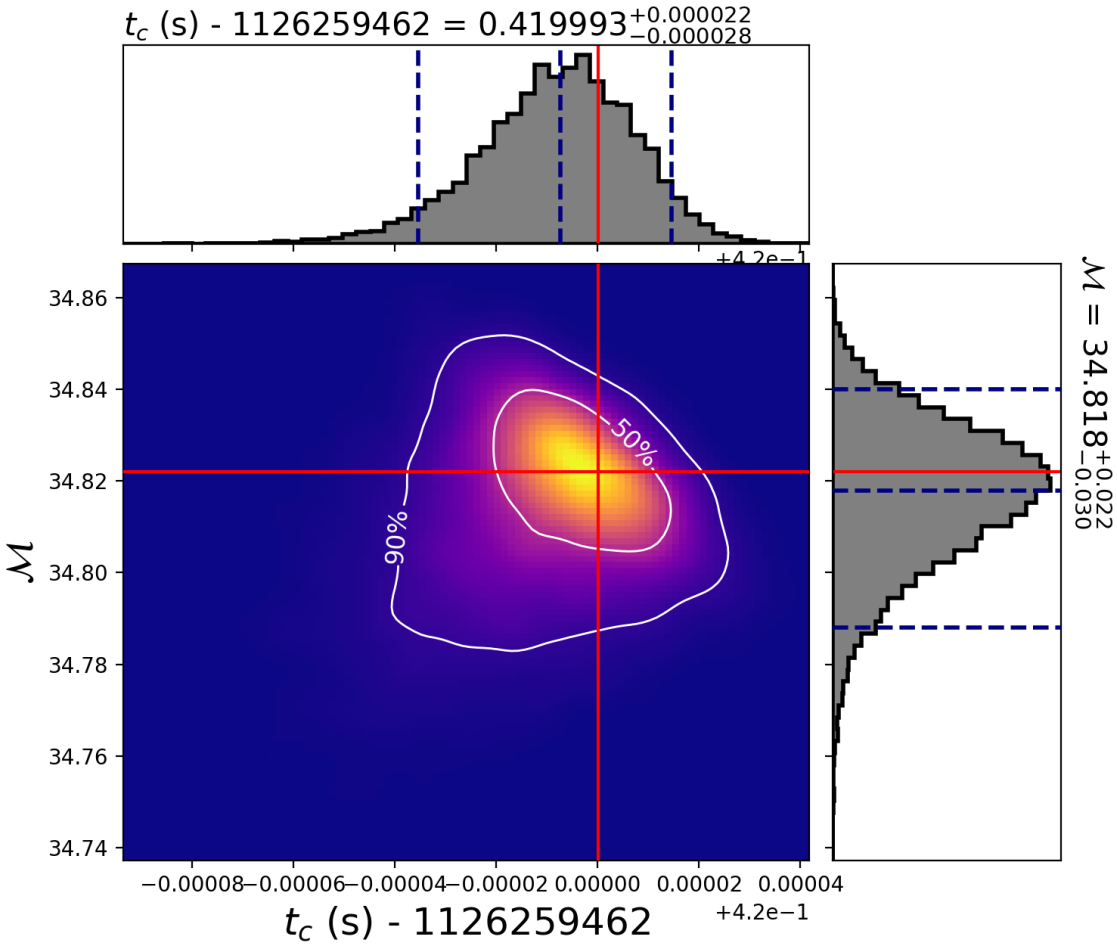

Figure 3.7: A corner plot showing the result of using a GR approximant as the underlying template when the underlying signal is GR in nature. The red lines mark the values of the parameters of the injection that are to be recovered. In this case the the injection is an equal-mass binary with a total mass of 80 solar masses.

across the masses probed, but the posteriors have also widened by a factor of roughly four compared to the GR approximant case.

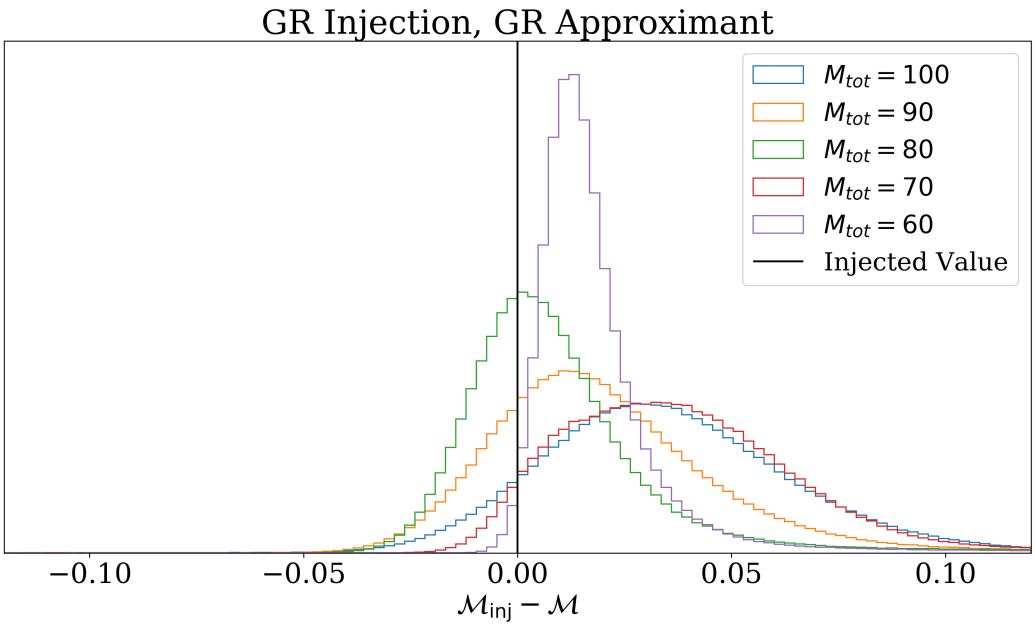

Figure 3.8: Posterior distribution results of the chirp mass $\mathcal{M}$ from five separate parameter estimation runs, each of a system with a different total mass, plotted on top of one another. Each run uses an unmodified IMRPhenomD approximant waveform. The black vertical line indicates the point around which the posterior should ideally be centered, in the case where the chirp mass is recovered perfectly.

ppE Injection, GR Approximant

In this section, we examine the results of parameter estimation where the injection is a ppE waveform, while the template is of a GR nature. In this case, there are no β or ϵ parameters in the template, and therefore there are no β nor ϵ posteriors recovered. However, because the injections are of a ppE nature, they are created with varying β and ϵ values. In this way, we can simulate how the presence of beyond-GR effects might instead be determined to be a GR signal, albeit one with slightly different parameters. In Fig. 3.11 we can see an example of this; the posteriors recovered correspond to that of a more massive system.

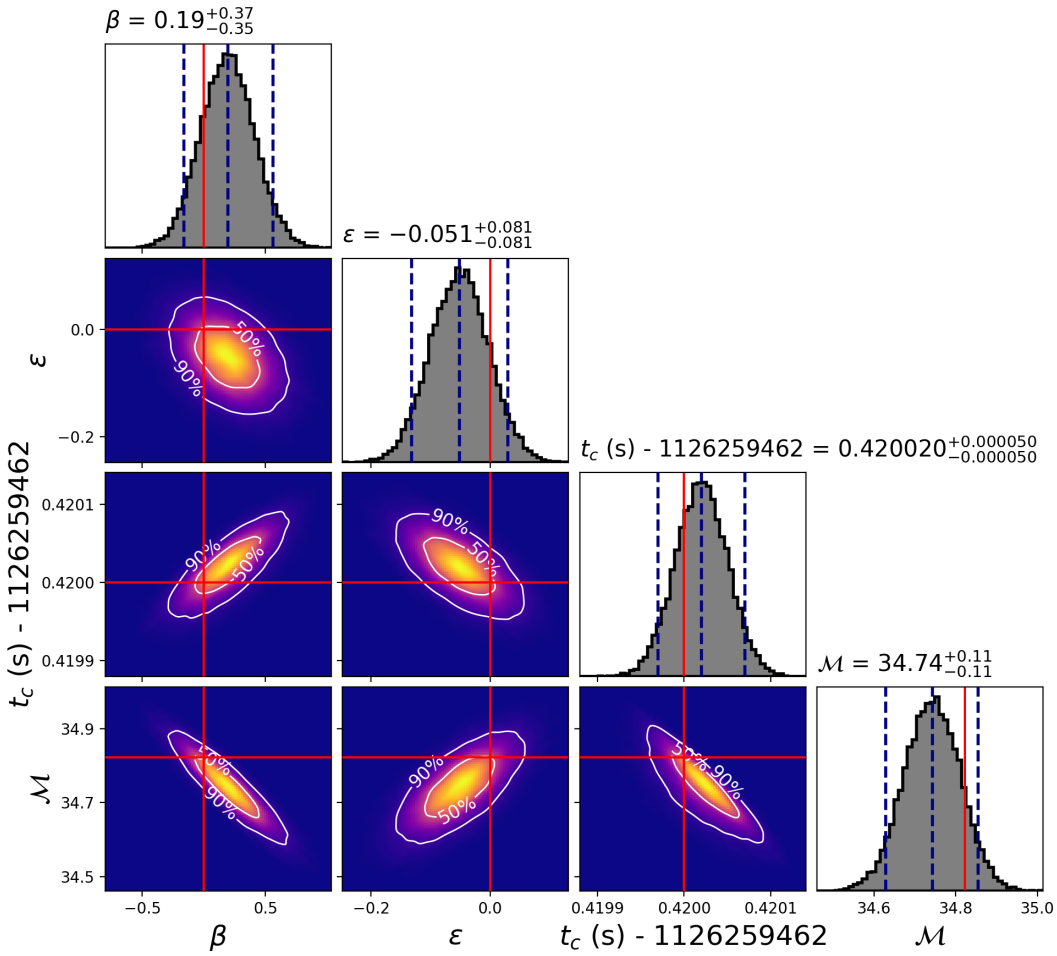

Figure 3.9: A corner plot showing the result of using a ppE-$\beta\epsilon$ approximant as the underlying template when the underlying signal is GR in nature. The red lines mark the values of the parameters of the injection that are to be recovered. Note that even in the case of a GR signal, which has $\beta = 0$ and $\epsilon = 0$, non-zero values are recovered. The injection is an equal-mass binary with a total mass of 80 solar masses.

ppE Injection, ppE Approximant

Finally, we examine the results of parameter estimation where both the injections as well as the templates are of a ppE nature. In this case, each injection is created with differing values of β and ϵ, and the templates will attempt to recover the standard GR

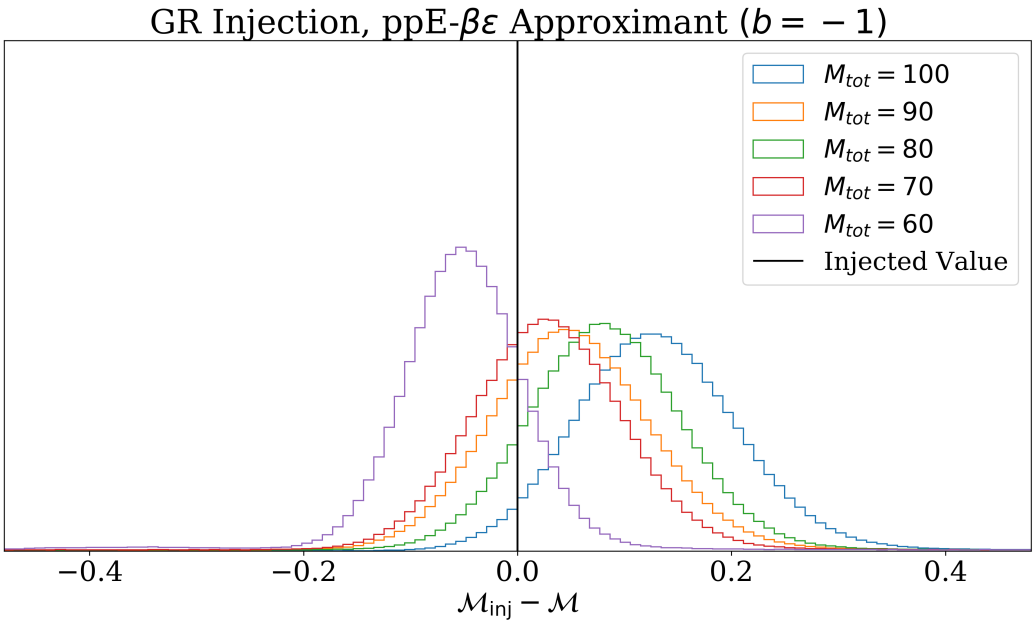

Figure 3.10: Posterior distribution results of the chirp mass $\mathcal{M}$ from five separate parameter estimation runs, each of a system with a different total mass, plotted on top of one another. Each run uses a ppE-$\beta\epsilon$ modified IMRPhenomD approximant waveform, where the ppE exponent b is set to -1. The black vertical line indicates the point around which the posterior should ideally be centered, in the case where the chirp mass is recovered perfectly.

parameters as well as β and ϵ for each of these cases. In Fig. 3.12 we see how both the β and ϵ posteriors contain the injected value, indicating that both are simultaneously recoverable. The joint posterior distribution indicates that the correlation between β and ϵ is less than or comparable to the correlation between either of these to the remaining parameters.

ppE-$\beta\epsilon$ correction

In the previous sections, we have examined whether the introduction of the β and ϵ parameters spoils the recovery of GR parameters. To do this, we compared the posteriors for coalescence time t_c and chirp mass $\mathcal{M}$ before and after this introduction, and

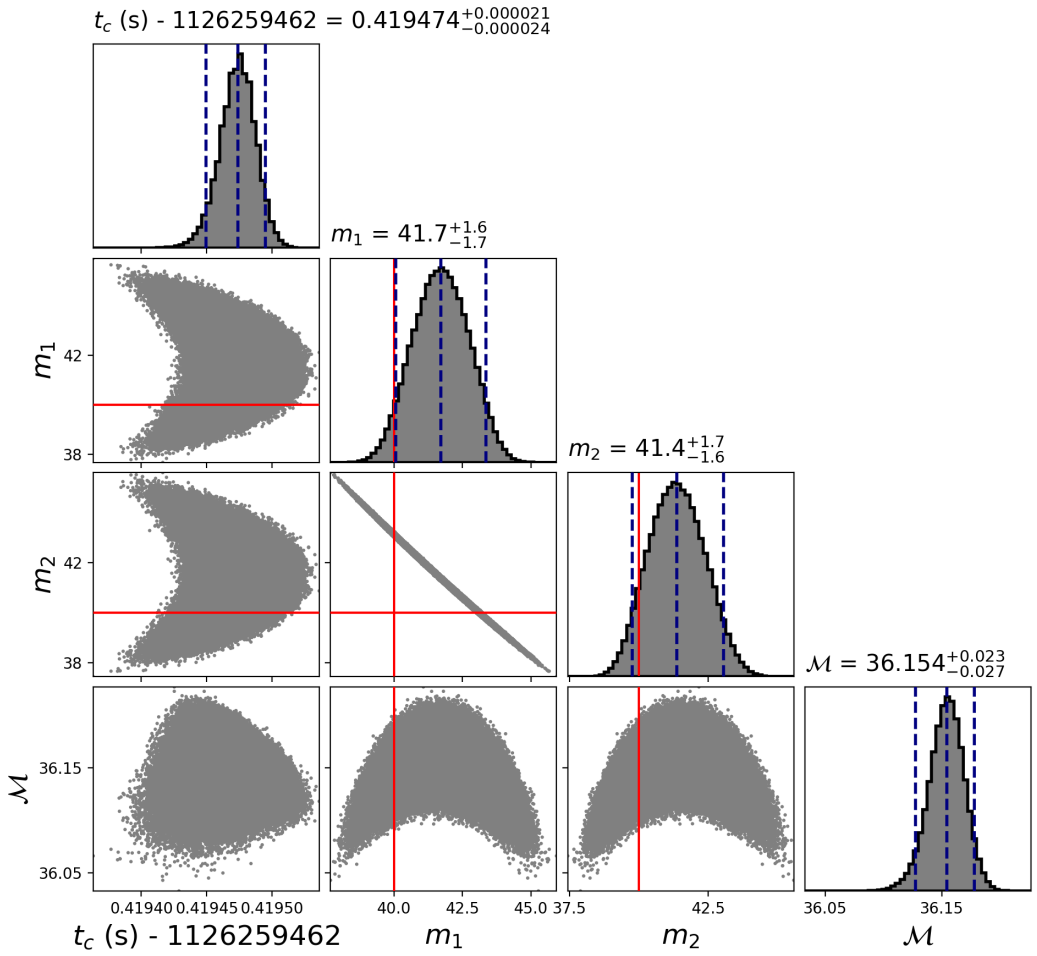

Figure 3.11: A corner plot showing the result of using a GR approximant to model parameter estimation templates when the underlying signal is ppE-$\beta\epsilon$ in nature. The red lines mark the values of the parameters of the injection that are to be recovered. In this case the the injection is an equal-mass binary with a total mass of 80 solar masses, with $\beta = -3$ and ϵ = -1. There are no density or contour lines in this plot because of the poor recovery of the parameters.

found that the recovery is not spoiled.

In Figs. 3.8 and 3.10 we show this result is robust for the mass range probed by LIGO. where the injection is generated using IMRPhenomD and the template is the $\beta\epsilon$-corrected IMRPhenomD, in the limit of zero noise.

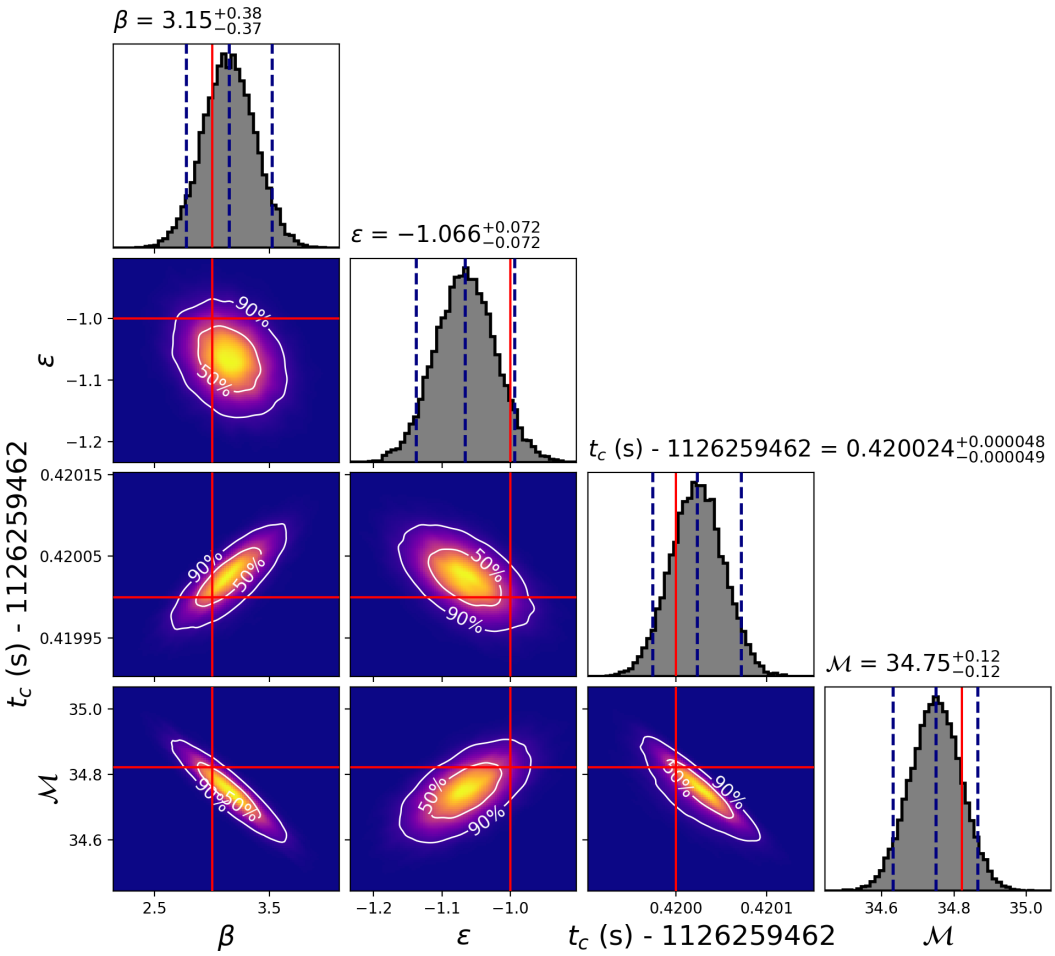

Figure 3.12: A corner plot showing the result of using a ppE-$\beta\epsilon$ approximant as the underlying template when the underlying signal is also of a ppE-$\beta\epsilon$ nature. The red lines mark the values of the parameters of the injection that are to be recovered. We note that the posteriors recovered are not significanly different from the posteriors recovered in the GR injection, GR approximant case, and in the GR injection, ppE approximant case. As in the previous cases, the injection is an equal mass binary with a total mass of 80 solar masses, with $\beta = -3$ and ϵ = -1.

Assuming the SNR is high enough to recover an accurate estimate of β, we can ask whether it is possible to recover the value of ϵ as well. One advantage of the ϵ extension to the ppE framework is that it is not necessary for β to be recoverable for ϵ to be recovered as well. Depending on the total mass of the binary, a different part

of the GW is in the LIGO band. Smaller mass binaries inspiral at higher frequencies, leaving more cycles in GW data. The longer inspirals aid in the recovery of β. On the other hand, if the GW is from a larger mass system, the power that is in the LIGO band is concentrated in the intermediate/merger-ringdown regime. As the ϵ parameter controls the deviation from GR in this region, it may still be recoverable in cases where β is not. With multiple runs one can quantify how the width of the posterior behaves in the $\beta\epsilon$ parameter space. When we plot the posterior distributions from different injections on top of one another, we see how sensitive the shape and location of the posteriors are on the beyond-GR parameters. To make clear how the parameters β and ϵ control the waveform in different frequency regimes, we repeat the parameter estimation runs on injections of different total masses. As expected, when the total mass is smaller, is it the higher-frequency inspiral portion that lies within the LIGO band, and so the distinguishability of different values of β is higher for lower system masses. Likewise, for higher mass systems, the lower-frequency merger falls within the LIGO band, and so the distinguishability of the different values of ϵ are higher here.

That β and ϵ are independently recoverable is demonstrated best by posterior distributions like those shown in Fig. 3.12. Even as the late-inspiral parameter ϵ is changed, the resulting posterior distribution for β still contains the injected value. While this relationship changes as the total mass of the system changes, depending on which parts of the inspiral fall into LIGO's sensitivity curve, it can be seen that both parameters are sufficiently distinguishable when both the inspiral and merger fall within LIGO's sensitivity curve.

3.5 Conclusion

We have presented a model suitable for exploring how the ppE model can be extended beyond the inspiral regime into the intermediate and merger-ringdown regimes. This extension is implemented as a generalization of the IMRPhenomD approximant in the form of an additional parameter that corresponds to the final merger time. We demonstrate that the recovery of this additional parameter does not significantly alter the precision with which we can recover the posteriors for the other parameters in the model. This allows us to perform parameter estimation using ppE-corrected waveforms where only the inspiral correction is known. The auxiliary parameter ϵ serves to signal the degree to which the inspiral correction can be extended into the intermediate and merger regimes. The analytic prior allows for the efficient sampling of the $\beta - \epsilon$ parameter space as the total mass varies, which approximates the current constraints on β. For high values of the signal-to-noise ratio, the value of β or ϵ needed for a particular match decreases. At a certain SNR, a value of zero for β or ϵ falls outside the 95% credible interval if GR is not valid. The value of b for which this occurs will determine the class of beyond-GR theories that are most supported by GW data. We defer a systematic study of this to future work. In the future we will show the bounds on β and ϵ using this extended model on the O3 LIGO data.

Acknowledgements

We thank Éamonn O'Shea and Masha Okounkova for useful discussions. This work was supported in part by the Sherman Fairchild Foundation and by NSF Grant PHY-1912081 at Cornell. P.K.'s research was also supported by the Department of Atomic Energy, Government of India, and by the Ashok and Gita Vaish Early Career Faculty

Fellowship at the International Centre for Theoretical Sciences.

BIBLIOGRAPHY

[1] Michael Boyle et al. The SXS Collaboration catalog of binary black hole simulations. *Class. Quant. Grav.*, 36(19):195006, 2019.

[2] Frans Pretorius. Evolution of binary black hole spacetimes. *Phys. Rev. Lett.*, 95:121101, 2005.

[3] Michael Pürrer and Carl-Johan Haster. Ready for what lies ahead? – Gravitational waveform accuracy requirements for future ground based detectors. *Phys. Rev. Res.*, 2(2):023151, 2020.

[4] Spectre. `https://github.com/sxs-collaboration/spectre`, 2017.

[5] B. P. Abbott, R. Abbott, T. D. Abbott, M. R. Abernathy, F. Acernese, K. Ackley, C. Adams, T. Adams, P. Addesso, R. X. Adhikari, V. B. Adya, C. Affeldt, M. Agathos, K. Agatsuma, N. Aggarwal, O. D. Aguiar, L. Aiello, A. Ain, P. Ajith, B. Allen, A. Allocca, P. A. Altin, S. B. Anderson, W. G. Anderson, K. Arai, M. C. Araya, C. C. Arceneaux, J. S. Areeda, N. Arnaud, K. G. Arun, S. Ascenzi, G. Ashton, M. Ast, S. M. Aston, P. Astone, P. Aufmuth, C. Aulbert, S. Babak, P. Bacon, M. K.M. Bader, P. T. Baker, F. Baldaccini, G. Ballardin, S. W. Ballmer, J. C. Barayoga, S. E. Barclay, B. C. Barish, D. Barker, F. Barone, B. Barr, L. Barsotti, M. Barsuglia, D. Barta, J. Bartlett, I. Bartos, R. Bassiri, A. Basti, J. C. Batch, C. Baune, V. Bavigadda, M. Bazzan, B. Behnke, M. Bejger, A. S. Bell, C. J. Bell, B. K. Berger, J. Bergman, G. Bergmann, C. P.L. Berry, D. Bersanetti, A. Bertolini, J. Betzwieser, S. Bhagwat, R. Bhandare, I. A. Bilenko, G. Billingsley, J. Birch, R. Birney, O. Birnholtz, S. Biscans, A. Bisht, M. Bitossi, C. Biwer, M. A. Bizouard, J. K. Blackburn, C. D. Blair, D. G. Blair, R. M. Blair, S. Bloemen, O. Bock, T. P. Bodiya, M. Boer, G. Bogaert, C. Bogan, A. Bohe, P. Bojtos, C. Bond, F. Bondu, R. Bonnand, B. A. Boom, R. Bork, V. Boschi, S. Bose, Y. Bouffanais, A. Bozzi, C. Bradaschia, P. R. Brady, V. B. Braginsky, M. Branchesi, J. E. Brau, T. Briant, A. Brillet, M. Brinkmann, V. Brisson, P. Brockill, A. F. Brooks, D. A. Brown, D. D. Brown, N. M. Brown, C. C. Buchanan, A. Buikema, T. Bulik, H. J. Bulten, A. Buonanno, D. Buskulic, C. Buy, R. L. Byer, L. Cadonati, G. Cagnoli, C. Cahillane, J. Calderón Bustillo, T. Callister, E. Calloni, J. B. Camp, K. C. Cannon, J. Cao, C. D. Capano, E. Capocasa, F. Carbognani, S. Caride, J. Casanueva Diaz, C. Casentini, S. Caudill, M. Cavaglià, F. Cavalier, R. Cavalieri, G. Cella, C. B. Cepeda, L. Cerboni Baiardi, G. Cerretani, E. Cesarini, R. Chakraborty, T. Chalermsongsak, S. J. Chamberlin, M. Chan, S. Chao, P. Charlton, E. Chassande-Mottin, H. Y. Chen, Y. Chen, C. Cheng, A. Chincarini, A. Chiummo, H. S. Cho, M. Cho, J. H. Chow, N. Christensen, Q. Chu, S. Chua, S. Chung, G. Ciani, F. Clara, J. A. Clark, F. Cleva, E. Coccia, P. F. Cohadon, A. Colla, C. G. Collette, L. Cominsky, M. Constancio, A. Conte, L. Conti, D. Cook, T. R. Corbitt, N. Cornish, A. Corsi, S. Cortese, C. A. Costa, M. W. Coughlin, S. B. Coughlin,

J. P. Coulon, S. T. Countryman, P. Couvares, E. E. Cowan, D. M. Coward, M. J. Cowart, D. C. Coyne, R. Coyne, K. Craig, J. D.E. Creighton, J. Cripe, S. G. Crowder, A. Cumming, L. Cunningham, E. Cuoco, T. Dal Canton, S. L. Danilishin, S. D'Antonio, K. Danzmann, N. S. Darman, V. Dattilo, I. Dave, H. P. Daveloza, M. Davier, G. S. Davies, E. J. Daw, R. Day, D. Debra, G. Debreczeni, J. Degallaix, M. De Laurentis, S. Deléglise, W. Del Pozzo, T. Denker, T. Dent, H. Dereli, V. Dergachev, R. De Rosa, R. T. Derosa, R. Desalvo, S. Dhurandhar, M. C. Díaz, L. Di Fiore, M. Di Giovanni, A. Di Lieto, S. Di Pace, I. Di Palma, A. Di Virgilio, G. Dojcinoski, V. Dolique, F. Donovan, K. L. Dooley, S. Doravari, R. Douglas, T. P. Downes, M. Drago, R. W.P. Drever, J. C. Driggers, Z. Du, M. Ducrot, S. E. Dwyer, T. B. Edo, M. C. Edwards, A. Effler, H. B. Eggenstein, P. Ehrens, J. Eichholz, S. S. Eikenberry, W. Engels, R. C. Essick, T. Etzel, M. Evans, T. M. Evans, R. Everett, M. Factourovich, V. Fafone, H. Fair, S. Fairhurst, X. Fan, Q. Fang, S. Farinon, B. Farr, W. M. Farr, M. Favata, M. Fays, H. Fehrmann, M. M. Fejer, I. Ferrante, E. C. Ferreira, F. Ferrini, F. Fidecaro, I. Fiori, D. Fiorucci, R. P. Fisher, R. Flaminio, M. Fletcher, J. D. Fournier, S. Franco, S. Frasca, F. Frasconi, Z. Frei, A. Freise, R. Frey, V. Frey, T. T. Fricke, P. Fritschel, V. V. Frolov, P. Fulda, M. Fyffe, H. A.G. Gabbard, J. R. Gair, L. Gammaitoni, S. G. Gaonkar, F. Garufi, A. Gatto, G. Gaur, N. Gehrels, G. Gemme, B. Gendre, E. Genin, A. Gennai, J. George, L. Gergely, V. Germain, Abhirup Ghosh, Archisman Ghosh, S. Ghosh, J. A. Giaime, K. D. Giardina, A. Giazotto, K. Gill, A. Glaefke, E. Goetz, R. Goetz, L. Gondan, G. González, J. M. Gonzalez Castro, A. Gopakumar, N. A. Gordon, M. L. Gorodetsky, S. E. Gossan, M. Gosselin, R. Gouaty, C. Graef, P. B. Graff, M. Granata, A. Grant, S. Gras, C. Gray, G. Greco, A. C. Green, P. Groot, H. Grote, S. Grunewald, G. M. Guidi, X. Guo, A. Gupta, M. K. Gupta, K. E. Gushwa, E. K. Gustafson, R. Gustafson, J. J. Hacker, B. R. Hall, E. D. Hall, G. Hammond, M. Haney, M. M. Hanke, J. Hanks, C. Hanna, M. D. Hannam, J. Hanson, T. Hardwick, J. Harms, G. M. Harry, I. W. Harry, M. J. Hart, M. T. Hartman, C. J. Haster, K. Haughian, J. Healy, A. Heidmann, M. C. Heintze, H. Heitmann, P. Hello, G. Hemming, M. Hendry, I. S. Heng, J. Hennig, A. W. Heptonstall, M. Heurs, S. Hild, D. Hoak, K. A. Hodge, D. Hofman, S. E. Hollitt, K. Holt, D. E. Holz, P. Hopkins, D. J. Hosken, J. Hough, E. A. Houston, E. J. Howell, Y. M. Hu, S. Huang, E. A. Huerta, D. Huet, B. Hughey, S. Husa, S. H. Huttner, T. Huynh-Dinh, A. Idrisy, N. Indik, D. R. Ingram, R. Inta, H. N. Isa, J. M. Isac, M. Isi, G. Islas, T. Isogai, B. R. Iyer, K. Izumi, T. Jacqmin, H. Jang, K. Jani, P. Jaranowski, S. Jawahar, F. Jiménez-Forteza, W. W. Johnson, N. K. Johnson-Mcdaniel, D. I. Jones, R. Jones, R. J.G. Jonker, L. Ju, M. K. Haris, C. V. Kalaghatgi, V. Kalogera, S. Kandhasamy, G. Kang, J. B. Kanner, S. Karki, M. Kasprzack, E. Katsavounidis, W. Katzman, S. Kaufer, T. Kaur, K. Kawabe, F. Kawazoe, F. Kéfélian, M. S. Kehl, D. Keitel, D. B. Kelley, W. Kells, R. Kennedy, J. S. Key, A. Khalaidovski, F. Y. Khalili, I. Khan, S. Khan, Z. Khan, E. A. Khazanov, N. Kijbunchoo, C. Kim, J. Kim, K. Kim, Nam Gyu Kim, Namjun Kim, Y. M. Kim, E. J. King, P. J. King, D. L. Kinzel, J. S. Kissel, L. Kleybolte, S. Klimenko, S. M. Koehlenbeck, K. Kokeyama, S. Koley, V. Kondrashov, A. Kontos, M. Korobko, W. Z. Korth, I. Kowalska, D. B. Kozak, V. Kringel, B. Krishnan,

A. Królak, C. Krueger, G. Kuehn, P. Kumar, L. Kuo, A. Kutynia, B. D. Lackey, M. Landry, J. Lange, B. Lantz, P. D. Lasky, A. Lazzarini, C. Lazzaro, P. Leaci, S. Leavey, E. O. Lebigot, C. H. Lee, H. K. Lee, H. M. Lee, K. Lee, A. Lenon, M. Leonardi, J. R. Leong, N. Leroy, N. Letendre, Y. Levin, B. M. Levine, T. G.F. Li, A. Libson, T. B. Littenberg, N. A. Lockerbie, J. Logue, A. L. Lombardi, L. T. London, J. E. Lord, M. Lorenzini, V. Loriette, M. Lormand, G. Losurdo, J. D. Lough, C. O. Lousto, G. Lovelace, H. Lück, A. P. Lundgren, J. Luo, R. Lynch, Y. Ma, T. Macdonald, B. Machenschalk, M. Macinnis, D. M. Macleod, F. Magaña-Sandoval, R. M. Magee, M. Mageswaran, E. Majorana, I. Maksimovic, V. Malvezzi, N. Man, I. Mandel, V. Mandic, V. Mangano, G. L. Mansell, M. Manske, M. Mantovani, F. Marchesoni, F. Marion, S. Márka, Z. Márka, A. S. Markosyan, E. Maros, F. Martelli, L. Martellini, I. W. Martin, R. M. Martin, D. V. Martynov, J. N. Marx, K. Mason, A. Masserot, T. J. Massinger, M. Masso-Reid, F. Matichard, L. Matone, N. Mavalvala, N. Mazumder, G. Mazzolo, R. McCarthy, D. E. McClelland, S. McCormick, S. C. McGuire, G. McIntyre, J. McIver, D. J. McManus, S. T. McWilliams, D. Meacher, G. D. Meadors, J. Meidam, A. Melatos, G. Mendell, D. Mendoza-Gandara, R. A. Mercer, E. Merilh, M. Merzougui, S. Meshkov, C. Messenger, C. Messick, P. M. Meyers, F. Mezzani, H. Miao, C. Michel, H. Middleton, E. E. Mikhailov, L. Milano, J. Miller, M. Millhouse, Y. Minenkov, J. Ming, S. Mirshekari, C. Mishra, S. Mitra, V. P. Mitrofanov, G. Mitselmakher, R. Mittleman, A. Moggi, M. Mohan, S. R.P. Mohapatra, M. Montani, B. C. Moore, C. J. Moore, D. Moraru, G. Moreno, S. R. Morriss, K. Mossavi, B. Mours, C. M. Mow-Lowry, C. L. Mueller, G. Mueller, A. W. Muir, Arunava Mukherjee, D. Mukherjee, S. Mukherjee, N. Mukund, A. Mullavey, J. Munch, D. J. Murphy, P. G. Murray, A. Mytidis, I. Nardecchia, L. Naticchioni, R. K. Nayak, V. Necula, K. Nedkova, G. Nelemans, M. Neri, A. Neunzert, G. Newton, T. T. Nguyen, A. B. Nielsen, S. Nissanke, A. Nitz, F. Nocera, D. Nolting, M. E. Normandin, L. K. Nuttall, J. Oberling, E. Ochsner, J. O'Dell, E. Oelker, G. H. Ogin, J. J. Oh, S. H. Oh, F. Ohme, M. Oliver, P. Oppermann, Richard J. Oram, B. O'Reilly, R. O'Shaughnessy, D. J. Ottaway, R. S. Ottens, H. Overmier, B. J. Owen, A. Pai, S. A. Pai, J. R. Palamos, O. Palashov, C. Palomba, A. Pal-Singh, H. Pan, Y. Pan, C. Pankow, F. Pannarale, B. C. Pant, F. Paoletti, A. Paoli, M. A. Papa, H. R. Paris, W. Parker, D. Pascucci, A. Pasqualetti, R. Passaquieti, D. Passuello, B. Patricelli, Z. Patrick, B. L. Pearlstone, M. Pedraza, R. Pedurand, L. Pekowsky, A. Pele, S. Penn, A. Perreca, H. P. Pfeiffer, M. Phelps, O. Piccinni, M. Pichot, F. Piergiovanni, V. Pierro, G. Pillant, L. Pinard, I. M. Pinto, M. Pitkin, R. Poggiani, P. Popolizio, A. Post, J. Powell, J. Prasad, V. Predoi, S. S. Premachandra, T. Prestegard, L. R. Price, M. Prijatelj, M. Principe, S. Privitera, R. Prix, G. A. Prodi, L. Prokhorov, O. Puncken, M. Punturo, P. Puppo, M. Pürrer, H. Qi, J. Qin, V. Quetschke, E. A. Quintero, R. Quitzow-James, F. J. Raab, D. S. Rabeling, H. Radkins, P. Raffai, S. Raja, M. Rakhmanov, P. Rapagnani, V. Raymond, M. Razzano, V. Re, J. Read, C. M. Reed, T. Regimbau, L. Rei, S. Reid, D. H. Reitze, H. Rew, S. D. Reyes, F. Ricci, K. Riles, N. A. Robertson, R. Robie, F. Robinet, A. Rocchi, L. Rolland, J. G. Rollins, V. J. Roma, R. Romano, G. Romanov, J. H. Romie, D. Rosińska, S. Rowan, A. Rüdiger, P. Ruggi, K. Ryan, S. Sachdev, T. Sadecki,

L. Sadeghian, L. Salconi, M. Saleem, F. Salemi, A. Samajdar, L. Sammut, E. J. Sanchez, V. Sandberg, B. Sandeen, J. R. Sanders, B. Sassolas, B. S. Sathyaprakash, P. R. Saulson, O. Sauter, R. L. Savage, A. Sawadsky, P. Schale, R. Schilling, J. Schmidt, P. Schmidt, R. Schnabel, R. M.S. Schofield, A. Schönbeck, E. Schreiber, D. Schuette, B. F. Schutz, J. Scott, S. M. Scott, D. Sellers, A. S. Sengupta, D. Sentenac, V. Sequino, A. Sergeev, G. Serna, Y. Setyawati, A. Sevigny, D. A. Shaddock, S. Shah, M. S. Shahriar, M. Shaltev, Z. Shao, B. Shapiro, P. Shawhan, A. Sheperd, D. H. Shoemaker, D. M. Shoemaker, K. Siellez, X. Siemens, D. Sigg, A. D. Silva, D. Simakov, A. Singer, L. P. Singer, A. Singh, R. Singh, A. Singhal, A. M. Sintes, B. J.J. Slagmolen, J. R. Smith, N. D. Smith, R. J.E. Smith, E. J. Son, B. Sorazu, F. Sorrentino, T. Souradeep, A. K. Srivastava, A. Staley, M. Steinke, J. Steinlechner, S. Steinlechner, D. Steinmeyer, B. C. Stephens, R. Stone, K. A. Strain, N. Straniero, G. Stratta, N. A. Strauss, S. Strigin, R. Sturani, A. L. Stuver, T. Z. Summerscales, L. Sun, P. J. Sutton, B. L. Swinkels, M. J. Szczepańczyk, M. Tacca, D. Talukder, D. B. Tanner, M. Tápai, S. P. Tarabrin, A. Taracchini, R. Taylor, T. Theeg, M. P. Thirugnanasambandam, E. G. Thomas, M. Thomas, P. Thomas, K. A. Thorne, K. S. Thorne, E. Thrane, S. Tiwari, V. Tiwari, K. V. Tokmakov, C. Tomlinson, M. Tonelli, C. V. Torres, C. I. Torrie, D. Töyrä, F. Travasso, G. Traylor, D. Trifirò, M. C. Tringali, L. Trozzo, M. Tse, M. Turconi, D. Tuyenbayev, D. Ugolini, C. S. Unnikrishnan, A. L. Urban, S. A. Usman, H. Vahlbruch, G. Vajente, G. Valdes, M. Vallisneri, N. Van Bakel, M. Van Beuzekom, J. F.J. Van Den Brand, C. Van Den Broeck, D. C. Vander-Hyde, L. Van Der Schaaf, J. V. Van Heijningen, A. A. Van Veggel, M. Vardaro, S. Vass, M. Vasúth, R. Vaulin, A. Vecchio, G. Vedovato, J. Veitch, P. J. Veitch, K. Venkateswara, D. Verkindt, F. Vetrano, A. Viceré, S. Vinciguerra, D. J. Vine, J. Y. Vinet, S. Vitale, T. Vo, H. Vocca, C. Vorvick, D. Voss, W. D. Vousden, S. P. Vyatchanin, A. R. Wade, L. E. Wade, M. Wade, M. Walker, L. Wallace, S. Walsh, G. Wang, H. Wang, M. Wang, X. Wang, Y. Wang, R. L. Ward, J. Warner, M. Was, B. Weaver, L. W. Wei, M. Weinert, A. J. Weinstein, R. Weiss, T. Welborn, L. Wen, P. Weßels, T. Westphal, K. Wette, J. T. Whelan, D. J. White, B. F. Whiting, D. Williams, R. D. Williams, A. R. Williamson, J. L. Willis, B. Willke, M. H. Wimmer, W. Winkler, C. C. Wipf, H. Wittel, G. Woan, J. Worden, J. L. Wright, G. Wu, J. Yablon, W. Yam, H. Yamamoto, C. C. Yancey, M. J. Yap, H. Yu, M. Yvert, A. Zadrożny, L. Zangrando, M. Zanolin, J. P. Zendri, M. Zevin, F. Zhang, L. Zhang, M. Zhang, Y. Zhang, C. Zhao, M. Zhou, Z. Zhou, X. J. Zhu, M. E. Zucker, S. E. Zuraw, J. Zweizig, M. Boyle, M. Campanelli, D. A. Hemberger, L. E. Kidder, S. Ossokine, M. A. Scheel, B. Szilagyi, S. Teukolsky, and Y. Zlochower. Tests of General Relativity with GW150914. *Physical Review Letters*, 116(22):1–17, 2016.

[6] C. M. Biwer, Collin D. Capano, Soumi De, Miriam Cabero, Duncan A. Brown, Alexander H. Nitz, and V. Raymond. PyCBC inference: a python-based parameter estimation toolkit for compact binary coalescence signals. *Publications of the Astronomical Society of the Pacific*, 131(996), 2019.

[7] B.P. Abbott et al. GW150914: First results from the search for binary black hole coalescence with Advanced LIGO. *Phys. Rev. D*, 93(12):122003, 2016.

[8] Noah Veltman. Warp-Off, 2016.

[9] Gabriel S. Bonilla. Redistributing Gridpoints, 2021.

[10] Gabriel S. Bonilla. domain::CoordinateMaps::Wedge $<$ Dim $>$ Class Reference, 2021.

[11] James Purser. U . S . Department of Commerce National Oceanic and Atmospheric Administration National Weather Service National Centers for Environmental Prediction College Park , MD 20740-3818 Office Note 496 MOBIUS NET CUBED-SPHERE GNOMONIC GRIDS IM Systems Group , Ro. (November), 2018.

[12] Gabriel S. Bonilla. domain::CoordinateMaps::BulgedCube Class Reference, 2021.

[13] J. S. Hesthaven. *A stable penalty method for the compressible navier-stokes equations: III. Multidimensional domain decomposition schemes*, volume 20. 1998.

[14] Gabriel S. Bonilla. domain::CoordinateMaps::SpecialMobius Class Reference, 2021.

[15] Gabriel S. Bonilla. domain::CoordinateMaps::Frustum Class Reference, 2021.

[16] Davide P. Cervone. Cubes and Hypercubes Rotating, 2002.

[17] Gabriel S. Bonilla. domain::CoordinateMaps::EquatorialCompression Class Reference, 2021.

[18] Gabriel S. Bonilla. OrientationMap, 2021.

[19] Lee Lindblom and Béla Szilágyi. Solving partial differential equations numerically on manifolds with arbitrary spatial topologies. *Journal of Computational Physics*, 243:151–175, 2013.

[20] Béla Szilágyi. Key elements of robustness in binary black hole evolutions using spectral methods. *International Journal of Modern Physics D*, 23(7), 2014.

[21] Gabriel S. Bonilla. domain::creators::BinaryCompactObject Class Reference, 2021.

[22] Béla Szilágyi, Lee Lindblom, and Mark A. Scheel. Simulations of binary black hole mergers using spectral methods. *Physical Review D - Particles, Fields, Gravitation and Cosmology*, 80(12):1–17, 2009.

[23] Emanuele Berti, Kent Yagi, and Nicolás Yunes. Extreme gravity tests with gravitational waves from compact binary coalescences: (I) inspiral–merger. *General Relativity and Gravitation*, 50(4), 2018.

[24] Katie Chamberlain and Nicolás Yunes. Theoretical physics implications of gravitational wave observation with future detectors. *Physical Review D*, 96(8), 2017.

[25] Lee Lindblom, Benjamin J. Owen, and Duncan A. Brown. Model waveform accuracy standards for gravitational wave data analysis. *Physical Review D - Particles, Fields, Gravitation and Cosmology*, 78(12):1–12, 2008.

[26] Maria Okounkova, Leo C. Stein, Jordan Moxon, Mark A. Scheel, and Saul A. Teukolsky. Numerical relativity simulation of GW150914 beyond general relativity. *Physical Review D*, 101(10):1–10, 2020.

[27] Nicolás Yunes and Frans Pretorius. Fundamental theoretical bias in gravitational wave astrophysics and the parametrized post-Einsteinian framework. *Physical Review D - Particles, Fields, Gravitation and Cosmology*, 80(12):1–25, 2009.

[28] Sharaban Tahura and Kent Yagi. Parametrized post-Einsteinian gravitational waveforms in various modified theories of gravity. *Physical Review D*, 98(8):1–21, 2018.

[29] Sebastian Khan, Sascha Husa, Mark Hannam, Frank Ohme, Michael Pürrer, Xisco Jiménez Forteza, and Alejandro Bohé. Frequency-domain gravitational waves from nonprecessing black-hole binaries. II. A phenomenological model for the advanced detector era. *Physical Review D*, 93(4):1–27, 2016.

[30] Lee S. Finn. Detection, measurement, and gravitational radiation. *Physical Review D*, 46(12):5236–5249, 1992.

[31] Sascha Husa, Sebastian Khan, Mark Hannam, Michael Pürrer, Frank Ohme, Xisco Jiménez Forteza, and Alejandro Bohé. Frequency-domain gravitational waves from nonprecessing black-hole binaries. I. New numerical waveforms and anatomy of the signal. *Physical Review D*, 93(4):1–17, 2016.

[32] Luc Blanchet. Gravitational radiation from post-newtonian sources and inspiralling compact binaries. *Living Reviews in Relativity*, 17:1–185, 2014.

[33] Carl L. Rodriguez, Benjamin Farr, Vivien Raymond, Will M. Farr, Tyson B. Littenberg, Diego Fazi, and Vicky Kalogera. Basic parameter estimation of binary neutron star systems by the advanced ligo/virgo network. *Astrophysical Journal*, 784(2), 2014.

[34] Kei Yamada and Takahiro Tanaka. Parametrized test of parity-violating gravity using GWTC-1 events. *Progress of Theoretical and Experimental Physics*, 2020(9):1–15, 2020.

[35] Nicolás Yunes, Kent Yagi, and Frans Pretorius. Theoretical physics implications of the binary black-hole mergers GW150914 and GW151226. *Physical Review D*, 94(8):1–42, 2016.

[36] R. Abbott, T. D. Abbott, S. Abraham, F. Acernese, K. Ackley, A. Adams, C. Adams, R. X. Adhikari, V. B. Adya, C. Affeldt, M. Agathos, K. Agatsuma, N. Aggarwal, O. D. Aguiar, L. Aiello, A. Ain, P. Ajith, S. Akcay, G. Allen, A. Allocca, P. A. Altin, A. Amato, S. Anand, A. Ananyeva, S. B. Anderson, W. G. Anderson, S. V. Angelova, S. Ansoldi, J. M. Antelis, S. Antier, S. Appert, K. Arai, M. C. Araya, J. S. Areeda, M. Arène, N. Arnaud, S. M. Aronson, K. G. Arun, Y. Asali, S. Ascenzi, G. Ashton, S. M. Aston, P. Astone, F. Aubin, P. Aufmuth, K. AultONeal, C. Austin, V. Avendano, S. Babak, F. Badaracco, M. K. M. Bader, S. Bae, A. M. Baer, S. Bagnasco, J. Baird, M. Ball, G. Ballardin, S. W. Ballmer, A. Bals, A. Balsamo, G. Baltus, S. Banagiri, D. Bankar, R. S. Bankar, J. C. Barayoga, C. Barbieri, B. C. Barish, D. Barker, P. Barneo, S. Barnum, F. Barone, B. Barr, L. Barsotti, M. Barsuglia, D. Barta, J. Bartlett, I. Bartos, R. Bassiri, A. Basti, M. Bawaj, J. C. Bayley, M. Bazzan, B. R. Becher, B. Bécsy, V. M. Bedakihale, M. Bejger, I. Belahcene, D. Beniwal, M. G. Benjamin, T. F. Bennett, J. D. Bentley, F. Bergamin, B. K. Berger, G. Bergmann, S. Bernuzzi, C. P. L. Berry, D. Bersanetti, A. Bertolini, J. Betzwieser, R. Bhandare, A. V. Bhandari, D. Bhattacharjee, J. Bidler, I. A. Bilenko, G. Billingsley, R. Birney, O. Birnholtz, S. Biscans, M. Bischi, S. Biscoveanu, A. Bisht, M. Bitossi, M. A. Bizouard, J. K. Blackburn, J. Blackman, C. D. Blair, D. G. Blair, R. M. Blair, O. Blanch, F. Bobba, N. Bode, M. Boer, Y. Boetzel, G. Bogaert, M. Boldrini, F. Bondu, R. Bonnand, E. Bonilla, P. Booker, B. A. Boom, R. Bork, V. Boschi, S. Bose, V. Bossilkov, V. Boudart, Y. Bouffanais, A. Bozzi, C. Bradaschia, P. R. Brady, A. Bramley, M. Branchesi, J. E. Brau, M. Breschi, T. Briant, J. H. Briggs, F. Brighenti, A. Brillet, M. Brinkmann, P. Brockill, A. F. Brooks, J. Brooks, D. D. Brown, S. Brunett, G. Bruno, R. Bruntz, A. Buikema, T. Bulik, H. J. Bulten, A. Buonanno, R. Buscicchio, D. Buskulic, R. L. Byer, M. Cabero, L. Cadonati, M. Caesar, G. Cagnoli, C. Cahillane, J. Calderón Bustillo, J. D. Callaghan, T. A. Callister, E. Calloni, J. B. Camp, M. Canepa, K. C. Cannon, H. Cao, J. Cao, G. Carapella, F. Carbognani, M. F. Carney, M. Carpinelli, G. Carullo, T. L. Carver, J. Casanueva Diaz, C. Casentini, S. Caudill, M. Cavaglià, F. Cavalier, R. Cavalieri, G. Cella, P. Cerdá-Durán, E. Cesarini, W. Chaibi, K. Chakravarti, C. L. Chan, C. Chan, K. Chandra, P. Chanial,

S. Chao, P. Charlton, E. A. Chase, E. Chassande-Mottin, D. Chatterjee, D. Chattopadhyay, M. Chaturvedi, K. Chatziioannou, A. Chen, H. Y. Chen, X. Chen, Y. Chen, H. P. Cheng, C. K. Cheong, H. Y. Chia, F. Chiadini, R. Chierici, A. Chincarini, A. Chiummo, G. Cho, H. S. Cho, M. Cho, S. Choate, N. Christensen, Q. Chu, S. Chua, K. W. Chung, S. Chung, G. Ciani, P. Ciecielag, M. Cieślar, M. Cifaldi, A. A. Ciobanu, R. Ciolfi, F. Cipriano, A. Cirone, F. Clara, E. N. Clark, J. A. Clark, L. Clarke, P. Clearwater, S. Clesse, F. Cleva, E. Coccia, P. F. Cohadon, D. E. Cohen, M. Colleoni, C. G. Collette, C. Collins, M. Colpi, M. Constancio, L. Conti, S. J. Cooper, P. Corban, T. R. Corbitt, I. Cordero-Carrión, S. Corezzi, K. R. Corley, N. Cornish, D. Corre, A. Corsi, S. Cortese, C. A. Costa, R. Cotesta, M. W. Coughlin, S. B. Coughlin, J. P. Coulon, S. T. Countryman, B. Cousins, P. Couvares, P. B. Covas, D. M. Coward, M. J. Cowart, D. C. Coyne, R. Coyne, J. D. E. Creighton, T. D. Creighton, M. Croquette, S. G. Crowder, J. R. Cudell, T. J. Cullen, A. Cumming, R. Cummings, L. Cunningham, E. Cuoco, M. Curylo, T. Dal Canton, G. Dálya, A. Dana, L. M. DaneshgaranBajastani, B. D'Angelo, B. Danila, S. L. Danilishin, S. D'Antonio, K. Danzmann, C. Darsow-Fromm, A. Dasgupta, L. E. H. Datrier, V. Dattilo, I. Dave, M. Davier, G. S. Davies, D. Davis, E. J. Daw, R. Dean, D. DeBra, M. Deenadayalan, J. Degallaix, M. De Laurentis, S. Deléglise, V. Del Favero, F. De Lillo, N. De Lillo, W. Del Pozzo, L. M. DeMarchi, F. De Matteis, V. D'Emilio, N. Demos, T. Denker, T. Dent, A. Depasse, R. De Pietri, R. De Rosa, C. De Rossi, R. DeSalvo, O. de Varona, S. Dhurandhar, M. C. Díaz, M. Diaz-Ortiz, N. A. Didio, T. Dietrich, L. Di Fiore, C. DiFronzo, C. Di Giorgio, F. Di Giovanni, M. Di Giovanni, T. Di Girolamo, A. Di Lieto, B. Ding, S. Di Pace, I. Di Palma, F. Di Renzo, A. K. Divakarla, A. Dmitriev, Z. Doctor, L. D'Onofrio, F. Donovan, K. L. Dooley, S. Doravari, I. Dorrington, T. P. Downes, M. Drago, J. C. Driggers, Z. Du, J. G. Ducoin, P. Dupej, O. Durante, D. D'Urso, P. A. Duverne, S. E. Dwyer, P. J. Easter, G. Eddolls, B. Edelman, T. B. Edo, O. Edy, A. Effler, J. Eichholz, S. S. Eikenberry, M. Eisenmann, R. A. Eisenstein, A. Ejlli, L. Errico, R. C. Essick, H. Estellés, D. Estevez, Z. B. Etienne, T. Etzel, M. Evans, T. M. Evans, B. E. Ewing, V. Fafone, H. Fair, S. Fairhurst, X. Fan, A. M. Farah, S. Farinon, B. Farr, W. M. Farr, E. J. Fauchon-Jones, M. Favata, M. Fays, M. Fazio, J. Feicht, M. M. Fejer, F. Feng, E. Fenyvesi, D. L. Ferguson, A. Fernandez-Galiana, I. Ferrante, T. A. Ferreira, F. Fidecaro, P. Figura, I. Fiori, D. Fiorucci, M. Fishbach, R. P. Fisher, J. M. Fishner, R. Fittipaldi, M. Fitz-Axen, V. Fiumara, R. Flaminio, E. Floden, E. Flynn, H. Fong, J. A. Font, P. W. F. Forsyth, J. D. Fournier, S. Frasca, F. Frasconi, Z. Frei, A. Freise, R. Frey, V. Frey, P. Fritschel, V. V. Frolov, G. G. Fronzé, P. Fulda, M. Fyffe, H. A. Gabbard, B. U. Gadre, S. M. Gaebel, J. R. Gair, J. Gais, S. Galaudage, R. Gamba, D. Ganapathy, A. Ganguly, S. G. Gaonkar, B. Garaventa, C. García-Quirós, F. Garufi, B. Gateley, S. Gaudio, V. Gayathri, G. Gemme, A. Gennai, D. George, J. George, R. N. George, L. Gergely, S. Ghonge, Abhirup Ghosh, Archisman Ghosh, S. Ghosh, B. Giacomazzo, L. Giacoppo, J. A. Giaime, K. D. Giardina, D. R. Gibson, C. Gier, K. Gill, P. Giri, J. Glanzer, A. E. Gleckl, P. Godwin, E. Goetz, R. Goetz, N. Gohlke, B. Goncharov, G. González, A. Gopakumar, S. E. Gossan, M. Gosselin, R. Gouaty, B. Grace, A. Grado, M. Granata, V. Granata, A. Grant, S. Gras, P. Grassia, C. Gray,

R. Gray, G. Greco, A. C. Green, R. Green, E. M. Gretarsson, H. L. Griggs, G. Grignani, A. Grimaldi, E. Grimes, S. J. Grimm, H. Grote, S. Grunewald, P. Gruning, J. G. Guerrero, G. M. Guidi, A. R. Guimaraes, G. Guixé, H. K. Gulati, Y. Guo, Anchal Gupta, Anuradha Gupta, P. Gupta, E. K. Gustafson, R. Gustafson, F. Guzman, L. Haegel, O. Halim, E. D. Hall, E. Z. Hamilton, G. Hammond, M. Haney, M. M. Hanke, J. Hanks, C. Hanna, M. D. Hannam, O. A. Hannuksela, O. Hannuksela, H. Hansen, T. J. Hansen, J. Hanson, T. Harder, T. Hardwick, K. Haris, J. Harms, G. M. Harry, I. W. Harry, D. Hartwig, R. K. Hasskew, C. J. Haster, K. Haughian, F. J. Hayes, J. Healy, A. Heidmann, M. C. Heintze, J. Heinze, J. Heinzel, H. Heitmann, F. Hellman, P. Hello, A. F. Helmling-Cornell, G. Hemming, M. Hendry, I. S. Heng, E. Hennes, J. Hennig, M. H. Hennig, F. Hernandez Vivanco, M. Heurs, S. Hild, P. Hill, A. S. Hines, S. Hochheim, E. Hofgard, D. Hofman, J. N. Hohmann, A. M. Holgado, N. A. Holland, I. J. Hollows, Z. J. Holmes, K. Holt, D. E. Holz, P. Hopkins, C. Horst, J. Hough, E. J. Howell, C. G. Hoy, D. Hoyland, Y. Huang, M. T. Hübner, A. D. Huddart, E. A. Huerta, B. Hughey, V. Hui, S. Husa, S. H. Huttner, B. M. Hutzler, R. Huxford, T. Huynh-Dinh, B. Idzkowski, A. Iess, S. Imperato, H. Inchauspe, C. Ingram, G. Intini, M. Isi, B. R. Iyer, V. JaberianHamedan, T. Jacqmin, S. J. Jadhav, S. P. Jadhav, A. L. James, K. Jani, K. Janssens, N. N. Janthalur, P. Jaranowski, D. Jariwala, R. Jaume, A. C. Jenkins, M. Jeunon, J. Jiang, G. R. Johns, N. K. Johnson-McDaniel, A. W. Jones, D. I. Jones, J. D. Jones, P. Jones, R. Jones, R. J. G. Jonker, L. Ju, J. Junker, C. V. Kalaghatgi, V. Kalogera, B. Kamai, S. Kandhasamy, G. Kang, J. B. Kanner, S. J. Kapadia, D. P. Kapasi, C. Karathanasis, S. Karki, R. Kashyap, M. Kasprzack, W. Kastaun, S. Katsanevas, E. Katsavounidis, W. Katzman, K. Kawabe, F. Kéfélian, D. Keitel, J. S. Key, S. Khadka, F. Y. Khalili, I. Khan, S. Khan, E. A. Khazanov, N. Khetan, M. Khursheed, N. Kijbunchoo, C. Kim, G. J. Kim, J. C. Kim, K. Kim, W. S. Kim, Y. M. Kim, C. Kimball, P. J. King, M. Kinley-Hanlon, R. Kirchhoff, J. S. Kissel, L. Kleybolte, S. Klimenko, T. D. Knowles, E. Knyazev, P. Koch, S. M. Koehlenbeck, G. Koekoek, S. Koley, M. Kolstein, K. Komori, V. Kondrashov, A. Kontos, N. Koper, M. Korobko, W. Z. Korth, M. Kovalam, D. B. Kozak, C. Krämer, V. Kringel, N. V. Krishnendu, A. Królak, G. Kuehn, A. Kumar, P. Kumar, Rahul Kumar, Rakesh Kumar, K. Kuns, S. Kwang, B. D. Lackey, D. Laghi, E. Lalande, T. L. Lam, A. Lamberts, M. Landry, B. B. Lane, R. N. Lang, J. Lange, B. Lantz, R. K. Lanza, I. La Rosa, A. Lartaux-Vollard, P. D. Lasky, M. Laxen, A. Lazzarini, C. Lazzaro, P. Leaci, S. Leavey, Y. K. Lecoeuche, H. M. Lee, H. W. Lee, J. Lee, K. Lee, J. Lehmann, E. Leon, N. Leroy, N. Letendre, Y. Levin, A. Li, J. Li, K. J. L. Li, T. G. F. Li, X. Li, F. Linde, S. D. Linker, J. N. Linley, T. B. Littenberg, J. Liu, X. Liu, M. Llorens-Monteagudo, R. K. L. Lo, A. Lockwood, L. T. London, A. Longo, M. Lorenzini, V. Loriette, M. Lormand, G. Losurdo, J. D. Lough, C. O. Lousto, G. Lovelace, H. Lück, D. Lumaca, A. P. Lundgren, Y. Ma, R. Macas, M. MacInnis, D. M. Macleod, I. A. O. MacMillan, A. Macquet, I. Magaña Hernandez, F. Magaña-Sandoval, C. Magazzù, R. M. Magee, E. Majorana, I. Maksimovic, S. Maliakal, A. Malik, N. Man, V. Mandic, V. Mangano, G. L. Mansell, M. Manske, M. Mantovani, M. Mapelli, F. Marchesoni, F. Marion, S. Márka, Z. Márka, C. Markakis, A. S. Markosyan, A. Markowitz, E. Maros,

A. Marquina, S. Marsat, F. Martelli, I. W. Martin, R. M. Martin, M. Martinez, V. Martinez, D. V. Martynov, H. Masalehdan, K. Mason, E. Massera, A. Masserot, T. J. Massinger, M. Masso-Reid, S. Mastrogiovanni, A. Matas, M. Mateu-Lucena, F. Matichard, M. Matiushechkina, N. Mavalvala, E. Maynard, J. J. McCann, R. McCarthy, D. E. McClelland, S. McCormick, L. McCuller, S. C. McGuire, C. McIsaac, J. McIver, D. J. McManus, T. McRae, S. T. McWilliams, D. Meacher, G. D. Meadors, M. Mehmet, A. K. Mehta, A. Melatos, D. A. Melchor, G. Mendell, A. Menendez-Vazquez, R. A. Mercer, L. Mereni, K. Merfeld, E. L. Merilh, J. D. Merritt, M. Merzougui, S. Meshkov, C. Messenger, C. Messick, R. Metzdorff, P. M. Meyers, F. Meylahn, A. Mhaske, A. Miani, H. Miao, I. Michaloliakos, C. Michel, H. Middleton, L. Milano, A. L. Miller, M. Millhouse, J. C. Mills, E. Milotti, M. C. Milovich-Goff, O. Minazzoli, Y. Minenkov, Ll. M. Mir, A. Mishkin, C. Mishra, T. Mistry, S. Mitra, V. P. Mitrofanov, G. Mitselmakher, R. Mittleman, G. Mo, K. Mogushi, S. R. P. Mohapatra, S. R. Mohite, I. Molina, M. Molina-Ruiz, M. Mondin, M. Montani, C. J. Moore, D. Moraru, F. Morawski, G. Moreno, S. Morisaki, B. Mours, C. M. Mow-Lowry, S. Mozzon, F. Muciaccia, Arunava Mukherjee, D. Mukherjee, Soma Mukherjee, Subroto Mukherjee, N. Mukund, A. Mullavey, J. Munch, E. A. Muñiz, P. G. Murray, S. L. Nadji, A. Nagar, I. Nardecchia, L. Naticchioni, R. K. Nayak, B. F. Neil, J. Neilson, G. Nelemans, T. J. N. Nelson, M. Nery, A. Neunzert, A. H. Nitz, K. Y. Ng, S. Ng, C. Nguyen, P. Nguyen, T. Nguyen, S. A. Nichols, S. Nissanke, F. Nocera, M. Noh, C. North, D. Nothard, L. K. Nuttall, J. Oberling, B. D. O'Brien, J. O'Dell, G. Oganesyan, G. H. Ogin, J. J. Oh, S. H. Oh, F. Ohme, H. Ohta, M. A. Okada, C. Olivetto, P. Oppermann, R. J. Oram, B. O'Reilly, R. G. Ormiston, L. F. Ortega, R. O'Shaughnessy, S. Ossokine, C. Osthelder, D. J. Ottaway, H. Overmier, B. J. Owen, A. E. Pace, G. Pagano, M. A. Page, G. Pagliaroli, A. Pai, S. A. Pai, J. R. Palamos, O. Palashov, C. Palomba, H. Pan, P. K. Panda, T. H. Pang, C. Pankow, F. Pannarale, B. C. Pant, F. Paoletti, A. Paoli, A. Paolone, W. Parker, D. Pascucci, A. Pasqualetti, R. Passaquieti, D. Passuello, M. Patel, B. Patricelli, E. Payne, T. C. Pechsiri, M. Pedraza, M. Pegoraro, A. Pele, S. Penn, A. Perego, C. J. Perez, C. Périgois, A. Perreca, S. Perriès, J. Petermann, D. Petterson, H. P. Pfeiffer, K. A. Pham, K. S. Phukon, O. J. Piccinni, M. Pichot, M. Piendibene, F. Piergiovanni, L. Pierini, V. Pierro, G. Pillant, F. Pilo, L. Pinard, I. M. Pinto, K. Piotrzkowski, M. Pirello, M. Pitkin, E. Placidi, W. Plastino, C. Pluchar, R. Poggiani, E. Polini, D. Y. T. Pong, S. Ponrathnam, P. Popolizio, E. K. Porter, A. Poverman, J. Powell, M. Pracchia, A. K. Prajapati, K. Prasai, R. Prasanna, G. Pratten, T. Prestegard, M. Principe, G. A. Prodi, L. Prokhorov, P. Prosposito, L. Prudenzi, A. Puecher, M. Punturo, F. Puosi, P. Puppo, M. Pürrer, H. Qi, V. Quetschke, P. J. Quinonez, R. Quitzow-James, F. J. Raab, G. Raaijmakers, H. Radkins, N. Radulesco, P. Raffai, H. Rafferty, S. X. Rail, S. Raja, C. Rajan, B. Rajbhandari, M. Rakhmanov, K. E. Ramirez, T. D. Ramirez, A. Ramos-Buades, J. Rana, K. Rao, P. Rapagnani, U. D. Rapol, B. Ratto, V. Raymond, M. Razzano, J. Read, T. Regimbau, L. Rei, S. Reid, D. H. Reitze, P. Rettegno, F. Ricci, C. J. Richardson, J. W. Richardson, L. Richardson, P. M. Ricker, G. Riemenschneider, K. Riles, M. Rizzo, N. A. Robertson, F. Robinet, A. Rocchi, J. A. Rocha, S. Rodriguez, R. D. Rodriguez-Soto, L. Rolland, J. G.

Rollins, V. J. Roma, M. Romanelli, R. Romano, C. L. Romel, A. Romero, I. M. Romero-Shaw, J. H. Romie, S. Ronchini, C. A. Rose, D. Rose, K. Rose, M. J. B. Rosell, D. Rosińska, S. G. Rosofsky, M. P. Ross, S. Rowan, S. J. Rowlinson, Santosh Roy, Soumen Roy, P. Ruggi, K. Ryan, S. Sachdev, T. Sadecki, J. Sadiq, M. Sakellariadou, O. S. Salafia, L. Salconi, M. Saleem, A. Samajdar, E. J. Sanchez, J. H. Sanchez, L. E. Sanchez, N. Sanchis-Gual, J. R. Sanders, L. Sandles, K. A. Santiago, E. Santos, T. R. Saravanan, N. Sarin, B. Sassolas, B. S. Sathyaprakash, O. Sauter, R. L. Savage, V. Savant, D. Sawant, S. Sayah, D. Schaetzl, P. Schale, M. Scheel, J. Scheuer, A. Schindler-Tyka, P. Schmidt, R. Schnabel, R. M. S. Schofield, A. Schönbeck, E. Schreiber, B. W. Schulte, B. F. Schutz, O. Schwarm, E. Schwartz, J. Scott, S. M. Scott, M. Seglar-Arroyo, E. Seidel, D. Sellers, A. S. Sengupta, N. Sennett, D. Sentenac, V. Sequino, A. Sergeev, Y. Setyawati, T. Shaffer, M. S. Shahriar, S. Sharifi, A. Sharma, P. Sharma, P. Shawhan, H. Shen, M. Shikauchi, R. Shink, D. H. Shoemaker, D. M. Shoemaker, K. Shukla, S. ShyamSundar, M. Sieniawska, D. Sigg, L. P. Singer, D. Singh, N. Singh, A. Singha, A. Singhal, A. M. Sintes, V. Sipala, V. Skliris, B. J. J. Slagmolen, T. J. Slaven-Blair, J. Smetana, J. R. Smith, R. J. E. Smith, S. N. Somala, E. J. Son, K. Soni, S. Soni, B. Sorazu, V. Sordini, F. Sorrentino, N. Sorrentino, R. Soulard, T. Souradeep, E. Sowell, A. P. Spencer, M. Spera, A. K. Srivastava, V. Srivastava, K. Staats, C. Stachie, D. A. Steer, J. Steinhoff, M. Steinke, J. Steinlechner, S. Steinlechner, D. Steinmeyer, S. P. Stevenson, G. Stolle-McAllister, D. J. Stops, M. Stover, K. A. Strain, G. Stratta, A. Strunk, R. Sturani, A. L. Stuver, J. Südbeck, S. Sudhagar, V. Sudhir, H. G. Suh, T. Z. Summerscales, H. Sun, L. Sun, S. Sunil, A. Sur, J. Suresh, P. J. Sutton, B. L. Swinkels, M. J. Szczepańczyk, M. Tacca, S. C. Tait, C. Talbot, A. J. Tanasijczuk, D. B. Tanner, D. Tao, A. Tapia, E. N. Tapia San Martin, J. D. Tasson, R. Taylor, R. Tenorio, L. Terkowski, M. P. Thirugnanasambandam, L. M. Thomas, M. Thomas, P. Thomas, J. E. Thompson, S. R. Thondapu, K. A. Thorne, E. Thrane, Shubhanshu Tiwari, Srishti Tiwari, V. Tiwari, K. Toland, A. E. Tolley, M. Tonelli, Z. Tornasi, A. Torres-Forné, C. I. Torrie, I. Tosta e Melo, D. Töyrä, A. T. Tran, A. Trapananti, F. Travasso, G. Traylor, M. C. Tringali, A. Tripathee, A. Trovato, R. J. Trudeau, D. S. Tsai, K. W. Tsang, M. Tse, R. Tso, L. Tsukada, D. Tsuna, T. Tsutsui, M. Turconi, A. S. Ubhi, R. P. Udall, K. Ueno, D. Ugolini, C. S. Unnikrishnan, A. L. Urban, S. A. Usman, A. C. Utina, H. Vahlbruch, G. Vajente, A. Vajpeyi, G. Valdes, M. Valentini, V. Valsan, N. van Bakel, M. van Beuzekom, J. F. J. van den Brand, C. Van Den Broeck, D. C. Vander-Hyde, L. van der Schaaf, J. V. van Heijningen, M. Vardaro, A. F. Vargas, V. Varma, S. Vass, M. Vasúth, A. Vecchio, G. Vedovato, J. Veitch, P. J. Veitch, K. Venkateswara, J. Venneberg, G. Venugopalan, D. Verkindt, Y. Verma, D. Veske, F. Vetrano, A. Viceré, A. D. Viets, A. Vijaykumar, V. Villa-Ortega, J. Y. Vinet, S. Vitale, T. Vo, H. Vocca, C. Vorvick, S. P. Vyatchanin, A. R. Wade, L. E. Wade, M. Wade, R. C. Walet, M. Walker, G. S. Wallace, L. Wallace, S. Walsh, J. Z. Wang, S. Wang, W. H. Wang, Y. F. Wang, R. L. Ward, J. Warner, M. Was, N. Y. Washington, J. Watchi, B. Weaver, L. Wei, M. Weinert, A. J. Weinstein, R. Weiss, F. Wellmann, L. Wen, P. Weßels, J. W. Westhouse, K. Wette, J. T. Whelan, D. D. White, L. V. White, B. F. Whiting, C. Whittle, D. M. Wilken, D. Williams, M. J. Williams, A. R. Williamson, J. L. Willis, B. Willke, D. J. Wilson,

M. H. Wimmer, W. Winkler, C. C. Wipf, G. Woan, J. Woehler, J. K. Wofford, I. C. F. Wong, J. Wrangel, J. L. Wright, D. S. Wu, D. M. Wysocki, L. Xiao, H. Yamamoto, L. Yang, Y. Yang, Z. Yang, M. J. Yap, D. W. Yeeles, A. Yoon, Hang Yu, Haocun Yu, S. H. R. Yuen, A. Zadrożny, M. Zanolin, T. Zelenova, J. P. Zendri, M. Zevin, J. Zhang, L. Zhang, R. Zhang, T. Zhang, C. Zhao, G. Zhao, Y. Zheng, M. Zhou, Z. Zhou, X. J. Zhu, A. B. Zimmerman, Y. Zlochower, M. E. Zucker, and J. Zweizig. GWTC-2: Compact Binary Coalescences Observed by LIGO and Virgo During the First Half of the Third Observing Run. pages 1–54, 2020.